

**DEVELOPMENT OF A PULSED PLASMA THRUSTER
FOR NANOSATELLITE APPLICATIONS**

by

Gert Jacobus Kotze

**This thesis is submitted at the Cape Peninsula University of Technology in fulfilment of
the requirements for this degree of**



**Master of Engineering in Mechanical Engineering
Department of Mechanical and Mechatronics Engineering**

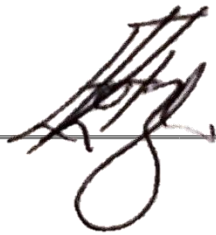
**Supervisor: Prof. Graeme Oliver
Co-supervisor: Dr. Kessie Govender**

**Bellville Campus
September 2022**

Declaration

I, Gert Jacobus Kotze, declare that the contents of this thesis represent my own unaided work and that the dissertation/thesis has not previously been submitted for academic examination towards any qualification. Furthermore, it represents my own opinions and not necessarily those of the Cape Peninsula University of Technology. All consulted literature is listed in the bibliography section.

Signed



Date

13/09/2022

Copyright © 2020 Cape Peninsula University of Technology

All rights reserved

Acknowledgements

Thanks goes to the following people who supported me throughout this project, without you, this was not possible:

- My main supervisor, Prof Graeme Oliver. Thank you for allowing me to pursue this research topic. By allowing me to do this, I grew not only as an engineer but as a researcher.
- My co-supervisor, Dr. Kessie Govender. Your wisdom is not unnoticed. Thank you for all of the advice, talks and effort that you were willing to put in to help me understand the field of physics better and improve my way of working in general. Your generosity will be remembered.
- To CPUT, for the opportunity to use their equipment and to pursue this topic.
- To Heinrich Jordaan, for his immense help during the Covid-19 period to allow me to use his garage and equipment to construct the pulsed plasma thruster and test theoretical concepts. Without you, this project was not possible, and I will forever be grateful for that.
- To my family, for always standing by my side no matter how hard things get. For always believing in me even when I'm sceptical. Thank you for your support during this time! It means the world.
- To my girlfriend, who has truly been one of the biggest blessings I could have asked for, especially during this time. Thank you for all of the 4 am study break talks and keeping my spirits high.
- To my friends, thank you for all of the love and support, even when I always said no to all of the invitations.

Abstract

For space missions to become more advanced and cost-effective, the manoeuvrability of spacecraft over the long term is required. Hence, both quantitative and qualitative work should be directed towards the development and optimization of electric propulsion (EP) systems that can support the mission requirements of the new space age. After comparing various propulsion systems within a survey, it was found that the electromagnetic ablative pulsed plasma thruster was best suited for this project. This is due to the simplicity, cost-effectiveness and reliability of this type of thruster. The primary objective of this work was to design, build and test a micro pulsed plasma thruster (μ PPT) for utilisation in future F'SATI nanosatellite missions. Hence, a numerical model was introduced to estimate thruster performance and system parameters. The numerical model was solved using a MATLAB® application with a dedicated guided user interface (GUI). Results from the numerical simulation led to a $4.44 \mu\text{F}$ capacitor, discharging at 1500 V, while practical designs only allowed for a $6 \mu\text{F}$ capacitor, discharging at 1200V. The experimental μ PPT consists of two copper electrodes separated by a solid polytetrafluoroethylene (Teflon) propellant bar of 2.5 cm^2 surface area, with a discharge energy of 4.32 J. To charge the main capacitors to 1200V, an applied voltage of 9.5 V was connected to an XP power DC-to-DC converter, where manual switches were used to control the charge and discharge cycles. Due to the impracticality of manual switching on nanosatellites, a circuit proposal is presented in appendix E for future development. The experimental tests consisted of two experiments (a 40 mm electrode and a 25 mm electrode) where the voltage discharge, current discharge and thrust were measured. Testing of the thruster involved the utilisation of a vacuum chamber, a power supply, high voltage probes and an oscilloscope. To determine the thrust of the μ PPT, a torsion balance is presented from the derived Cavendish experiment. From the voltage discharge measurements, it was found that for both experiments, the thruster consists of a high system resistance of approximately $126 \text{ m}\Omega$. From the current discharge, it is shown that the plasma resistance is $53.159 \text{ m}\Omega$ and $37.04 \text{ m}\Omega$ for experiment 1 and experiment 2 respectively. Furthermore, using a self-made thrust balance, it was calculated that a maximum thrust of $3.374 \text{ mN} \pm 20\%$ was achieved for a thruster discharging at 1200 V under 0.75 Torr. Tests showed that a pressure variance leads to a variance in thrust. Therefore, extrapolating between various pressure tests, while keeping the thruster parameters constant, an estimated

thrust of $270 \mu\text{N}$ was theoretically achieved. Furthermore, comparing the thrust generated in experiment 1 and experiment 2 leads to the conclusion that the physical length of the thruster has minimal effect on the performance of the μPPT . Hence, a more compact design can be achieved. This thesis presents the design of a compact μPPT system for improved spacecraft manoeuvrability that is suitable for use on future F'SATI nano-satellites. It includes improved circuitry, suggested testing equipment, additional tests to fully characterise the PPT system, and recommended future work in this regard.

Contents

Declaration.....	i
Acknowledgements	ii
Abstract.....	iii
Contents	v
List of Tables	x
List of Figures.....	xi
Nomenclature.....	xvii
1. Introduction	1
1.1 Background and Motivation	2
1.1.1 The Demand for Propulsion Systems for the New Space Age.....	2
1.1.2 Growth of Nanosatellites and F'SATI MDA Project	2
1.1.3 Industry Concerns on Nanosatellite Space Debris	3
1.1.4 CubeSat Design and Specifications.....	4
1.2 Aims and Objectives	5
1.2.1 Numerical Model.....	5
1.2.2 μ PPT Design Stages and Experimental Work.....	6
1.3 Delineation of Research Outcomes.....	7
1.4 Research Methodology	8
1.5 General Overview of Propulsion	9
1.5.1 Fundamental Propulsion Concepts	9
1.5.2 Electric Propulsion Systems	11

1.5.3	Pulsed Plasma Thrusters Overview	12
1.6	Summary	14
2.	Literature Survey and Introduction to Pulsed Plasma Thrusters	15
2.1	Basic PPT Theory and Performance	15
2.2	Mechanical Geometry	20
2.3	Electrode and Insulator Materials	23
2.4	Feed Mechanism	25
2.5	Arc Power Circuit	26
2.6	Arc Triggering	26
2.7	Summary and Conclusion	28
3.	An Introduction to Parallel Plate Pulsed Plasma Theory	29
3.1	A General Survey of Pulsed Plasma Models	29
3.2	General Electromechanical Model for a Parallel-Plate PPT.....	30
3.2.1	Self-Induced Magnetic Field	33
3.2.2	Parallel Plate Inductance Model	37
3.2.3	Dynamical model.....	37
3.2.4	Plasma Resistance model	38
3.2.5	Mass Distribution Model	40
3.2.6	Summary of the General Electromechanical model	41
3.3	Improved Electromechanical Models for a Parallel-Plate PPT	42
3.4	General Slug and Snowplow Models.....	46
3.4.1	Slug Model	47
3.4.2	Snowplow Model.....	47
3.5	Summary and Conclusion	49
4.	Numerical Model Simulation for a Parallel Plate PPT.....	50
4.1	Introduction.....	50

4.2	Model Simplification and Assumptions	51
4.3	Revision of the General Electromechanical Model	51
4.4	Numerical Implementation of the General Electromechanical Model	52
4.5	Software to Implement the Numerical Model	55
4.6	Model Validation	60
4.6.1	LES-6 model comparison	61
4.6.2	LES-8/9 model comparison	63
4.7	μ PPT Parameters Comparison for Preliminary Design	64
4.7.1	Evaluation of the Initial Voltage to Capacitance Ratio	65
4.7.2	Evaluation of the Aspect Ratio	68
4.7.3	Suggested Preliminary Design Parameters	71
4.8	Summary and Conclusion	73
5.	Thruster and Power Circuit Design	75
5.1	Conceptual Designs	76
5.1.1	PPT geometry types	76
5.1.2	PPT Power Circuit Design	79
5.2	Preliminary Design	80
5.2.1	Geometry of PPT	81
5.2.2	Design of PPT Power Circuit	82
5.3	Final Experimental Prototype	85
5.4	Summary	91
6.	Experimental Setup and Test Procedures	93
6.1	Experimental Test Setup	94
6.2	Experimental Testing Approach	97
6.3	Direct Thrust Measuring System	100
6.3.1	DTMS Overview	100

6.3.2	Preliminary Design of DTMS	102
6.3.3	Final DTMS Artifact	108
6.3.4	Calibration of DTMS.....	111
6.3.5	Summary of DTMS	114
6.4	Summary and Conclusion	115
7.	Experimental Results and Discussion	116
7.1	Experimental Limitations	117
7.2	Experimental Results: Parameter Analysis.....	118
7.2.1	Voltage Discharge Measurements	119
7.2.2	Current Discharge Measurements	122
7.2.3	Estimated plasma temperature.....	125
7.2.4	Thrust Measurements and Thrust Extrapolation to LEO pressures.....	127
7.2.5	Electrode Length Evaluation	130
7.3	Summary.....	132
8.	Conclusions and Recommended Future work	134
8.1	Conclusion	134
8.1.1	Numerical Model.....	134
8.1.2	Design.....	135
8.1.3	Experimental work	136
8.2	Proposed Future Work	137
8.2.1	Future Work on Theoretical and Numerical Models.....	137
8.2.2	Experimental Future Work	138
	Appendices	142
A	Review on Available Propulsion Technology for Nanosatellites.....	142
A.1	Descriptive Characteristics of Variable Thrusters.....	142
A.2	Performance Evaluation of Variable Thrusters	144

B	Computer-Aided Design of Preliminary Design Components	148
C	STK Simulation for Preliminary Design	154
D	Measuring the Discharge Voltage using a Self-Made Voltage Divider	159
E	Proposed Circuitry for Future Research	161
	Electrical design.....	161
	Circuit Operation	162
	Bibliography	164

List of Tables

Table 2-1 Essential PPT performance design factors (Rezaeiha, 2014).....	18
Table 2-2. General μ PPT operating conditions and performance	19
Table 2-3 Alternative PPT Propellant types (Rezaeiha & Schonherr, 2013)	23
Table 2-4 Brass and molybdenum performance comparison when used as electrode material	24
Table 2-5 Solid Propellant Performance Comparison (Palumbo & Guman, 1976)	24
Table 2-6 Performance results of InBr ₃ /Teflon (Palumbo & Guman, 1976).....	25
Table 2-7 Vacuum arc triggering mechanisms (Eslava, 2014)	27
Table 4-1 Experimental data control thrusters	60
Table 4-2 Comparison of simulation results and experimental data from Burton & Turchi (1998) for the LES 6 thruster.	62
Table 4-3 Comparison of simulation results and experimental data from Burton & Turchi (1998) for the LES 8/9 thruster.	64
Table 4-4 Simulation tests of initial voltage to capacitance ratio for a 5 W system	65
Table 4-5 Capacitance to peak discharge current comparison when varying the capacitance value and analysing the discharge current in Figure 4-17 and Figure 4-18.	67
Table 4-6 Aspect ratio simulation tests	68
Table 4-7 Preliminary design performance simulation results	72
Table 5-1 PPT geometry comparison	78
Table 5-2 XP Power E15 specifications	83
Table 5-3 Experimental prototype and preliminary design parameters	86
Table 5-4 Measured parameters for experimental prototype.....	90
Table 5-5 Additional input parameters for the numerical simulation on the experimental prototype.....	90
Table 5-6 Numerical simulation results of experimental prototype and preliminary design using the MATLAB® application.....	91
Table 5-7 Experimental charge/discharge sequence revision.....	92
Table 6-1 Experimental test descriptions	94
Table 6-2 DTMS design concepts	100
Table 6-3 Input parameters for thrust balance testing	106

Table 6-4 DTMS design iterations	114
Table 7-1 Experimental limitations	117
Table 7-2 Experimental design parameters	118
Table 7-3 Initial voltage discharge for Experiment 1 and Experiment 2	119
Table 7-4 Current discharge measurements for both experiment 1 and experiment 2, each consisting of six discharges tested at 0.75 Torr with an initial voltage ranging between 1170 V and 1200 V.	123
Table 7-5 Plasma resistance for experiments 1 and 2 when discharging at 1200 V	124
Table 7-6 PPT input parameters and plasma temperature for experiments 1 and 2.....	125
Table 7-7 Summary of plasma temperature results	126
Table 7-8 Experimental and numerical thrust values at 1200 V	128
Table A-1 Thruster Evaluation (Adapted from (Lun, 2008), (Scharlemann, et al., 2011), (Mueller, et al., 2010), (Zandbergen, 2013)).....	145
Table A-2 Final Comparisons of PPT, VAT and FEEP Thruster Systems	146
Table C-1 Orbital parameters simulation results during the first year in orbit	154
Table C-2 Orbital parameters during 10-day burn	155
Table C-3 Orbital parameters at higher altitudes.....	156
Table C-4 Orbital parameters during de-orbiting.....	156

List of Figures

Figure 1-1 Nanosatellite activity graph (De Carvalho, et al., 2020)	3
Figure 1-2 1U CubeSat structure	5
Figure 1-3 3U CubeSat structure	5
Figure 1-4 Basic Pulsed Plasma thruster layout with a description of the operating sequence	13
Figure 2-1 Basic rectangular breech-fed ¹ APPT concept.....	16
Figure 2-2 PPT geometry types	20
Figure 2-3 Rectangular breech-fed concept.....	21
Figure 2-4 Rectangular side-fed concept.....	21
Figure 2-5 Coaxial breech-fed concept	21
Figure 2-6 Coaxial side-fed concept (Burton & Turchi, 1998)	21

Figure 2-7 Pulsed Plasma thruster Spring Mechanism.....	25
Figure 2-8 Basic μ PPT power schematic (adapted from (Spanjers & et al., 2002))	26
Figure 3-1 Electromechanical model.....	30
Figure 3-2 Simplified RLC circuit model for PPTs	31
Figure 3-3 Uniform current flowing through electrode conductor.....	33
Figure 3-4 PPT electromagnetic overview	34
Figure 3-5 Pulsed Plasma Thruster magnetic field vectors. It should be noted that within figure (a), the dots and crosses represent the current direction through the electrodes, whereas the dots and crosses within figure (c) represent the magnetic field direction caused by the PPT.	35
Figure 3-6 Current density and Ampere’s law throughout the plasma surface sheet.....	36
Figure 3-7 Impact Parameter collision orbit (Hutchinson, 2001-2021)	40
Figure 3-8 Mass distribution loading parameter	41
Figure 3-9 Electromechanical System.....	44
Figure 3-10 Representation of Slug model.....	47
Figure 3-11 Representation of Snowplow model mass accumulation	48
Figure 4-1 MATLAB® One Dimensional model GUI overview	55
Figure 4-2 Electrical input parameters	56
Figure 4-3 Plasma Resistance input parameters	57
Figure 4-4 Thruster input parameters	57
Figure 4-5 Thruster geometry selection	58
Figure 4-6 Model Specification input parameter.....	58
Figure 4-7 Simulation modelling approach.....	58
Figure 4-8 Model validation checkbox.....	59
Figure 4-9 Simulation model dropdown list.....	59
Figure 4-10 Simulation results of the general electromechanical model	60
Figure 4-11 LES-6 experimental data and numerical model simulation comparison	62
Figure 4-12 LES-8/9 experimental data and numerical model simulation comparison	63
Figure 4-13 Efficiency-electrical test comparison.....	66
Figure 4-14 Exhaust velocity-electrical test comparison	66
Figure 4-15 Specific impulse-electrical test comparison	66
Figure 4-16 Delta-v- Electrical test comparison.....	66
Figure 4-17 High capacitance discharge	67

Figure 4-18 Low capacitance discharge	67
Figure 4-19 Efficiency-Dynamical test comparison.....	69
Figure 4-20 Exhaust velocity- Dynamical test comparison.....	69
Figure 4-21 Specific Impulse- Dynamical test comparison	69
Figure 4-22 Delta-V- Dynamical test comparison	69
Figure 4-23 Exceeded aspect ratio boundary example	70
Figure 4-24 Aspect ratio boundary example results	71
Figure 4-25 Numerical simulation for preliminary μ PPT design.....	71
Figure 4-26 Software architecture flow diagram.....	74
Figure 5-1 PPT geometry design considerations (Adapted from Burton & Turchi (1998)). (Top left) Design 1: Rectangular Breech-fed concept, (Top right) Design 2: Rectangular Side-fed concept, (Middle left) Design 3: Rectangular Breech-fed sandwich concept, (Middle right) Design 4: Coaxial Breech-fed concept, (Bottom left) Design 5: Coaxial three electrode concept, (Bottom right) Design 6: Coaxial side-fed concept.....	76
Figure 5-2 Marx circuit representation (Adapted from Eslava (2014)).....	79
Figure 5-3 Inductive Storage Unit (Adapted from Burton & Turchi (1998))	80
Figure 5-4 Capacitive energy storage unit (Adapted from (Spanjers & et al., 2002))	80
Figure 5-5 Extruded view of the preliminary PPT design.....	82
Figure 5-6 PPT power distribution concept.....	83
Figure 5-7 preliminary design of the main discharge circuit.....	84
Figure 5-8 Preliminary design of spark-igniter discharge circuit.....	84
Figure 5-9 Preliminary circuit design	85
Figure 5-10 Circuit layout for the experimental prototype using a mechanical triggering mechanism	87
Figure 5-11 XP Power E15 input to output ratio (Power, 2020).....	87
Figure 5-12 Circuit enclosure and mechanical trigger interface for experimental prototype testing	88
Figure 5-13 μ PPT operation sequence for both the charging and discharging of the main circuit and the spark-igniter circuit.....	88
Figure 5-14 Final experimental design.....	89
Figure 6-1 Experimental test setup for all equipment outside of the vacuum chamber	94
Figure 6-2 Experimental test setup for all components inside of the vacuum chamber.....	95

Figure 6-3 Circuit layout of experimental prototype to test both experiment 1 and experiment 2	96
Figure 6-4 Instrumentation setup of experimental prototype tests. This includes the voltage measurements for both the voltage discharge and current measurements.....	96
Figure 6-5 Implementation of current measuring shunt resistor into the experimental circuit	98
Figure 6-6 Parallel plate PPT current discharge path	99
Figure 6-7 DTMS design concepts. Concept (a) represents a pivoting balance. Concept (b) represents a strain gauge cantilever balance. Concept (c) represents a torsional pendulum. .	101
Figure 6-8 Cavendish experiment illustration	103
Figure 6-9 Torsion balance concept for a DTMS design (adapted from the cavendish experiment).....	103
Figure 6-10 Thrust balance GUI interface.....	106
Figure 6-11 Preliminary DTMS design concept	106
Figure 6-12 Schematic of preliminary DTMS design	107
Figure 6-13 Schematic of preliminary DTMS design	108
Figure 6-14 Final DTMS design layout.....	109
Figure 6-15 Description of inertia variables.....	110
Figure 6-16 general torsional balance oscillation characteristic ⁵	111
Figure 6-17 Thrust balance oscillation period measured data.....	112
Figure 6-18 Thrust balance oscillation error bars.....	112
Figure 6-19 Torsion pendulum rotation using a graded scale	113
Figure 7-1 Voltage divider used for initial testing. Figure (a) presents constructed voltage divider values. Figure (b) presents the implementation of the voltage divider into the experimental prototype circuit.....	118
Figure 7-2 Voltage over time curve of the experimental prototype using the voltage divider from Figure 7-1. The curve describes the high resistance and highly over-damped system..	119
Figure 7-3 Raw voltage over time data from oscilloscope when six 40 mm electrode tests (Experiment 1) discharged between 1180 V and 1200 V at 0.75 Torr.....	120
Figure 7-4 Raw voltage over time data from oscilloscope when six 25 mm electrode tests (Experiment 2) discharged between 1170 V and 1200 V at 0.75 Torr.....	120

Figure 7-5 Filtered voltage discharge over time data of the experimental prototype for both experiment 1 and experiment 2 when discharging at approximately 1200 V under 0.75 Torr.	121
Figure 7-6 Tektronix P5205 slope characteristic when measuring a square pulse waveform.	122
Figure 7-7 Raw current discharge over time data from oscilloscope. For figure (a), six 40 mm electrode tests (Experiment 1) discharged between 1180 V and 1200 V at 0.75 Torr. Similarly, figure (b), represents six 25 mm electrode tests (Experiment 2) discharging between 1170 V and 1200 V at 0.75 Torr.	123
Figure 7-8 Filtered current discharge over time data for both experiment 1 and experiment 2 when discharging at approximately 1200 V under 0.75 Torr.....	124
Figure 7-9 Plasma resistance over plasma temperature for dedicated aspect ratios (adapted from (Nada, Semtember, 2013)). The blue dotted line represents the added interpolated aspect ratio of 2.5 found within this thesis to the constructed graph by Nada.	126
Figure 7-10 Thrust to discharge energy evaluation at various pressure levels ($C = 6 \mu\text{F}$).....	127
Figure 7-11 Thrust extrapolation towards LEO pressure discharging at 1200 V.....	128
Figure 7-12 Plasma arc colour for experiments 1 and 2.....	129
Figure 7-13 Plasma arc colour for experiments 1 and 2. (a) Represents a PPT discharge of low initial voltage, low-pressure environment. (b) represents a PPT discharge of high initial voltage, high-pressure environment.	130
Figure 7-14 Experimental cathode electrode after all experiment 1 tests were conducted	131
Figure 7-15 Thrust to discharge energy evaluation for both experiments 1 and 2 when varying the electrode length and the discharge energy ($C = 6 \mu\text{F}$).....	131
Figure 8-1 μPPT experimental prototype with the estimated initial gas environment for main PPT discharge. The dots represent ionised molecules created after the initial spark-igniter discharge. The spark-igniters front face is placed perpendicular to the propellant discharge surface and electrode face, while placed in the outer cover of the μPPT	140
Figure B-1 PPT supporting cover.....	149
Figure B-2 PPT and spring support cover	150
Figure B-3 PPT cathode electrode.....	151
Figure B-4 PPT anode electrode.....	152
Figure B-5 PPT final design	153

Figure C-1 Orbital mission example of a 3U CubeSat using the performance parameters of the preliminary design μ PPT thruster within this thesis.....	158
Figure D-1 Experiment voltage divider.....	160
Figure D-2 Voltage divider implementation	160
Figure E-1 PCB base conforming to PC-104 standards	161
Figure E-2 LT Spice full-bridge DC-DC converter.....	162
Figure E-3 LTspice charge/discharge configuration	162
Figure E-4 Input pulse signal from EPS for charging	163
Figure E-5 Input pulse signal from EPS for discharging.....	163
Figure E-6 μ PPT charge/discharge cycles simulation.....	163

Nomenclature

a_{con}	Length of the connector (m)
a_{mir}	Length of the mirror (m)
h_e	Electrode separation height (m)
b_0	Impact parameter (m)
b_{con}	Width of the connector (m)
b_{mir}	Width of the mirror (m)
m_r	Reduced mass (kg)
v_r	Relative velocity (m/s)
I	Current discharge (A)
I_{Bit}	Impulse bit (c)
I_{counter}	Moment of inertia of the counterweight in the DTMS system ($\text{kg}\cdot\text{m}^2$)
I_{con}	Moment of inertia of the connector in the DTMS system ($\text{kg}\cdot\text{m}^2$)
I_{foil}	Moment of inertia of the foil sheet in DTMS system ($\text{kg}\cdot\text{m}^2$)
I_{inertia}	Moment of inertia ($\text{kg}\cdot\text{m}^2$)
I_{mir}	Moment of inertia of the mirror in the DTMS ($\text{kg}\cdot\text{m}^2$)
I_{PPT}	Moment of inertia of the PPT ($\text{kg}\cdot\text{m}^2$)
I_{rod}	Moment of inertia of the pendulum rod ($\text{kg}\cdot\text{m}^2$)
I_{SP}	Specific Impulse (s)
I_{T}	Total Impulse ($\text{N}\cdot\text{s}$)
K	Torsional constant
L'_{pe}	Inductance gradient
L_0	Initial system inductance (H)
E_0	Discharge Energy (J)
F_L	Lorentz Force (N)
V_0	Initial capacitor voltage (V)

V_{in}	Input voltage (V)
m_{bit}	Mass ablated per pulse ($kg \cdot s^{-1}$)
m_{con}	Mass of the connector in the DTMS system (kg)
m_{foil}	Mass of the foil sheet in the DTMS system (kg)
m_{mir}	Mass of the mirror in the DTMS system (kg)
m_p	Total propellant mass (kg)
m_{PPT}	Mass of Pulsed Plasma thruster (kg)
m_0	Initial current sheet mass (kg)
m_{rod}	Mass of pendulum rod (kg)
m_T	Total mass of accelerated current sheet (kg)
\dot{m}_f	Propellant mass flowrate (kg/s)
\dot{x}_s	Plasma sheet velocity (m/s)
M_0	Initial Spacecraft mass (kg)
M_f	Final Spacecraft mass (kg)
w_e	Electrode width (m)
h_e	Electrode gap height (m)
h	Electrode thickness (m)
v_e	Exhaust velocity relative to the spacecraft ($m \cdot s^{-1}$)
η	Thruster efficiency (%)
τ	Quarter of the ringing period (s)
α	Mass distribution loading parameter
C	Capacitance (F)
t	Time (s)
t_0	Initial Time (s)
t_f	Final Time (s)
P	Power (W)
E	Energy (J)
eV	Electron Volts (eV)
F_{PPT}	Applied force of PPT (N)
L_T	Total circuit Inductance (H)
R	Resistance (Ω)

R_{lim}	Current limiting resistor ($k\Omega$)
R_{rod}	Radius of torsion balance rod (m)
T	Plasma Temperature (K)
T_F	Thrust (N)
T_e	Electron Temperature (K)
$T_{oscillation}$	Oscillation Period (s)
$\bar{\bar{T}}$	Maxwell's stress tensor ($N \cdot m^{-2}$)
\bar{P}	Particle stress tensor ($N \cdot m^{-2}$)
\bar{g}	Photon momentum density ($kg \cdot m \cdot s^{-1}$)
\bar{p}	Particle momentum density ($kg \cdot m \cdot s^{-1}$)
τ_{force}	Torque generated on the pendulum due to the thrust force of the PPT ($N \cdot m$)
τ_{PPT}	The torque generated by the PPT on the pendulum ($N \cdot m$)
τ_{wire}	Torque due to torsion constant of wire ($N \cdot m$)
f	Pulse Frequency (Hz)
I	Discharge Current (A)
ρ	Ambient mass density distribution
φ	Expected satellite lifetime
α	Angle between pendulum rod and applied force ($^\circ$)
p	Spitzer Conductivity
θ	Pendulum rotation angle ($^\circ$)
B_{ext}	External magnetic field
B_{ind}	Self-Inductance field throughout the plasma sheet
1D	One-Dimensional
Ohm's Law	$V = I \cdot R$
ABS	Acrylonitrile Butadiene Styrene
ACSS	Attitude Control and stabilization System
APPT	Ablation Pulsed Plasma Thruster
AIT	Austrian Institute of Technology
CPUT	Cape Peninsula University of Technology
COTS	Components Off The Shelf

DTMS	Direct Thrust Measuring System
EP	Electric Propulsion
F'SATI	French South African Institute of Technology
FEEP	Field Emission Electric Propulsion
ITMS	Indirect Thrust Measuring System
IT	Ion Thruster
PERT	Project Evaluation Review Technique
PFN	Pulse Forming Network
PPT	Pulsed Plasma thruster
PSS	Plasma Stabilization System
PTFE	Polytetrafluoroethylene (Teflon)
VAT	Vacuum Arc Thruster
CDS	CubeSat Design Specifications
MHD	Magnetohydrodynamics
KVL	Kirchhoff's Voltage Law
RLC	Resistance-Inductance-Capacitance
ODE	Ordinary Differential Equations
GUI	Guided User Interface

Constants

Symbol	Name	Value (SI)
g	Gravity	$9.81 \text{ m}\cdot\text{s}^{-2}$
μ_0	Permeability of free space / Magnetic constant	$4\pi \times 10^{-7} \text{ N/A}^2$
k_B	Boltzmann's Constant	$1.38 \times 10^{-23} \text{ J}\cdot\text{K}^{-1}$
e	Electron charge	$1.6 \times 10^{-19} \text{ C}$
ϵ_0	Permittivity of free space	$8.85 \times 10^{-12} \text{ F}\cdot\text{m}^{-1}$
e/k_B	The temperature of 1 eV	11604 K

Chapter 1

Introduction

When considering the development required to improve nanosatellite capabilities, it should be taken into consideration that stringent work must be dedicated to the implementation of propulsion devices on these satellites. As space junk still proves to be a problematic area of concern, space entrepreneurs cannot allow the continuation of space vessels without means of being manoeuvrable. As technology improves and new theoretical concepts are developed, research institutions, which mostly have very strict budgets, should have the capability to test and evaluate these concepts for the development of space technology. Therefore, this work is dedicated to the development of a micro pulsed plasma thruster (μ PPT) for the use of the French South African Institute of Technology (F'SATI) satellite program at Cape Peninsula University of Technology (CPUT). Within this thesis, all the different aspects of the thruster are discussed. This includes the pulsed plasma theory, design considerations, and the electromechanical model. From this, an application is presented to simplify the cumbersome mathematical procedures needed to estimate thruster performance, inherently reducing design time. Furthermore, work is directed to the design, construction and testing of the μ PPT for the use on nanosatellites, more specifically CubeSats. To measure the thrust of the μ PPT, a thrust balance design is presented. Thereafter, the experimental results are presented and discussed. Within the introduction section, five sections are presented, namely:

- Background and motivation
- Aims and objectives
- Delineation of research outcomes
- Research methodology

- General overview of propulsion

From these sections, the research problem is clearly defined, the aims and objectives are presented, and the research methodology describes the approach to this project.

1.1 Background and Motivation

1.1.1 The Demand for Propulsion Systems for the New Space Age

With the beginning of the 21st century and the rapid development of technology, we have found ourselves in the midst of a new space era. Space mission milestones are dared to be challenged again and beyond. Research is currently conducted on missions back to the moon (McKay, 2013), colonizing Mars, building the starlink network (SpaceX, 2020) and developing a space tourism sector (Galactic, n.d.). As seen by these few examples, a new burning drive has hit the space industry, commonly now known as Space industry 4.0. For space missions to become more advanced and cost-effective, long-term manoeuvrability of space vessels is required. Although conventional chemical propulsion of rockets provides a desirable thrust for space missions, the specific impulse is quite small (Wertz, 1999). This essentially limits the number of times a spacecraft can manoeuvre. For this reason, quantitative and qualitative work must be dedicated to the development and optimization of propulsion systems for space vessels. Whether chemical or electric propulsion (EP) systems; propulsion development will be required to support the mission requirements of the new space age.

1.1.2 Growth of Nanosatellites and F'SATI MDA Project

Surprisingly, nanosatellites are not a new concept, although the term only appeared in 1992 for the first time (De Carvalho, et al., 2020). This can be seen in the historic time frame between the late 1950's and early 1970's when these small satellites were used to collect data and test different technologies and theories (Janson, 2011). As the 'new space' era arose, government and university projects led to an exponential growth in nanosatellite launch rates. By 2010, additional interest from the commercial market attending to the exploration of nanosatellite

technology was solidified with the addition of CubeSats. (De Carvalho, et al., 2020). To illustrate the growth of the nanosatellite industry, Figure 1-1 is presented.

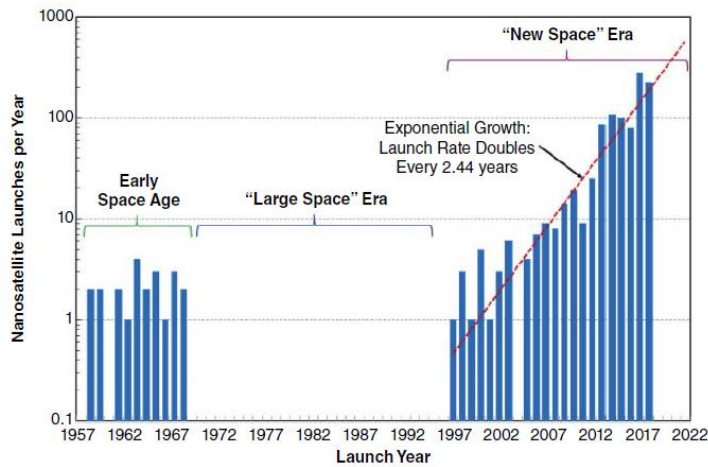


Figure 1-1 Nanosatellite activity graph (De Carvalho, et al., 2020)

Due to the commercial exploration and private sector growth in the nanosatellite industry, an appeal arose among institutions and the private sector. In 2008, F’SATI, in collaboration with CPUT, and ASIC (Africa Space Innovation Centre) started a space program to focus on the development of technology in the nanosatellite, more specifically CubeSat sector (F’SATI, 2020). After more than a decade of great success, they secured a contract with the South African government to support the Maritime Domain Awareness act of South Africa, hence the MDA project. This support consists of a monitoring system to detect the ships around the South African border, inherently securing more control over the ocean economy.

1.1.3 Industry Concerns on Nanosatellite Space Debris

In modern-day society, nanosatellites, and especially CubeSats, are becoming more common for the use of space missions. As CubeSats have demonstrated their functionality, reliability, and use for theoretical concept testing, they have become quite popular among start-up space companies and research institutions. Due to the fairly young addition of CubeSats to the space industry and the cohesion between space vessels and space law, it is found that limited de-orbiting restrictions currently exist. Hence, CubeSat regulations currently dictate a 25-year de-orbiting timeframe, while CubeSats are commonly designed for 3-5 years of operating time.

Therefore, it is clear that CubeSats become a member of the concerning space debris family, not only after they served their purpose, but at an alarming rate. Furthermore, as nanosatellites typically get launched in LEO (low earth orbit), atmospheric drag affects the velocity of the satellite. This inherently results in a decrease in satellite altitude, which can lead to a possible mission failure. Although propulsion systems already exist for these nanosatellites, it is found that they can cover more than half of the cost of the satellites. Due to the cost, start-up companies and research institutions commonly neglect these propulsion devices within their restricted budgets.

1.1.4 CubeSat Design and Specifications

In 1999, a collaborative effort between California Polytechnic State University (Cal Poly) and Stanford University arose to design a small satellite. The sole purpose of the project (CubeSat project) was to provide a standard for small satellites, reduce cost and deployment time, increase accessibility to space, and sustain frequent launches. Therefore, the CubeSat design specifications (CDS) were created. The CDS document dictates the minimum requirements that have to be met to satisfy the standards of the original design. This involves general requirements, mechanical, electrical, and operational requirements and holds the standard for all the different types of CubeSats (Poly, n.d.). It is important to note that all these ‘CubeSats’ are formed from the same 100 mm sided cubes, where every cube is referred to as a 1U as shown in Figure 1-2. Although the autological aspect of the word ‘CubeSat’ is self-explanatory, a CubeSat refers to a small satellite consisting of equal-sized cubes arranged in a certain configuration to form a satellite body (literally meaning a satellite built out of cubes). Thus, Figure 1-3 display a 3U CubeSat consisting of three 1U cubes stacked on top of one another.

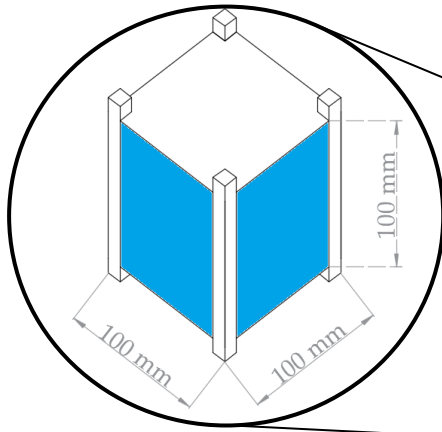


Figure 1-2 1U CubeSat structure

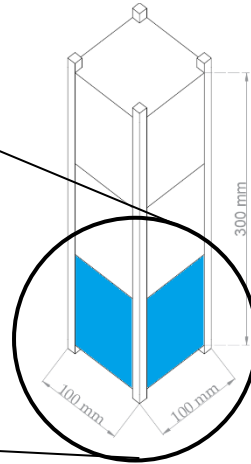


Figure 1-3 3U CubeSat structure

1.2 Aims and Objectives

The aim of this project is to design and develop a pulsed plasma thruster that can be used as the basis for future PPT development for F'SATI missions. Due to F'SATI focussing on nanosatellite missions, a survey was conducted to determine the most appropriate thruster for this work. From the survey results in appendix A, it was found that a micro pulsed plasma thruster (μ PPT) is best suited for future integration with CubeSat structures. Therefore, the thruster must conform to the standards developed by CalPoly and Stanford's CDS manual. Due to the limited space within these small satellite structures, the thruster is limited to only 1U of the CubeSat. As this project is divided into multiple areas of PPT development, a breakdown of the objectives is shown below for each design and testing section within this thesis. These sections include the numerical model used, the design process and experimental work.

1.2.1 Numerical Model

Within this thesis, a general electromechanical model is used within a MATLAB® software program to numerically estimate the performance of the thruster. Therefore, an application displays both the input parameters and the output performance parameters in a logical, user-friendly manner. For future work, the application interface incorporates additional thruster geometry types, as well as different modelling approaches.

Objectives:

- Write a software program for a numerical simulation model for thruster performance estimations
- Validate the numerical model to known thrusters
- Present the numerical model in a user-friendly application

1.2.2 μ PPT Design Stages and Experimental Work

The design and experimental work aim is to develop a μ PPT for experimental tests to form an initial foundation for future μ PPT development at F'SATI. As the conceptual design differentiates the preferred thruster type for this project, the preliminary design displays the most ideal design found from the numerical simulations conducted. Thereafter, experimental work leads to a practical understanding of the μ PPT operation, testing setups and system parameters.

Design Objectives:

- Compare various electrical and geometry configurations and conclude on the configurations chosen
- Design a preliminary power circuit based on the numerical simulation results
- Design a preliminary CAD model of the PPT geometry based on the numerical simulation results
- Design and construct an experimental PPT prototype

Experimental Objectives:

- Gain an understanding of the PPT operation and testing methodology
- Evaluate the μ PPT operating system and identify problems
- Measure and evaluate the voltage discharge of the system
- Measure and evaluate the current discharge of the system
- Determine the thrust of the μ PPT using a self-made thrust balance system and evaluate the results

1.3 Delineation of Research Outcomes

Numerical Model Simulation:

- Multi-fluid models are not incorporated in the simulations.
- Simulations exclude the effects of gas-dynamic forces.
- Only the general electromechanical model is used for numerical performance estimations.
- Simulations exclude the effect of operating pressure.
- Simulations will only estimate the performance results of parallel plate pulsed plasma thrusters.

Design

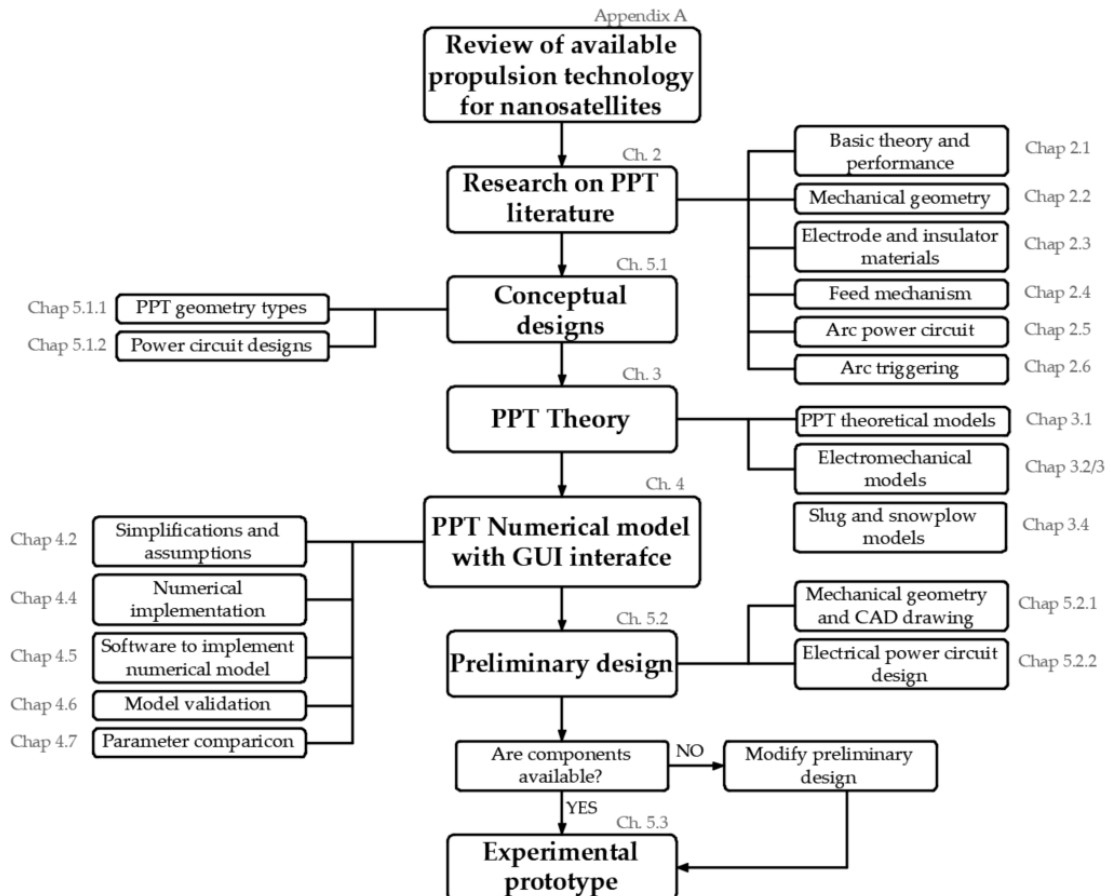
- For increased control and design simplicity, no complex circuitry was considered during this work. Rather, future PPT circuitry is recommended at the end of the thesis.
- Structural analysis will not be applied to the μ PPT. This includes stress and thermal analysis.

Experimental work:

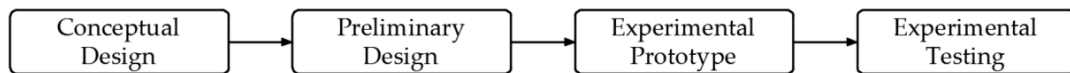
- No experiments are conducted under 0.75 Torr due to the limitation of the vacuum pump available at the time.
- The high voltage attenuator cannot be manually calibrated, therefore affecting the accuracy of the results.
- No electromagnetic high current measuring sensors are used. Due to the inability of acquiring these components, a shunt resistor is used instead.
- No plasma interferometry or spectroscopy tests are done for this thesis.

1.4 Research Methodology

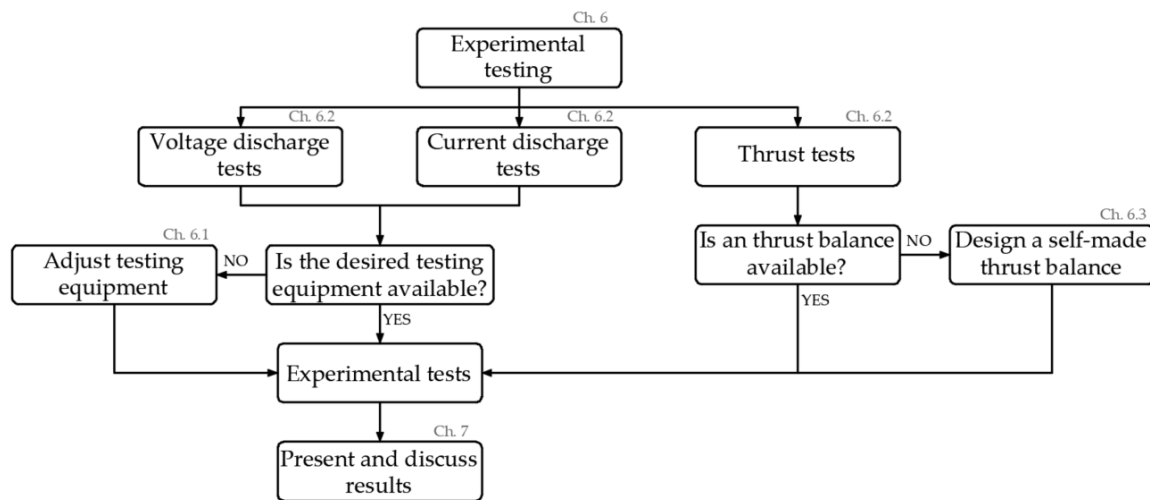
Within the flowchart presented below, the project approach is presented. Therefore, the order, as well as the project philosophy is presented clearly and logically.



Initially, a review of available propulsion devices is conducted to justify the use of a micro-pulsed plasma thruster for nanosatellite applications. A literature survey on pulsed plasma thrusters is thereafter conducted to identify critical system considerations. This leads to conceptual design evaluations to determine the PPT type and to introduce the appropriate PPT theory. Using the PPT theory, a numerical model is constructed to estimate thruster performance. Software development leads to a user-friendly software application. Furthermore, the numerical model is used to define the preliminary design parameters for both the electrical and mechanical sections of a μ PPT. Using the preliminary design parameters, combined with practical execution, an experimental prototype is presented. When strictly viewing the design and testing philosophy, it is represented by four distinctive steps, namely:



Testing is conducted on the experimental prototype to gain an understanding of the PPT operation, testing methodology and system characteristics. For a visual representation, the testing philosophy is represented by,



Within the experimental testing section, three distinctive tests are conducted: voltage discharge, current discharge and thrust measurements. These parameters are chosen due to their importance in defining system characteristics.

1.5 General Overview of Propulsion

1.5.1 Fundamental Propulsion Concepts

Before delving into different propulsion systems and their derivatives, it is quite important to understand the fundamental concepts used when working with these systems. Regardless of the type of thruster used, the working principle of a thruster follows Newton's third law of motion, stating that every action has an equal, but opposite reaction. Thus, it can be stated that the spacecraft is moving forward with the same force generated by the acceleration of the propellant

in the propulsion device. This force, or change of momentum throughout time, is referred to as **Thrust** and can be mathematically expressed as,

$$T_F = m \frac{dv_e}{dt} = \frac{dm}{dt} v_e \quad (1-1)$$

Where m , $\frac{dv_e}{dt}$, $\frac{dm}{dt}$ and v_e represent respectively, the mass of the spacecraft, the spacecraft acceleration, the rate of change of exhaust propellant, and the exhaust velocity relative to the rocket. Since the total impulse represents the maximum momentum that an engine can impart onto a vehicle, it is represented by,

$$I_T = \int_{t_0}^{t_f} T_F dt \quad (1-2)$$

Where I_T , t_0 and t_f represents the total impulse, initial time, and final time, respectively. For cases where missions require a larger impulse, a high exhaust velocity would rather be preferred than the excessive ejection of propellant mass (Jahn, 1968). Determining the ratio of the thrust to the amount of impulse that can be obtained per unit of reaction mass is called the **Specific Impulse** and can be expressed as (Wallangen, 2014),

$$I_{SP} = \frac{T_F}{\dot{m}_f g} = \frac{v_e}{g} \quad (1-3)$$

Where I_{SP} , \dot{m}_f and g represent the specific impulse, propellant mass flow rate, and gravitational constant at sea level, respectively. When analysing a spacecraft for orbital manoeuvres, it is important to determine the change in velocity necessary to conduct these manoeuvres. Since the propulsion system generates a force of motion, a change in velocity will be produced, Δv , which is famously known as the Tsiolkovsky ‘Rocket equation’ displayed as,

$$\Delta v = v_e \ln \left(\frac{M_0}{M_f} \right) \quad (1-4)$$

Where Δv , M_0 and M_f represent the change in velocity (Delta-V), original spacecraft mass, and the final spacecraft mass. Due to the exhaust velocity observed in both equation (1-3) and equation (1-4), a relationship exists between the specific impulse and the Δv .

1.5.2 Electric Propulsion Systems

Electric thrusters are generally best described by the means of the acceleration method used to produce thrust (Jahn, 1968) (Goebel & Katz, 2008). Due to the expansion of these methods throughout the last century, they can be divided into the following major categories, namely: electrostatic, electrothermal, and electromagnetic. These three categories can be distinguished from one another by their distinctive fundamental principles by which they create thrust.

Electrostatic:

The working principle of an electrostatic propulsion system makes use of electric fields to accelerate positively charged ionised gas. Thus, acceleration occurs due to electrostatic potentials. Ionisation occurs through a DC discharge, RF frequencies and electron synchrotron motion. Due to the positively charged particles used for acceleration, a neutraliser is required for the addition of electrons outside of the acceleration zone. (Ley, et al., 2008). This is simply to avoid the positive charge being attracted to the same source which caused it to accelerate. Results of this could lead to stalling of the thruster. When delving into the physics of the electrostatic engine and the explanation of (Fortescue, et al., 2011), acceleration is mainly caused by a Coulomb force and the static electric field is directed in the same direction as the acceleration.

Electrothermal:

Electrothermal thrusters operate by increasing the enthalpy of the propellant and converting it into kinetic energy through means of a nozzle (Fortescue, et al., 2011). This is done by using electromagnetic fields to generate plasma. This plasma is used to increase the temperature of the bulk propellant where the thermal energy is converted to kinetic energy (Kawnine & Kawnine, 2014). Electrothermal thrusters are thus still seen as true rockets, due to acceleration

being generated by the nozzle and converting the energy into linear motion. Hydrogen, Helium and Ammonia are typical propellants used for electrothermal thrusters (Fortescue, et al., 2011), where these thrusters can produce an I_{SP} of around 500 s to 1000 s (Kawnine & Kawnine, 2014).

Electromagnetic:

Electromagnetic thrusters are observed when electric and magnetic fields are applied to the system. This forces the ionised gas to accelerate outwards through a Lorentz force. Due to the neutral nature of the plasma created, no neutralization is required outside the acceleration zone (Choueiri, 2009). From the physical design arrangements shown in Figure 1-4, it is stated that the electric field vector is not in the direction of the accelerated material. This characteristic trademarks these devices as electromagnetic.

When considering a propulsion device, it is important to primarily focus on the mission and purpose of the thruster. Careful consideration should be directed to the precise requirements necessary, and the final objective should stay clear. Due to these considerations, a conclusion was made at the IEPC in 2011 that the PPT and the VAT are the best options for nanosatellite propulsion. These were chosen above the arcjet, hall thruster, gridded ion thruster, FEEP, micro-discharge thruster, colloid thruster, magnetoplasdynamic thrusters and other derivatives of these thruster types. This was due to the low power requirements, the potential for miniaturization, simplicity, and performance (Scharlemann, et al., 2011).

Within Appendix A, a propulsion survey was conducted on the available propulsion devices for nanosatellites. Within this survey, the different thruster models are listed, discussed, and compared to determine which thruster could best accomplish the requirements for future F'SATI missions. Within this survey, it was found that the micro pulsed plasma thruster is the best suited for this project. This is due to its vast history, low cost, simplicity, reliability, and other factors mentioned in the survey. Therefore, a thematic approach will be applied to μ PPTs from here on out and it will be regarded as the primary focus for the rest of the paper.

1.5.3 Pulsed Plasma Thrusters Overview

As previously mentioned, Appendix A contains a thruster survey to validate why the pulsed plasma thruster is best suited for this project. Within this survey, observations, comparisons, and validations were made on various thrusters.

A brief description of the general pulsed plasma thruster describes a device that creates thrust by accelerating ionised particles through the means of a Lorentz force. To do this, a potential is generated between two electrodes through a high-voltage capacitor. An initial spark triggers the ablation of solid propellant material causing a main discharge between the electrodes. This discharge causes a magnetic field to form, inherently accelerating the ionised gas outward. To visually grasp the concept of the PPT's operating sequence, Figure 1-4 is presented. From Figure 1-4, it is observed that the operating sequence consists of five steps, namely:

1. An initial spark from spark-igniter
2. Ablation of propellant occurs
3. A plasma sheet is created, closing the circuit
4. Main discharge is initiated
5. Plasma is accelerated by means of Lorentz force

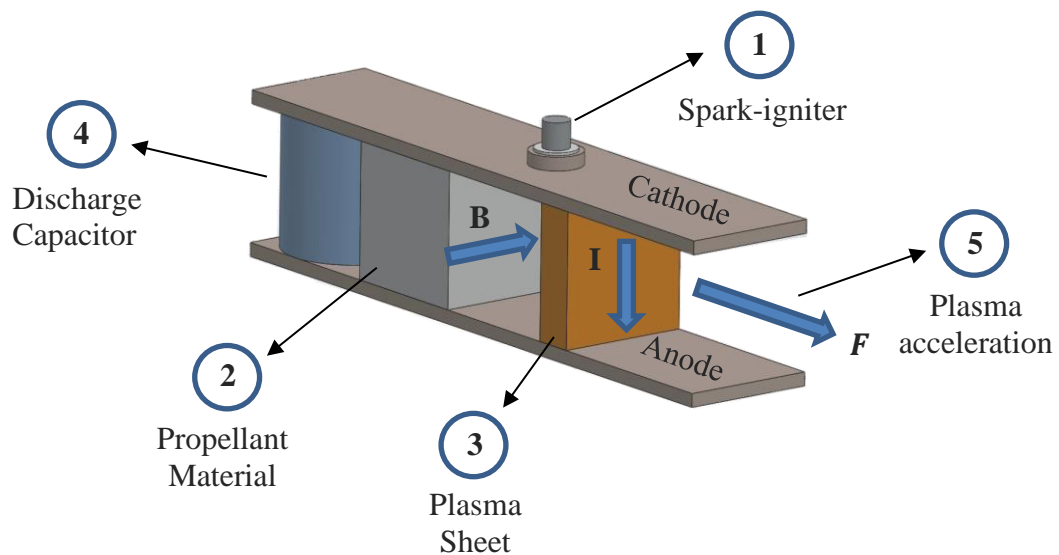


Figure 1-4 Basic Pulsed Plasma thruster layout with a description of the operating sequence

1.6 Summary

Within this chapter, a clear background and motivation were presented to serve as an introduction to the nanosatellite industry. Within this section, it was shown that there is a drastic increase in nanosatellite launches, while space junk remains to be a domain with minimal-to-nonviable solutions. Therefore, within the aims and objectives, the design of a pulsed plasma thruster was presented to serve as not only the basis for future development towards F'SATI satellite missions, but to mitigate future space debris via deorbit techniques and to account for orbital maintenance. To accomplish the project at hand, the research methodology was clearly defined, while running coherently with the delineation of the research outcome found prior. To end the chapter, an overview of propulsion was presented to define the necessary terminology and concepts necessary when working with a propulsion system.

Any reader not familiar with the fundamental concept of propulsion, electric propulsion systems and electro-magnetism, is advised to research the respective fields before reading this thesis.

Chapter 2

Literature Survey and Introduction to Pulsed Plasma Thrusters

This chapter briefly explains the working principle of a pulsed plasma thruster. This involves the general operation, design, and performance of a standard PPT model. Therefore, an introduction to the electromagnetic phenomena of the pulsed plasma thruster is discussed. Starting the chapter with an introduction to pulsed plasma thrusters, six parameters are discussed and presented which should be taken into consideration when designing a PPT. Thus, the basic PPT theory and performance, mechanical geometry, electrode and insulator materials, feed mechanism, arc power circuit, and arc triggering are discussed to gain knowledge of the methods and means to design a PPT. For any reader familiar with the literature on pulsed plasma thrusters, minimal attention can be directed toward this chapter.

2.1 Basic PPT Theory and Performance

The basic principles of a PPT operate on electromagnetic field theory. To better visualise the concept of an ablative pulsed plasma thruster (APPT), it can be stated that a traditional PPT consists of two electrodes (anode and cathode) joined by a dielectric in vacuum (commonly Teflon). These electrodes are joined by a charged capacitor in a vacuum and driven by a resistance-inductance-capacitance (RLC) pulse circuit as seen in Figure 2-1. A spark-igniter is used to generate a small amount of initial plasma, triggering a discharge over the exposed surface of the propellant. Due to this surface discharge, heat transfer allows evaporation of the

propellant to occur (Burton & Turchi, 1998). Furthermore, the ablation ionises the propellant and induces a thrust by accelerating the plasma outward by means of a Lorentz force (Cerdan, 2016). Due to the quasi-neutral state of the plasma, it allows for the abandonment of a neutralizing electrode (Burton & Turchi, 1998). Furthermore, due to the evaporation of propellant material during each discharge, a spring mechanism is inserted to ensure the propellant material is always pushed against the discharge region. As most PPTs use solid propellant material, the spring is the only moving part of the design. Solid propellant PPTs eliminate the need for propellant tanks, feed regulator systems and complex system control. This inherently simplifies the design and decreases the risk of failure. The various PPT components shown in Figure 2-1 will be described in detail throughout this chapter.

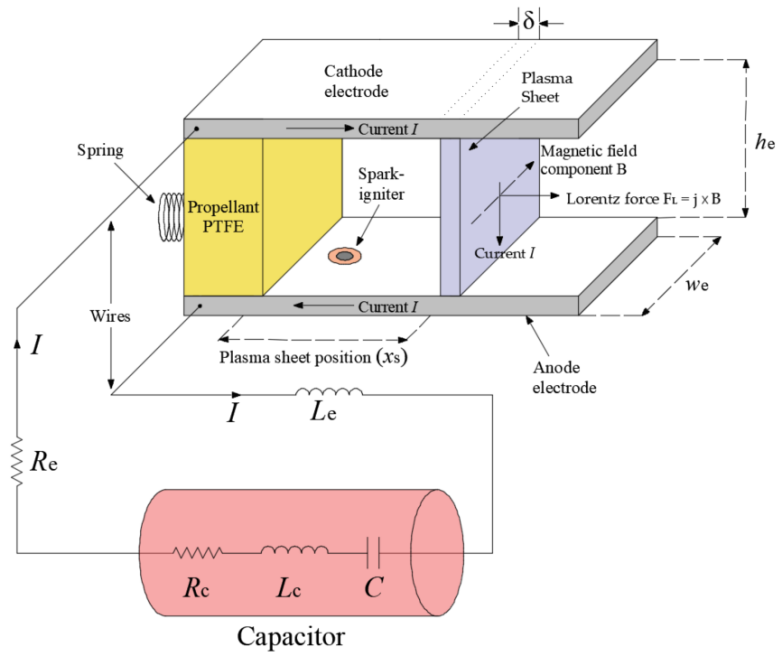


Figure 2-1 Basic rectangular breech-fed¹ APPT concept

Since the first glimpse of the pulsed plasma thruster in 1959, countless research has been conducted on methods to improve the thruster performance and how to determine the thruster's characteristics more accurately.

¹ Although clearly described in chapter 2.2, a breech-fed PPT is best described as an PPT with the thrust vector normal to the propellant surface. Therefore, the accelerated particles move perpendicular to the face of the propellant as a single unit. Examples of these thrusters is shown in Figure 2-3 and Figure 2-5.

Typical energy levels of flight PPTs can range anywhere from only a few joules to around one hundred joules (Scharlemann, et al., 2011), depending on the design parameters. With all parameters considered, it should be noted that most weight of a PPT is embedded into the electronic section. Approximately 40-45% of the total weight, solely lies in the hands of the high voltage capacitors used for creating the plasma (Hoskins & Cassady, 2000). Due to the demarcation of CubeSats, the capacitors are generally one of the main and most important focus points in the design phase of a μ PPT.

It is extremely important to notice that the amount of energy transferred to the propellant during discharge, strongly depends on the positioning of the spark-igniter. Therefore, not all of the energy transferred from the capacitor is directed towards the ablation of propellant material and therefore, wasted. Features of this unused energy can be found through heat transfer in the thruster and satellite framework in the form of conduction and radiation into space (Hoskins & Cassady, 2000). From the high plasma temperatures generated within a PPT, the specific impulse is far superior to the conventional chemical rockets, but as one can expect, it has its limitations. With inelastic scattering processes and electromagnetic radiation present, the electron temperature is limited to a few electron volts (eV). This affects the amount of energy transferred to heavy particles created during the ablation process and essentially reduces exhaust velocity. Therefore, exhaust velocity is associated with electrothermal operations. Comparing this statement to the high exhaust velocities observed in PPTs, it can be stated that the heating of heavy particles through plasma electrons should not exceed 25% of the total kinetic energy of these particles. It should rather be noticed that the high specific impulse occurs due to the electromagnetic force generated in these systems (Burton & Turchi, 1998). Since thrust is generated by high-velocity ions and slow-moving neutral gas particles, the exhaust velocity of the thruster is found to be below 10 km/s. Due to this low exhaust velocity, the efficiency of the PPT is limited to approximately 10% (Eslava, 2014). Although the exhaust velocity observed in PPTs is still considerably high, it should not be confused with the impulse-bit produced. As an impulse-bit represents the change of momentum caused by a single discharge pulse, μ PPTs generally deliver an impulse-bit in the order of micronewton-seconds (Lev, et al., 2019). When a rectangular breech-fed APPT (chapter 2.2) is considered, an estimation of the impulse-bit can be calculated by the expression (Scharlemann, et al., 2011),

$$I_{\text{Bit}} = \frac{L'_{\text{pe}}}{2} \int [I(t)]^2 dt \quad (2-1)$$

Where I_{Bit} , L'_{pe} , I represent the impulse-bit, inductance gradient formed by the ratio between the electrode gap height (h_e) and electrode width (w_e) from Figure 2-1, and current discharge, respectively. Iterating on the PPT construction, it is said that ablative pulsed plasma thrusters (APPT) consist of two electrodes (cathode and anode), a solid propellant block, a spring, spark-igniter, a capacitor, a power processing unit (PPU) and the support structure. All of these individual factors play a fundamental role in PPT performance, lifetime, system size and mission capabilities (Rezaeiha, 2014). Critical PPT design factors are presented in Table 2-1 below.

Table 2-1 Essential PPT performance design factors (Rezaeiha, 2014)

Geometrical parameters	Electrode Length, Width, Thickness
	Electrodes spacing
	Flare Angle (α)
	Electrode Shape (rectangular/co-axial)
	Aspect ratio (h_e/w_e)
Capacitor characteristics	Capacitance
	Internal resistance/inductance
	Discharge behaviour
	Maximum voltage
Propellant	Propellant face Area
	Propellant type (PTFE or other)
	Propellant temperature
Spark-igniter	Type
	Distance between spark and propellant face
	Spark Energy
	Plug discharge behaviour

Although the design parameters shown in Table 2-1 display the essential parameters when designing a PPT, it should not be forgotten that the geometry type, the propellant feeding type, the input power, thruster operating frequency and the electrode material are other factors to take into consideration (Rezaeiha & Schonherr, 2012). The general operating conditions and performance characteristics for a micro pulsed plasma thruster are presented below in Table 2-2.

Table 2-2. General μ PPT operating conditions and performance

Input Power	(1-20) W
Initial Voltage	(750-1750) V
Operating Frequency	(1-2) Hz
System Mass	(180-600) g
Avg. Thrust	(1-500) μ N
Specific Impulse	(300-1200) s
Impulse Bit	(10-80) μ Ns
Thrust/Power ratio	(0.1-25) μ N/W
Efficiency	(5-16) %

In 1968, Palumbo & Guman (1972) set out to develop a system case to analyse the flight operations of a PPT. In this study, which was conducted over a period of 10 years and 9000 hours of testing time, results displayed numerous characteristics (Burton & Turchi, 1998). These characteristics are seen as highly advantageous when used on nanosatellites. This includes:

- Zero warmup time, zero standby power.
- Inert and fail-safe – no unpowered torques or forces.
- Scalable to performance requirements.
- Usable on spinning or three-axis stabilized satellites.
- Discrete impulse-bits are compatible with digital logic.
- Variable thrust level.
- The performance is compatible with altitude control and station-keeping requirements.
- Operates at large variations in environmental temperature.
- Thrust vector control capability.

If solid propellant PPTs are used, additional advantages may be listed:

- No propellant tank requirements
- Feed lines are not required
- No seals
- No mechanical valves and valve operating systems required
- Much easier to determine propellant loss/consumption

- No zero-g propellant conditions
- Cryogenic temperatures considerations are N/A
- Vacuum capable
- Noncorrosive material
- Nontoxic
- Long shelf life
- Not affected by rapid temperature changes
- Not affected by variable ‘g’ loads

As solid APPTs hold many advantages, investigation steered into the use of these devices on microsattellites. This was due to their small impulse-bit, which inherently allows for precision control of satellite orientation and orbit maintenance (Keidar, et al., 2006). As PPTs can be scaled and adapted to different satellite dimensions and requirements (Lev, et al., 2019), their use in CubeSats could be a valuable and irrefutable advantage to future CubeSat missions.

2.2 Mechanical Geometry

Similar to the electric propulsion (EP) systems briefly discussed in Chapter 1.5.2, PPTs managed to develop their own derivatives throughout the years. Although PPTs are either gas-fed or solid propellant operated, due to a large number of additional advantages of APPTs (Chapter 2.1), the focus is directed to the design of an APPT for this thesis. Classifying different APPT geometry types by the means of a 2x2 matrix (Burton & Turchi, 1998), yields,

$$\begin{bmatrix} \text{Rectangular} \\ \text{Coaxial} \end{bmatrix} \cdot \begin{bmatrix} \text{Breech} & \text{Side} \end{bmatrix} = \begin{bmatrix} \text{Rectangular Breech} & \text{Rectangular Side} \\ \text{Coaxial Breech} & \text{Breech Side} \end{bmatrix}$$

Figure 2-2 PPT geometry types

Therefore, two primary PPT geometry types exist, namely: rectangular and coaxial configuration. From these configurations, they can be subdivided into either breech-fed or side-fed PPT thrusters. Additional derivatives of the rectangular and the coaxial thruster designs have been demonstrated in models such as the pinch model, described by (Jahn, 1968) or the

torque and flared models described by (Vondra, et al., 1971), although they are not of interest for this project. A visual representation of Figure 2-2 is presented below.

Rectangular Pulsed Plasma Thrusters

Rectangular Breech-Fed Thruster

Rectangular Side-Fed Thruster

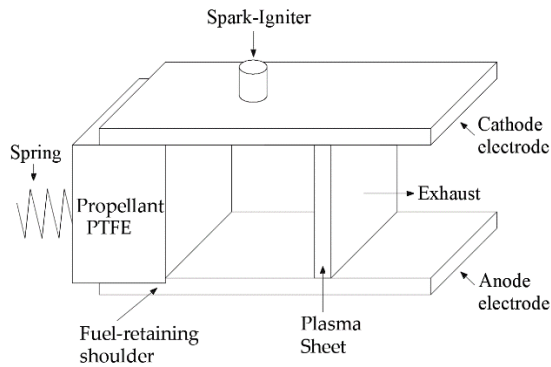


Figure 2-3 Rectangular breech-fed concept

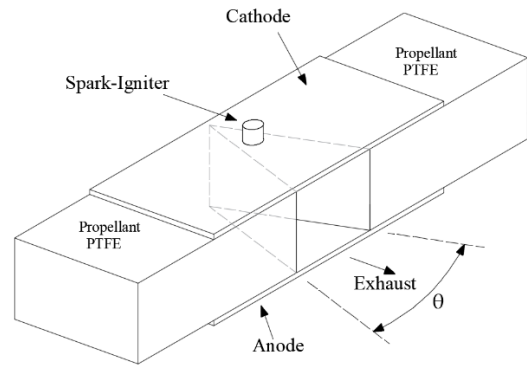


Figure 2-4 Rectangular side-fed concept

Coaxial Pulsed Plasma Thrusters

Coaxial Breech-Fed Thruster

Coaxial Side-Fed Thruster

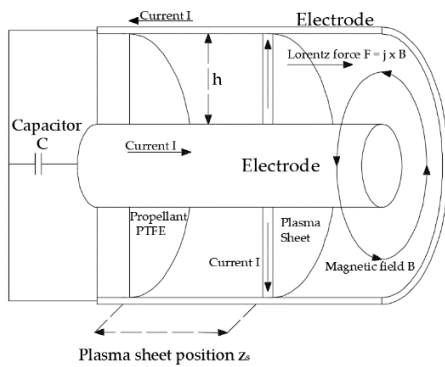


Figure 2-5 Coaxial breech-fed concept

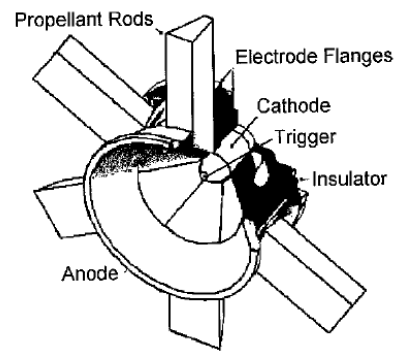


Figure 2-6 Coaxial side-fed concept (Burton & Turchi, 1998)

As shown above, Figure 2-3 represents the general rectangular breech-fed PPT. Although this geometry type is displayed at the beginning of chapter 2.1, the design entails two parallel electrodes placed at a desired distance from one another. As the propellant is placed between the two electrodes, the accelerated particles move perpendicular to the face of the propellant as a single unit (shown in chapter 3.4.1, slug model) and down the channel.

When viewing Figure 2-4, similarities can be drawn with the rectangular breech-fed thruster as both execute a parallel electrode configuration. The major difference between the rectangular breech and the side-fed thruster is that the side-fed thruster places the propellant material along the channel length instead of perpendicular to the channel as shown in Figure 2-3 and Figure 2-4. Therefore, it can be said that the accelerated gas accumulates as it transverse down the channel. This accelerated gas will be moving in the direction of the exhaust vector observed in Figure 2-4 and parallel to the face of the propellant (see chapter 3.4.2 in chapter 3 on snowplow models).

Figure 2-5 presents the co-axial breech-fed thruster. Similar to the rectangular breech-fed thruster, the propellant is placed between the two electrodes. The co-axial electrode configuration is circular, with one electrode in the centre of the thruster and the other electrode encompassing the propellant. It can be said that the accelerated gas moves perpendicular to the face of the propellant as a single unit and in the direction of the longitudinal axis of the channel (see chapter 3.4.1 in chapter 3 on slug models).

The co-axial side-fed thruster within Figure 2-6, represents the same operating concept as found for the co-axial breech-fed thruster. The major difference between the breech-fed and side-fed co-axial PPT is that the propellant is placed around and along the thruster and channel length, respectively. Therefore, the accelerated gas accumulates as it transverse down the channel (snowplow, chapter 3.4.2) and moves parallel to the face of the propellant.

A study conducted by Fortec (2006 - 2007) in collaboration with the Austrian Institute of Technology (AIT) set out to design a micro pulsed plasma thruster. Within their study, they found that although the different models of the parallel plate μ PPT functioned as a useful tool to verify the analytic model predictions, constant ignition issues terminated that area of investigation and turned their focus to coaxial μ PPTs. While comparing the results of the coaxial μ PPT to the parallel plate μ PPT, it was found that the reliability and specifically the lifetime of the thruster improved significantly when using the co-axial μ PPT. Upon that, due to its circular symmetry, less complicated measures were required to implement a third electrode as an ignition system (Scharlemann, et al., 2011).

2.3 Electrode and Insulator Materials

Since the dawn of PPTs, multiple propellants have been tested and evaluated to determine what materials deliver the best performance. These tests included solid, liquid and gas propellants and yet, only solid APPTs have been flight-qualified (Rezaeiha & Schonherr, 2012). Due to the success of these APPT thrusters, laboratory experiments focussed on using alternative propellant materials (Table 2-3) as a primary propellant for a PPT.

Table 2-3 Alternative PPT Propellant types (Rezaeiha & Schonherr, 2013)

State	Propellants
Solid	Fluorocarbons, Teflon sintered, seeded Teflon, composite propellants, powdered propellants
Liquid	Water, methanol, ethanol, butanol, dimethyl ether, mercury, gallium, lithium, caesium
Gas	Argon, nitrogen, xenon, water vapour

As researchers constantly aspire to find methods and tools to optimise a μ PPT, extensive work has gone into the effects of electrode and propellant materials to increase the performance of these thrusters. As the electrode material determines the conductivity and erosion resistance of the thruster, Rezaeiha & Schonherr (2012) suggested three types of electrode materials for the utilization in a μ PPT, namely, copper, brass, and molybdenum. A study by Kumagai et al. (2003) evaluated and compared the results of brass and molybdenum to determine how these materials would affect the μ PPT performance. Results from this comparison (Table 2-4) show that molybdenum yielded better performance results compared to the brass material. Due to the severe erosion rate of brass, uncertainty developed about its ability to operate on long-term missions.

Table 2-4 Brass and molybdenum performance comparison when used as electrode material

	Brass	Molybdenum
Energy (J)	3.6	3.6
I_{SP} (s)	1015	1129
I_{Bit} (μ N-s)	28	29.4
Mass shot (μ g)	2.44	2.66
Cathode erosion (μ g)	0.252	0.114
Anode erosion (μ g)	0.195	0.041
Thermal conductivity (W/mK)	106	139
Electrical resistivity (m Ω)	6×10^{-8}	5.6×10^{-8}
Specific heat (J/gK)	0.377	0.3
Melting Point (K)	1,173	2,883

Although copper was not directly compared to brass and molybdenum in Table 2-4, copper has proven to be a popular option for the use of pulsed plasma propulsion systems. This is due to the low resistivity, familiarity with multiple flight PPTs, and numerous test results. Since copper became common for the use of PPT electrodes, (Eslava, 2014) conducted tests on tungsten-plated copper electrodes. From the tests conducted, results showed that tungsten-plated copper displayed better electrical properties than regular copper.

Experiments by (Palumbo & Guman, 1976) focussed on using four thermoplastic materials such as Celcon, Halar, Tefzel, and in sintered Halon as alternative propellants to Teflon (Table 2-5). Additional experiments followed by evaluating the performance of Teflon seeded with InBr. Within this test, the performance was first measured with a Teflon/InBr ratio of 9:1 and thereafter with a Teflon/InBr ratio of 7:3 (Table 2-6). Results of all the tests concluded that although some materials such as Celcon, Tefzel and Teflon seeded InBr 7:3 ratio, showed some good characteristics, none of them produced characteristics comparable with pure Teflon (Rezaeiha & Schonherr, 2012).

Table 2-5 Solid Propellant Performance Comparison (Palumbo & Guman, 1976)

Propellant	Teflon	Celcon	Halar	Tefzel	Halon
Discharge Energy (J)	454	436	-	416	381
Thrust / Power (mN/kW)	21.07	17.91	-	16.05	17.47
I_{SP} (s)	5,170	5,500	-	8,410	5,100
η (%)	53.4	48.3	Charred	66.2	48.7

Table 2-6 Performance results of InBr₃/Teflon (Palumbo & Guman, 1976)

Propellant	100% Teflon	10% InBr ₃ / 90% Teflon	30% InBr ₃ / 70% Teflon
Discharge Energy (J)	390	387	400
Thrust / Power (mN/kW)	20.14	20.45	19.47
<i>I</i> _{SP} (s)	4,610	4,500	4,901
η (%)	45.4	45.1	38.3

2.4 Feed Mechanism

APPTs generally consist of electrodes, propellant, a spark-igniter, a spring mechanism, and additional circuitry, thus, minimal moving parts contribute to the thruster. This inherently simplifies the system and reduces risk, increasing the appeal for the use of the PPT on nanosatellites/CubeSats. From the ablation of propellant with each pulse, loss of propellant can easily be observed (Jahn, 1968). This causes a gradual displacement of the propellant surface discharge position relative to the spark-igniter, inherently altering the system. Generally, a solution to this problem consists of inserting a spring mechanism behind the propellant bar to ensure that the propellant face is against the discharge region as shown in Figure 2-7. This essentially eliminates the complications involved with moving parts (Eslava, 2014).

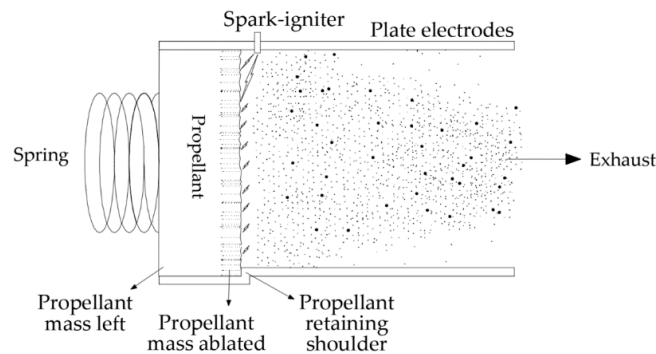


Figure 2-7 Pulsed Plasma thruster Spring Mechanism

As the characteristics of each thruster may differ depending on the mission at hand, the abandonment of the spring mechanism on an APPT is plausible. Many reasons can motivate why these spring mechanisms are excluded in the design of an APPT, where the feed rate (the propellant used per unit time) compared to the mission timeline is one of them (Lun, 2008).

2.5 Arc Power Circuit

Unlike the inductive energy storage circuit commonly used in vacuum arc thrusters (VAT), PPT circuits operate through a capacitive energy storage circuit (Schein, et al., 2007). Although inductive drivers have the advantage of higher pulse rates, lower voltages, and better control over the current, capacitor drivers can produce a high current at short pulses. This characteristic results in less heat dissipation during capacitor charge-up (Lun, 2008). To charge the capacitors, a high-voltage DC source is required. Commonly, high voltage DC-DC converters are used for capacitor charging. Typically, voltages range between 700 V and 2000 V to achieve voltage breakdown of the electrode gap (Rezaeiha,2014; Rezaeiha & Schonherr, 2012; Eslava, 2014). Depending on the satellite type, nanosatellites generally supply a bus voltage range between 3 V – 28 V, although small CubeSat bus voltages commonly supply 3.3 V, 5 V and a maximum of 12 V (Space, 2019). A simple diagram of this requirement is presented in Figure 2-8.

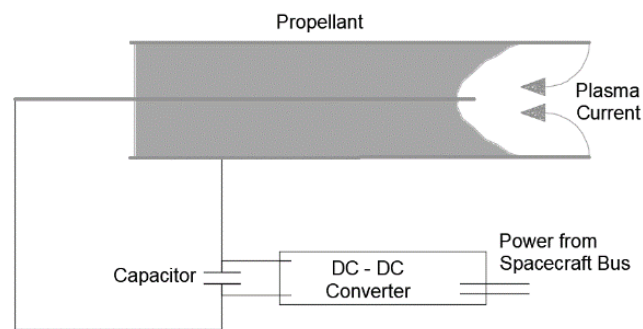


Figure 2-8 Basic μ PPT power schematic (adapted from (Spanjers & et al., 2002))

2.6 Arc Triggering

When considering the main discharge circuit of a μ PPT in space, a clear problem occurs. Due to the high dielectric strength observed in the vacuum of space, no conducting medium is available for a discharge arc to form. To create a conducting path for the electrons to flow between the cathode to the anode, a field emissions mechanism is used for electrical breakdown (Eslava, 2014). For this reason, trigger mechanisms have been developed to create an initial conducting layer through which the discharge arc can flow. A summary of vacuum arc

triggering mechanisms were constructed by (Eslava, 2014) and is presented in Table 2-7. From all the triggering mechanisms, it is found that the ‘triggerless’ vacuum arc ignition is the most commonly used. Speculation as to why this method is commonly used led to the ease of operation, reliability, space heritage, high repetition rate, the PPT operating at lower voltages, and only requires an arc switch and booster circuit. Apart from the advantages of using this mechanism, research by (Aston & Pless, 1981) showed that when the spark-igniter is placed directly into the cathode electrode, the spark-igniter suffered severe erosion after multiple discharges. To counter this, they proposed insulating the spark-igniter from the cathode electrode and adding a coupling element between them. Two coupling methods were identified, namely: resistive coupling and inductance coupling. Results of the resistive coupling found a decrease in deposition on the spark-igniter, where results of the inductance coupling showed a limitation of the coupling current. Therefore, the charging of the inductor has a damping effect on the current, essentially decreasing spark-igniter erosion.

Table 2-7 Vacuum arc triggering mechanisms (Eslava, 2014)

Triggering Mechanisms	Advantages	Disadvantages
High-Voltage Vacuum Breakdown	No contamination of metal plasmas	Requires a high voltage, breakdown voltage changes with electrode conditioning, not usable for repetitive mode operation.
Fuse Wire Explosion	No contamination of metal plasmas	Not usable for repetitive mode operation.
Contact Separation	Reliable, Simple, Repeatable	Low repetition rate, contacts may weld
Mechanical Triggering	Reliable, relatively simple (depending on actuator mechanisms)	Low repetition rate, contacts may weld and wear, a limited number of triggering events (less than 10^4 pulses) large jitter
High-Voltage Surface Discharge	High repetition rates, reliable typically up to 10^5 pulses, low jitter	Needs high voltage pulser, fails when approaching 10^5 pulses, plasma contamination by erosion of insulator
Plasma Injection Triggering	No trigger supply	Needs significantly high pressure in the discharge vicinity, metal plasma contamination by gas species, very large jitter
Low-Voltage or ‘Triggerless’ vacuum arc initiation	Reliable for 10^5 pulses, simple, high repetition rate possible, works without high voltage	Needs arc switch and moderate ‘booster’ voltage, may fail for low melting point and easily oxidizing cathode materials

Due to the effects of triggering mechanisms affecting the required breakdown voltage, rare ignition requirements up to 50 kV have been found necessary (Cerdan, 2016). Generally, ignition voltages range between 700 V – 2000 V (Rezaeiha, 2014) (Eslava, 2014). Although the simplicity, reliability, and lower operating voltages of the triggerless mechanism seem quite appealing, other limiting factors such as spark-igniter size, weight, additional booster circuits and power availability from the satellite bus need to be taken into consideration (Eslava, 2014).

2.7 Summary and Conclusion

Within this chapter, an introduction to pulsed plasma thrusters was presented. To understand the working principle and various design considerations of a pulsed plasma thruster, six primary focus points were discussed. Within the mechanical geometry section, it is stated that four APPTs can be used for PPT operation. From these four geometries, only the breech-fed PPT have successfully been flight operated. Furthermore, it is found that copper electrodes are the overall choice of electrode material, whereas Polytetrafluoroethylene displays the best performance characteristics out of all the propellants evaluated. Due to the simplicity of the APPT, no moving parts are found, except for a spring which is generally inserted to keep the propellant face within the discharge region. Therefore, a spring is generally inserted to keep the propellant face within the discharge region. Between the inductive energy storage unit and capacitive storage unit, it is found that capacitive storage units are the preferred method due to their ability to produce a high current at short pulses. Within the arc triggering section, multiple triggering methods are presented. From all the methods, it is found that the triggerless vacuum arc ignition is best suited due to its simplicity, reliability and only requires an arc switch and voltage booster.

Chapter 3

An Introduction to Parallel Plate Pulsed Plasma Theory

Within this section, the general electromechanical model derived by (Jahn, 1968) and adapted by (Laperriere, 2005) is presented as an electrical circuit interacting with a mechanical system. The electrical circuit is theoretically idealized as an RLC circuit with discrete, albeit movable elements. The electromechanical model is divided into five model segments to clearly define the various aspects of the model. Therefore, the self-induced magnetic field, parallel plate inductance model, dynamical model, plasma resistance model, and mass distribution model are presented. Thereafter, an improved electromechanical model from (Laperriere, 2005) is presented which considers additional external applied magnetic fields. To define the method by which the accelerated mass is modelled, the slug and snowplow models are introduced. As the slug model represents a case in which the entire mass is accumulated at the point of breakdown, the snowplow model represents an impermeable absorbing surface accelerating down the channel, essentially accumulating all mass overtaken by it. To end the chapter, a summary is presented.

For any reader familiar with the pulsed plasma thruster and the theoretical models associated, minimal attention can be directed towards this chapter.

3.1 A General Survey of Pulsed Plasma Models

To simulate the performance characteristics of a μ PPT, analytical and numerical models have been developed. These theoretical models can be observed from the simplest one-dimensional model by Jahn (1968), to the more advanced magnetohydrodynamic modelling of Mikellides,

(Mikellides, P.G.; Turchi, P. J., 1995). Practical examples of these models are discussed by both Laperriere (2005), who focussed on designing an improved version of the one-dimensional model first seen by Jahn (1968) and Wallangen (2014), who focussed on analysing the characteristics of the thruster by means of an analytical approach. Although both approaches proved sufficient, due to the non-linear nature of the PPT model as well as the continuous challenge to accurately determine plasma characteristics, numerical methods offer a simplified solution to these complex mathematical models. As experiments are cost-intensive, numerical methods are frequently used for μ PPTs and allow for the determination of relevant system parameters to improve system performance (Ou, et al., 2018). To determine these system parameters, the electromechanical model is frequently used. This is due to the simplicity of the model and ease of modelling steps which inherently reduces simulation time compared to the magnetohydrodynamic (MHD) model (Ou, et al., 2018). From Figure 3-1, it can be observed that the electromechanical model is represented by a combination of an electrical and a mechanical system. The electromechanical model first appeared in (Hart, 1962) which was followed by the one-dimensional mathematical models of (Jahn, 1968).

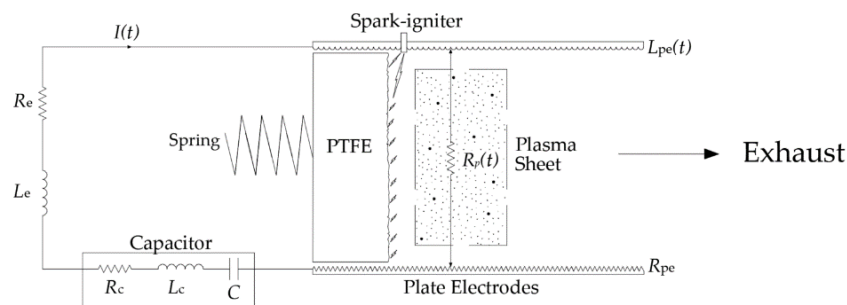


Figure 3-1 Electromechanical model

As described by Jahn (1968), multiple models exist within the one-dimensional model. These design approaches include the slug model, snowplow model, multifluid models, gas-dynamic models and the additional magnetohydrodynamic model seen by (Mikellides, P.G.; Turchi, P. J., 1995). Although advanced models such as multifluid models and gas-dynamic models can be used, they appear unnecessary as models such as the slug and snowplow deliver sufficient results for this type of system (Nada, Semtember, 2013), (Ziemer & Choueiri, 2001).

3.2 General Electromechanical Model for a Parallel-Plate PPT

To describe the electrical contribution to the system, we have to refer back to a statement made by R. H. Lovberg back in 1968. In this statement made on ‘Plasma technology’, he stated that the narrow arc current layers observed in unsteady electromagnetic accelerators are theoretically ideal when these layers are represented by a discrete, albeit movable series RLC circuit (Lovberg, 1968). For a visual representation, a basic RLC circuit is displayed in Figure 3-2.

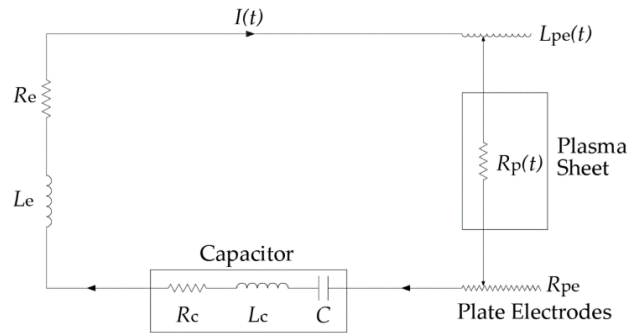


Figure 3-2 Simplified RLC circuit model for PPTs

From Figure 3-2, the total inductance of the system is the summation of all the inductance-generating components in that system ($L_T = L_c + L_e + L_{pe}$). Stating that, L_c , L_e and L_{pe} represent, respectively, the capacitor inductance, the wire and leads inductance and the electrode inductance. Similar to the inductance in the system, the total resistance can be represented by $R_T(t) = R_c + R_e + R_{pe} + R_p(t)$, where R_c , R_e , R_{pe} and $R_p(t)$ represent, the capacitor, wire and leads, electrode and plasma resistance. Using Kirchhoff's Voltage Law (KVL), the dynamics of the circuit can be represented by,

$$V_c + \frac{d}{dt}(L_T I) + R_T I = V_0 - \frac{1}{C} \int_0^t I(\tau) \cdot d\tau - \frac{d}{dt}[(L_0 + L'_{pe} x_s) I] - R_T I = 0 \quad (3-1)$$

where V_c , I , V_0 , C , L_0 , L'_{pe} and x_s represent the voltage across the capacitor, circuit current, initial capacitor voltage, capacitance, initial system inductance, inductance gradient and current sheet position. Generally, the inductance gradient L'_{pe} is not known, but through analytical expressions, several estimations have been developed (Scharlemann, et al., 2011). An example of this can be seen by the inductance gradient approximation equation from (Jahn, 1968), stating that if the width of the parallel plate electrodes is sufficiently larger than the height between the electrodes ($w_e \gg h_e$), then the inductance gradient can be represented by,

$$L'_{pe} \approx \mu_0 \frac{h_e}{w_e} \quad (3-2)$$

where h_e , w_e and μ_0 represents the electrode separation distance and the electrode width and the permeability of free space ($4\pi \times 10^{-7} \text{ N/A}^2$). Since the discharge current causing the acceleration of the plasma is in itself dependent on the position and velocity of the movable circuit element, the dynamical system is non-linear (Jahn, 1968). From this, Jahn's dynamical model was written in terms of Newton's second law as

$$\frac{d}{dt} [m_T \dot{x}_s(t)] = \frac{1}{2} \mu_0 \frac{h_e}{w_e} [I(t)]^2 = \frac{L'_{pe}}{2} [I(t)]^2 \quad (3-3)$$

where m_T and \dot{x}_s represents, respectively, the total mass accelerated and the velocity of the plasma sheet. Equations (3-1) and (3-3) are simultaneous equations in $I(t)$ and $x_s(t)$ in terms of parameters V_0 , m_T , h_e , w_e , L_0 , L'_{pe} , and C when R_T is presumed constant throughout the process. This specific model neglects the effects of gas-dynamic forces. Since Jahn's model assumed that the plasma would accelerate as a single unit ('Slug model'), no mass is accumulated and is considered constant ($m_T = m_0$). To better understand how equations (3-1) and (3-3) represent the general electromechanical model for a parallel-plate PPT, a derivation of the model is required. Within this derivation, attention is drawn to the self-induced magnetic field, inductance model, dynamical model, plasma resistance model and mass distribution model as these areas play a major role in the performance characteristics of the thruster. Applying Faraday's law of induction to the circuit yields,

$$V_c(t) = IR_T(t) + \frac{d}{dt} [\lambda_{PPT}(t)] \quad (3-4)$$

where λ_{PPT} represents the total flux linkage through the system. Writing the flux linkage in terms of its individual components yields,

$$\lambda_{PPT}(t) = \lambda_c(t) + \lambda_e(t) + \lambda_{pe}(t) \quad (3-5)$$

Where $\lambda_c(t)$, $\lambda_e(t)$ and $\lambda_{pe}(t)$, represents the magnetic flux linkage due to the capacitor inductance, the leads-and-wires inductance, and the electrodes. Rewriting equation (3-5) in terms of capacitance and leads-and-wires self-inductance (Laperriere, 2005), shows,

$$\lambda_{\text{PPT}}(t) = L_c I(t) + L_e I(t) + \iint_{\text{electrodes}} \mathbf{B}_{\text{ind}}(x, y) \cdot d\mathbf{A} \quad (3-6)$$

Where \mathbf{B}_{ind} and $d\mathbf{A}$ represent, respectively, the self-induced magnetic field through the plasma sheet and an area vector. Now that the basic equations of the electrical model have been established ((3-4)-(3-6)), details of the self-induced magnetic field, the inductance model, the dynamical model, the plasma resistance model, and the mass distribution model will be discussed.

3.2.1 Self-Induced Magnetic Field

To determine the effect of the magnetic fields on the system, the system is divided into three sections. As the electrodes are considered as ‘*perfect conductors*’, this simplification implies a quasi-infinite width ($w_e \gg h$) of uniform current within the electrodes as shown in Figure 3-3, an infinite plasma conductance, and the exclusion of any fringe effects.

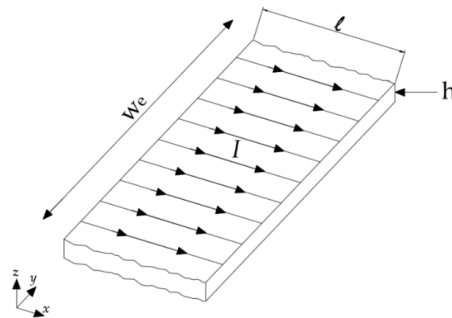


Figure 3-3 Uniform current flowing through electrode conductor

Figure 3-4 shows three magnetic sections/regions as follows: the magnetic field between the propellant and plasma sheet (region 1), the magnetic field within the plasma sheet (region 2) and the magnetic field in front of the approaching face of the plasma sheet (region 3).

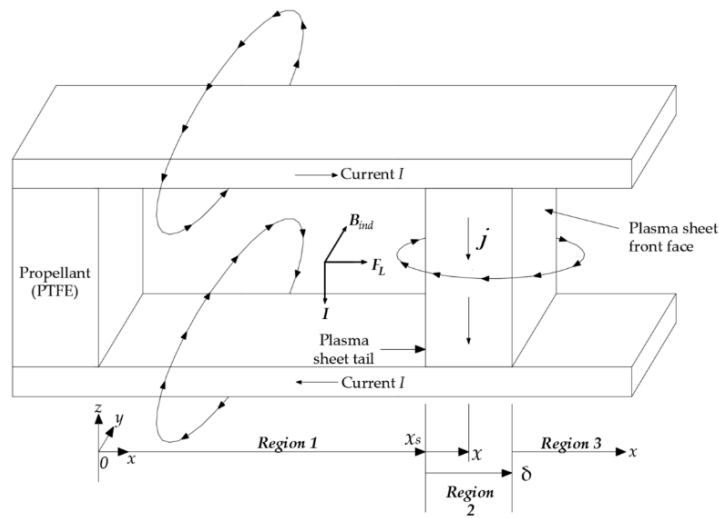


Figure 3-4 PPT electromagnetic overview

Therefore, to determine the magnetic field between the propellant surface and the tail of the plasma sheet ($0 < x < x_s(t)$), we use the divergenceless property of the magnetic field and Ampere's law,

$$\nabla \cdot \mathbf{B}_{\text{ind}} = 0 \quad (3-7)$$

$$\nabla \times \mathbf{B}_{\text{ind}} = \mu_0 \mathbf{j} \quad (3-8)$$

Furthermore, writing Amperes law into integral form yields,

$$\oint \mathbf{B}_{\text{ind}} \cdot d\mathbf{l} = \mu_0 I_{\text{enclosed}} \quad (3-9)$$

where \mathbf{j} and I_{enclosed} represent, respectively, the current density vector and the current in a closed loop formed by the external capacitor, leads, together with the upper and lower conductor and the plasma. Since the inner magnetic field vector for both the cathode and anode is directed in the same direction (Figure 3-5-(b)), a summation of the magnetic fields is to be expected.

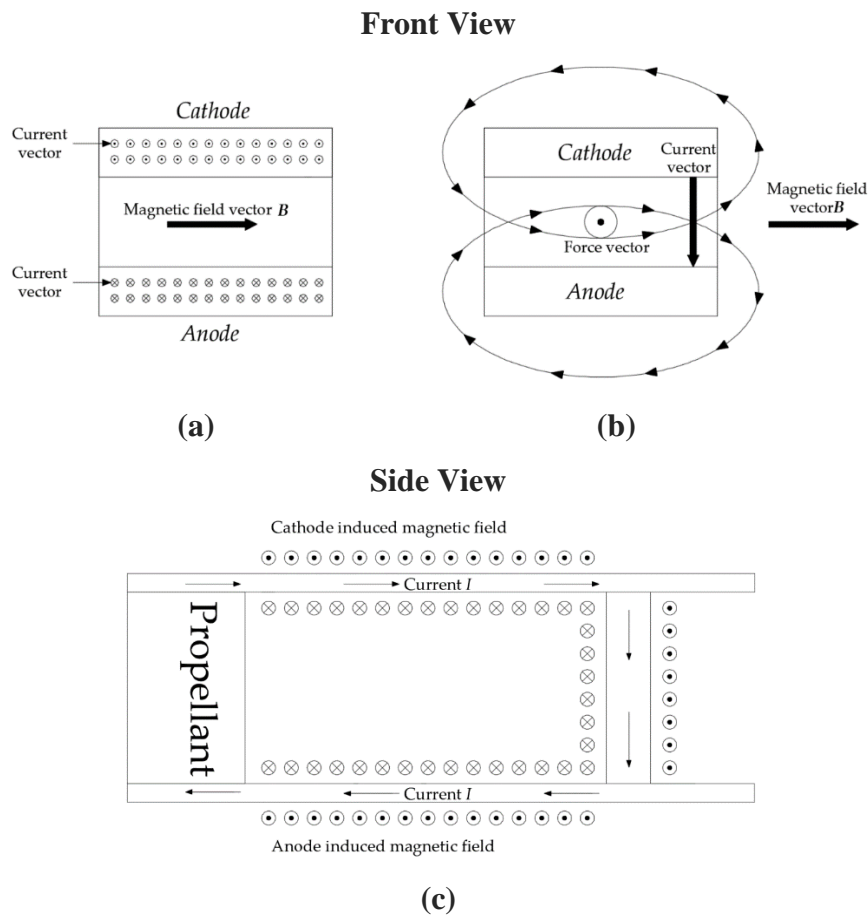


Figure 3-5 Pulsed Plasma Thruster magnetic field vectors. It should be noted that within figure (a), the dots and crosses represent the current direction through the electrodes, whereas the dots and crosses within figure (c) represent the magnetic field direction caused by the PPT.

Therefore, when both the cathode and anode electrodes have a quasi-infinite width while the total magnetic field is a summation of both these electrodes, the magnetic field within region 1 is presented as,

$$\mathbf{B}_{\text{ind}} = \mu_0 \frac{I}{w_e} \hat{y} \quad (3-10)$$

The above can be derived by assuming region 1 is the inside of a very long solenoid formed by a current sheet in the upper conductor, lower conductor and the plasma. This formula is derived from many books on electromagnetic theory.

To determine the magnetic field within the plasma sheet (region 2 in Figure 3-4), we apply Ampere's law to a surface passing through the plasma sheet (as shown by the shaded area in

Figure 3-6), while using the magnetic field as if the fields are generated by the inner core of a solenoid as a boundary condition.

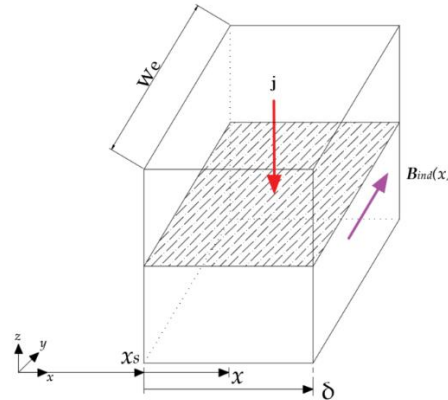


Figure 3-6 Current density and Ampere's law throughout the plasma surface sheet

When a uniform current density is considered throughout the current sheet,

$$\mathbf{j}(t) = \frac{I(t)}{w_e \delta} \hat{\mathbf{z}} \quad (3-11)$$

the magnetic field within the current sheet is shown to be

$$\mathbf{B}_{\text{ind}}(x, t) = \mu_0 \frac{I(t)}{w_e} \left[1 - \frac{x - x_s(t)}{\delta} \right] \hat{\mathbf{y}} \quad (3-12)$$

As observed in Figure 3-5(c), when the plasma sheet accelerates down the channel, the current in the upper and lower conductors in Figure 3-4 does not flow past the plasma. Therefore, the contribution of the magnetic fields generated in front of the front face of the plasma ($x > x_s(t) + \delta$) in region 3 can be neglected. When considering all three regions, the magnetic fields of the PPT are represented by,

$$\mathbf{B}_{\text{ind}}(x, t) = \begin{cases} \mu_0 \frac{I(t)}{w_e} \hat{\mathbf{y}}, & 0 < x < x_s(t) \\ \mu_0 \frac{I(t)}{w_e} \left[1 - \frac{x - x_s(t)}{\delta} \right] \hat{\mathbf{y}}, & x_s(t) < x < x_s(t) + \delta \\ 0, & x < x_s(t) + \delta \end{cases} \quad (3-13)$$

3.2.2 Parallel Plate Inductance Model

When the self-induced magnetic field from equation (3-13) is substituted into equation (3-5) for the flux linkage, we get

$$\lambda_{\text{PPT}}(t) = L_c I(t) + L_e I(t) + \int_0^{x_s(t)} \int_0^{h_e} \mu_0 \frac{I(t)}{w_e} dy dx + \int_{x_s(t)}^{x_s(t)+\delta} \int_0^{h_e} \mu_0 \frac{I(t)}{w_e} \left[1 - \frac{x - x_s(t)}{\delta} \right] dy dx \quad (3-14)$$

By integrating the induced magnetic fields within equation (3-14), the self-inductance of the parallel plate electrodes can be found in the last two terms of equation (3-15).

$$\lambda_{\text{PPT}}(t) = L_c I(t) + L_e I(t) + \left[\mu_0 \frac{h_e}{w_e} x_s(t) + \mu_0 \frac{\delta}{2} \frac{h_e}{w_e} \right] I(t) \quad (3-15)$$

Evaluating the last two terms (in brackets) show,

$$L_{\text{pe}}(x_s(t)) = \frac{\lambda_{\text{pe}}(x_s(t))}{I(t)} = \mu_0 \frac{h_e}{w_e} x_s(t) + \mu_0 \frac{\delta}{2} \frac{h_e}{w_e} \quad (3-16)$$

Simplifying the system by reducing the plasma sheet thickness to an infinitesimally small sheet thickness ($\delta = 0$), leads to

$$L_{\text{pe}}(x_s(t)) = \mu_0 \frac{h_e}{w_e} x_s(t) \quad (3-17)$$

By enforcing this simplification, equation (3-17) is consistent with the work done by (Jahn, 1968) in his book on electric propulsion.

3.2.3 Dynamical model

To understand the dynamical model used for PPTs (equation (3-3)), we start by detailing Newton's second law in terms of the plasma sheet velocity as,

$$\frac{d}{dt} [m_T \dot{x}_s(t)] = \sum \mathbf{F}_L(t) \quad (3-18)$$

When the force acting on the system is that of a Lorentz force, then

$$\frac{d}{dt} [m_T \dot{x}_s(t)] = F_L(t) = \iiint_{\text{plasma sheet}} \mathbf{j} \times \mathbf{B} \cdot dV \quad (3-19)$$

Substituting equations (3-11) and (3-13) into equation (3-19) yields (Laperriere, 2005),

$$F_L(t) = \iiint_{\text{plasma sheet}} \mu_0 \frac{[I(t)]^2}{\delta w_e^2} \hat{\mathbf{x}} \left[1 - \frac{x - x_s(t)}{\delta} \right] dx dy dz = \mu_0 \frac{h_e [I(t)]^2}{w_e \delta} \hat{\mathbf{x}} \int_{x_s(t)}^{x_s(t)+\delta} \left[1 - \frac{x - x_s(t)}{\delta} \right] dx = \frac{1}{2} \mu_0 \frac{h_e}{w_e} [I(t)]^2 \hat{\mathbf{x}} \quad (3-20)$$

Therefore, substituting equation (3-20) into equation (3-18), the dynamic equation for the electromechanical model is represented as,

$$\frac{d}{dt} [m_T \dot{x}_s(t)] = \frac{1}{2} \mu_0 \frac{h_e}{w_e} [I(t)]^2 \hat{\mathbf{x}} \quad (3-21)$$

3.2.4 Plasma Resistance model

From equation (3-1) it can be seen that the electrical equation is dependent on the resistance of the system. Due to various factors influencing the system resistance, the total resistance is the summation of the resistance of each component. Thus,

$$R_T(t) = R_c + R_e + R_{pe} + R_p(t) \quad (3-22)$$

As plasma resistance ($R_p(t)$) play a fundamental role in the performance of the thruster, a plasma resistance model was formulated by Laperriere (2005) to represent a more realistic plasma resistance model instead of the constant resistance fitting the curve of the current discharge. As the plasma resistance influences the developed current, it inherently influences the plasma velocity, specific impulse and thrust (Nada, Semtember, 2013). Therefore, Laperriere (2005) proposed to use the Spitzer-Harm model while assuming the plasma is fully ionised and singly charged. This led to the plasma resistance being described as,

$$R_p(t) = \frac{l}{\sigma A} = \frac{h_e}{\sigma_p w_e \delta} \quad (3-23)$$

where σ_p , h_e , w_e and δ represents the plasma conductivity, the electrode separation distance, the electrode width, and the plasma sheet thickness, respectively. To determine the sheet thickness, the magnetic diffusion depth was used since the plasma sheet is governed by the diffusion equation² (Haus & Melcher, 1989).

$$\delta = \sqrt{\frac{\tau}{\sigma_p \mu_0}} \quad (3-24)$$

Since the ringing period³ represents the reciprocal of the pulse time, τ represents the characteristic pulse time equal to a quarter of the PPT ringing period (Nada, Semtember, 2013). In the equation above, the spitzer conductivity σ_p , used to determine the plasma conductivity, is given by,

$$\sigma_p = (1.53 \times 10^7) \frac{T_e^{\frac{3}{2}}}{\ln \Lambda} \quad (3-25)$$

where T_e and $\ln \Lambda$ represents the electron temperature and the Coulomb logarithm (often called the 'Spitzer algorithm') (Laperriere, 2005). The plasma parameter Λ of the Spitzer algorithm is found to be the ratio between the Debye length (λ_D) and the impact parameter (b_0) (Krommes, 2018) and is presented as,

$$\Lambda = \frac{\lambda_D}{b_0} \quad (3-26)$$

To elaborate on the plasma parameter, the Debye length is described as the distance over which electrons and ions can be separated within a plasma. The Debye length is mathematically described as,

$$\lambda_D = \left(\frac{\epsilon_0 k_B T_e}{e^2 n_e} \right)^{\frac{1}{2}} \quad (3-27)$$

² The diffusion equation refers to the behaviour of macro-particles in Brownian motion which results from random movements and particles colliding.

³ The circuit in Figure 3-2 represents a 2nd order system. Therefore, when the capacitor is allowed to discharge through the circuit, the current will be a decaying sinusoid, also sometimes referred to as 'ringing'.

where ε_0 , k_B , e and n_e represent, respectively, the permittivity of free space (dielectric constant), Boltzmann's constant, the electron charge and finally the electron density (Gibbon, 2014). Furthermore, the impact parameter, seen in Figure 3-7, represents the distance of the closest approach between two particles (Krommes, 2018) and is mathematically described as,

$$b_0 = \frac{q_1 q_2}{m_r v_r^2} \quad (3-28)$$

Where q_1 , q_2 , m_r and v_r are respectively, the charge on particles 1 and 2, the reduced mass, and the relative velocity.

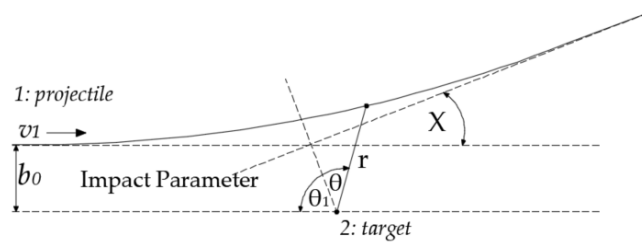


Figure 3-7 Impact Parameter collision orbit (Hutchinson, 2001-2021)

By substituting equation (3-27) and (3-28) into equation (3-26) and by the means of simplification, the ratio of the Debye length and the impact parameter is described as,

$$\Lambda = \frac{\lambda_D}{b_0} = (1.24 \times 10^7) \left(\frac{T_e^3}{n_e} \right)^{\frac{1}{2}} \quad (3-29)$$

Substituting equations (3-24), (3-25) and (3-29) back into equation (3-23), the final plasma resistance model is presented by

$$R_p = 8.08 \frac{h_e}{T_e^{\frac{3}{4}} w_e} \sqrt{\frac{\mu_0 \ln \left[1.24 \times 10^7 \left(\frac{T_e^3}{n_e} \right)^{\frac{1}{2}} \right]}{\tau}} \quad (3-30)$$

3.2.5 Mass Distribution Model

The fundamental principle of pulsed plasma thrusters dictates an acceleration of propellant/gas down a channel and information on how the mass is determined is essential to the modelling of the thruster. Hence, models such as the slug and snowplow (discussed in chapter 3.4) have been developed to estimate how much propellant is accelerated throughout the channel per unit time. (Michels, et al., 1966) improved on (Hart, 1962) snowplow model by introducing a variable mass loading distribution (Laperriere, 2005),

$$m_T(t) = m_0 + m_t \left[1 - \left[1 - \frac{x_s(t)}{l} \right]^{1-\alpha} \right] \quad (3-31)$$

Where m_0 , m_t , α and l represent, respectively, the initial mass accelerated, the additional mass added to the accelerated sheet as it transverses down the channel, the mass distribution loading parameter, and the channel length. As seen in Figure 3-8, the improved model led to the option of analysing the gas distribution as a constant throughout the channel ($\alpha = 0$, snowplow model) or as an initial ‘shot’ with no additional mass added to the sheet as it transverses down the channel ($\alpha = 1$, slug model).

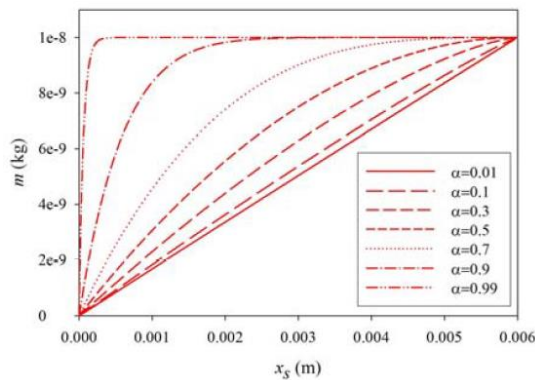


Figure 3-8 Mass distribution loading parameter

3.2.6 Summary of the General Electromechanical model

From the derivations observed in this chapter, the boundary conditions for the set of coupled non-linear second-order integro differential equations are defined as

$$x_s(0) = 0, \quad \dot{x}_s(0) = 0, \quad \int_0^{t=0} I(\tau) \cdot d\tau = 0, \quad I(0) = 0 \quad (3-32)$$

By substituting the mass distribution (3-31) and plasma resistance (3-30) models into both the electrical and dynamical equations, the one-dimensional electromechanical PPT for unsteady plasma acceleration is defined.

Below the various model equations are given:

Electrical circuit model

$$V_c(t) = V_0 - \frac{1}{C} \int_0^t I(\tau) \cdot d\tau = I(t)(R_c + R_e + R_{pe} + R_p) + \dot{I}(t) \left[L_c + L_e + \mu_0 \frac{h_e}{w_e} x_s(t) + \mu_0 \frac{\delta h_e}{2 w_e} \right] + I(t) \mu_0 \frac{h_e}{w_e} \dot{x}_s(t) \quad (3-33)$$

Dynamical model

$$\frac{d}{dt} [m_T \dot{x}_s(t)] = \frac{1}{2} \mu_0 \frac{h_e}{w_e} [I(t)]^2 = \frac{L'_{pe}}{2} [I(t)]^2 \quad (3-3)$$

Plasma resistance model

$$R_p = 8.08 \frac{h_e}{T_e^{\frac{3}{4}} w_e} \sqrt{\frac{\mu_0 \ln \left[1.24 \times 10^7 \left(\frac{T_e^3}{n_e} \right)^{\frac{1}{2}} \right]}{\tau}} \quad (3-30)$$

Mass Distribution Model

$$m_T(t) = m_0 + m_t \left[1 - \left[1 - \frac{x_s(t)}{l} \right]^{\frac{1}{1-\alpha}} \right] \quad (3-31)$$

3.3 Improved Electromechanical Models for a Parallel-Plate PPT

From the general electromechanical model, P.M. Waltz proposed a set of equations identical to Jahn's model (Jahn, 1968) with the exception of using the conservation of energy instead of KVL. This was accomplished by multiplying the circuit equation by $I = C\dot{V}$ and then differentiating with respect to time (Laperriere, 2005).

$$\frac{1}{2}(L_0 + L'_{pe}x_s)I^2 + \frac{1}{2}CV_c^2 + \int_0^t \frac{1}{2}L'_{pe}I \cdot d\tau + \int_0^t R_T I^2 d\tau = \frac{1}{2}CV_0^2 \quad (3-34)$$

When evaluating equation (3-34), the terms represent, respectively, the energy stored in the magnetic field, the capacitor energy, the kinetic energy supplied to the slug model, ohmic heating losses, and the total energy of the system. A year after Waltz and Vondra (1970) dared to improve the electromechanical model of the LES-6 thruster by leaving the electrical model unchanged and focusing on the dynamical model. Within his approach, he aimed to account for the gas-dynamic forces present in the acceleration of the propellant. To do this, he aimed to rather analyse the dynamic momentum equation in terms of Maxwell's stress tensor $\overline{\overline{T}}$, the particle stress tensor $\overline{\overline{P}}$, the particle momentum density \overline{p} , and the photon momentum density \overline{g} (Laperriere, 2005). The relation between the stress tensors and the momentum densities can be found in the momentum equation, represented as

$$\iiint \nabla \cdot (\overline{\overline{T}} + \overline{\overline{P}}) \cdot dV + \frac{\partial}{\partial t} \iiint (\overline{p} + \overline{g}) dV = 0 \quad (3-35)$$

From equation (3-35), the divergence of the stress tensor represents the particle electromagnetic force density, and the divergence of the particle stress tensor represents the gas-dynamic force density. To simplify this equation into common thruster parameters, assumptions combined with mathematical manipulation led to,

$$\int_0^t \left(\frac{1}{2}L'_{pe}I^2 + h_e w_e n k T \right) \cdot dt = m_0 \dot{x}_s \quad (3-36)$$

Where n , k , and T represent, respectively, the particle number density, Boltzmann's constant, and the plasma temperature. When differentiating equation (3-36) with respect to time, the new improved dynamical model is presented as

$$\frac{d}{dt}(m_0 \dot{x}_s) = \frac{1}{2}L'_{pe}I^2 + h_e w_e n k T \quad (3-37)$$

Comparing this model to the model designed by Jahn in equation (3-3), it is quite clear that the right-hand side of the equation consists of an additional force term. From equation (3-37), it

was found that the additional term represents the influence of the gas-dynamic forces acting on the acceleration of the thruster (Laperriere, 2005). Due to the simplicity and proven accuracy of the slug and snowplow models, it allows for a control strategy operation of the pulsed plasma thruster. Therefore, a one-dimensional model can be used since it approximates the PPT as an electromechanical model, divided into an electrical system and a mechanical system interacting with one another. By 2005 Laperriere (2005) set out to improve this electromechanical model by considering the external applied magnetic field effects. Due to the difficulty of applying a magnetic field to the enclosed geometry of a co-axial PPT, Laperriere rather focused on modifying the parallel-plate electromechanical model. To do this, he focussed on the effects of an additional external magnetic field (using permanent magnets) on the self-induced magnetic fields of the thruster.

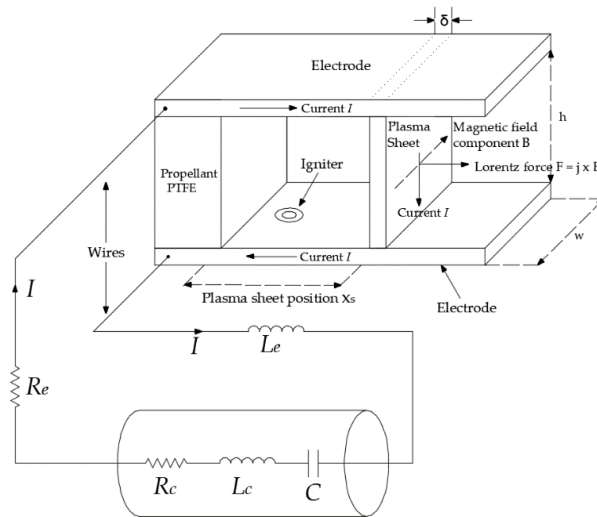


Figure 3-9 Electromechanical System

Revisiting the visual diagram of the parallel PPT (Figure 3-9), Laperrier’s improved electromechanical model resembles that of the general electromechanical model. Therefore, presenting Kirchoff’s law combined with Faraday’s law,

$$V_c(t) = IR_T(t) + \frac{d}{dt}[\lambda_{\text{PPT}}(t)] \quad (3-38)$$

where $R_T(t) = R_c + R_e + R_{pe} + R_p(t)$ and λ_{PPT} represents the total magnetic flux through the system. The total resistance of the system is due to that of the capacitor, lead and wire, electrodes, and plasma resistance. Defining the flux in terms of the components, yields

$$\lambda_{\text{PPT}}(t) = \lambda_c(t) + \lambda_e(t) + \lambda_{\text{pe}}(t) \quad (3-39)$$

where λ_c , λ_e and λ_{pe} represents the magnetic flux due to the capacitor inductance, the magnetic flux due to the leads and wires inductance and the magnetic flux due to the electrodes. When rewriting equation (3-39) in terms of capacitance and lead-and-wire self-inductance yields,

$$\lambda_{\text{PPT}}(t) = L_c I(t) + L_e I(t) + \iint_{\text{electrodes}} \mathbf{B}_{\text{ind}}(x, y) \cdot d\mathbf{A} \quad (3-40)$$

where L_c , L_e , \mathbf{B}_{ind} and $d\mathbf{A}$ represent the self-inductance of the capacitor, the lead-and-wire self-inductance, the self-induced magnetic field through the plasma sheet and an area vector. If the assumption is made that the external magnetic field is applied throughout the electrode channel and plasma sheet, equation (3-40) can be written as

$$\lambda_{\text{PPT}}(t) = L_c I(t) + L_e I(t) + \left[\mu_o \frac{h_e}{w_e} x_s(t) + \mu_o \frac{\delta h_e}{2 w_e} \right] I(t) + \int_0^{x_s(t)} \int_0^{h_e} \mathbf{B}_{\text{ext}}(t, x, y) \cdot dy dx + \int_{x_s(t)}^{x_s(t)+\delta} \int_0^{h_e} \mathbf{B}_{\text{ext}}(t, x, y) \cdot dy dx \quad (3-41)$$

Where $\mathbf{B}_{\text{ext}}(t, x, y)$ and δ represent the magnitude of the external magnetic field and the plasma sheet thickness. Rewriting equation (3-41) when assuming that the electrode channel has a negligible spatial gradient, yields

$$\lambda_{\text{PPT}}(t) = L_c I(t) + L_e I(t) + \left[\mu_o \frac{h_e}{w_e} x_s(t) + \mu_o \frac{\delta h_e}{2 w_e} \right] I(t) + h_e \mathbf{B}_{\text{ext}}(t) [x_s(t) + \delta] \quad (3-42)$$

When substituting equation (3-42) back into equation (3-38), Laperriere's modified circuit equation is shown as

$$V_c(t) = V_0 - \frac{1}{C} \int_0^t I(\tau) \cdot d\tau = I(t) (R_c + R_e + R_{\text{pe}} + R_p) + \dot{I}(t) \left[L_c + L_e + \mu_o \frac{h_e}{w_e} x_s(t) + \mu_o \frac{\delta h_e}{2 w_e} \right] + I(t) \mu_o \frac{h_e}{w_e} \dot{x}_s(t) + h_e \frac{d}{dt} \left\{ \mathbf{B}_{\text{ext}}(t) [x_s(t) + \delta] \right\} \quad (3-43)$$

When deriving the dynamical equation for Laperriere's improved electromechanical model, it can be noted that the only difference from the general electromechanical model is the addition of the external magnetic field throughout the plasma sheet. Thus,

$$\mathbf{B}_{\text{ind}}(t, x) = \begin{cases} \mu_o \frac{I(t)}{w_e} \hat{\mathbf{y}} + B_{\text{ext}}(t) \hat{\mathbf{y}}, & 0 < x < x_s(t) \\ \mu_o \frac{I(t)}{w_e} \left[1 - \frac{x - x_s(t)}{\delta} \right] \hat{\mathbf{y}} + B_{\text{ext}}(t) \hat{\mathbf{y}}, & x_s(t) < x < x_s(t) + \delta \\ B_{\text{ext}}(t) \hat{\mathbf{y}}, & x < x_s(t) + \delta \end{cases} \quad (3-44)$$

When a uniform current density is considered throughout the plasma sheet,

$$\mathbf{j}(t) = -\frac{I(t)}{w_e \delta} \hat{\mathbf{x}}_s \quad (3-45)$$

the Lorentz force acting on the sheet will be

$$\mathbf{F}_L(t) = \iiint_{\substack{\text{plasma} \\ \text{sheet}}} \mathbf{j}(t) \times \mathbf{B}(t, x) dV = \frac{I(t) h_e}{\delta} \hat{\mathbf{x}}_s \int_{x_s(t)}^{x_s(t) + \delta} \left\{ \mu_o \frac{I(t)}{w_e} \left[1 - \frac{x - x_s(t)}{\delta} \right] + B_{\text{ext}}(t) \right\} dx = \left\{ \frac{1}{2} \mu_o \frac{h_e}{w_e} [I(t)]^2 + h_e I(t) B_{\text{ext}}(t) \right\} \hat{\mathbf{x}}_s \quad (3-46)$$

Substituting equation (3-46) into Newton's second law of motion gives

$$\frac{d}{dt} [m_T \dot{\mathbf{x}}_s(t)] = \frac{1}{2} \mu_o \frac{h_e}{w_e} [I(t)]^2 + h_e I(t) B_{\text{ext}}(t) \quad (3-47)$$

As seen in equations (3-44) and (3-47), both equations are fairly similar to the general electromagnetic model, only to be distinguished by the additional terms representing the external magnetic field acting on the system.

3.4 General Slug and Snowplow Models

Due to the unique approach of different mathematical models, some models are more appropriate for certain PPT geometries than others. As the one-dimensional slug and snowplow models represent the simplest analytical model, it is frequently used on PPTs. Therefore, this section describes the working principle and mathematical representation of both these models.

3.4.1 Slug Model

Best described by Jahn (1968), the slug model represents a case in which the entire mass is accumulated at the point of breakdown. Thus, as the plasma transverses down the channel, no additional mass is accounted for during this acceleration process and is therefore constant. To visually represent the slug model process, Figure 3-10 is presented. For this reason, the slug model can be seen as an electromagnetic cannon, as it was historically designed to be. Since the ablated mass is considered constant throughout this process, the slug model is suitable for only specific cases (Jahn, 1968). Thus, slug models are generally used in the evaluation of breech-fed thrusters when gas-dynamic forces are neglected and, due to the perpendicular orientation between the propellant face and the accelerated mass.

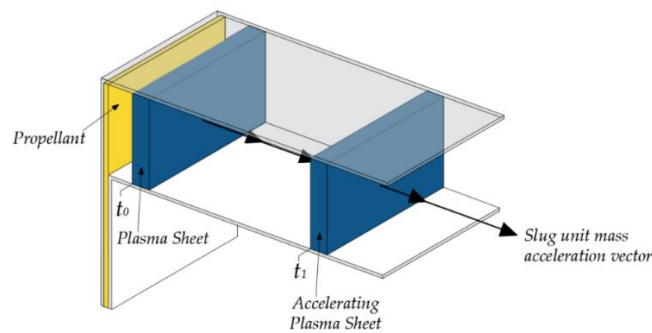


Figure 3-10 Representation of Slug model

From the general dynamical system equation seen in equation (3-3) and more so described in chapter 3.2.3, using the quasi-infinite parallel plate geometry, the dynamic system is represented as,

$$m_o \ddot{x}_s = h_e w_e \int_0^{\delta} IB dx = \frac{\mu_o h_e}{2w_e} I^2 = \frac{1}{2} L'_{pe} I^2 \quad (3-48)$$

3.4.2 Snowplow Model

The snowplow, a model which earned its name from its additive characteristics, is the most common model found in PPTs. One of the deficiencies of the slug model refers to its inadequacy to account for the additional ambient mass accelerating through the channel. Therefore, this model represents a case where a sweeping feature of the current zone, driven by its own magnetic field, acts as an impermeable absorbing surface accelerating down the channel,

essentially accumulating all mass overtaken by it. Figure 3-11, demonstrates the mass accumulation within a PPT discharge. Furthermore, it should be noted that the shade of blue in Figure 3-11 is directly related to the mass density of the accelerating sheet (darker = higher mass density) thus, it displays the accumulation of mass as it propagates through the channel.

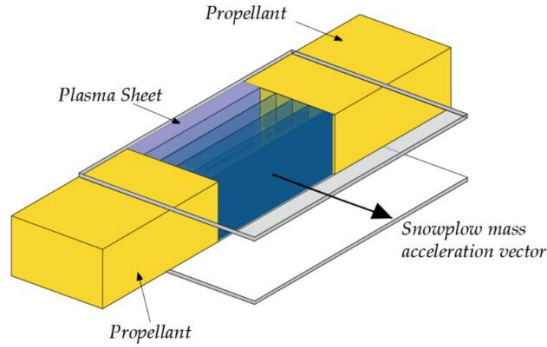


Figure 3-11 Representation of Snowplow model mass accumulation

Since the snowplow model uses a sweeping feature similar to the cannon gun effect in the slug model, the difference in the models can be seen as a dynamic one. For this reason, the circuit equation is unchanged from the slug model observed in equation (3-1). Although the dynamic equation for the slug and snowplow models are almost identical, the major difference is found in the additional inertial term added to Newton's law. This additional term is to account for the plasma sheet mass accumulation as it propagates down the channel and is described by,

$$m_T \ddot{x}_s + \dot{m}_T \dot{x}_s = \frac{1}{2} L'_{pe} I^2 \quad (3-49)$$

If it is considered that the plasma sheet initially contains a small but finite mass (m_0), the plasma sheet accumulates mass at a rate determined by the sheet velocity, the channel dimensions and the ambient mass density distribution when it is considered uniform (Jahn, 1968). This leads to the dynamical equation,

$$(m_0 + h_e w_e \rho x_s) \ddot{x}_s + h_e w_e \rho \dot{x}_s^2 = \frac{1}{2} L'_{pe} I^2 \quad (3-50)$$

Since,

$$m_T(x_s) = m_0 + h_e w_e \int_0^{t(x_s)} \rho(x_s) \dot{x}_s dt = m_0 + h_e w_e \rho x_s \quad (3-51)$$

where ρ represents the ambient mass density distribution. Further studies by (Nada, Semtember, 2013) were conducted on a modified snowplow model. According to his work, within the traditional snowplow model, authors neglected the influence of:

- The geometry
- The capacitor energy in determining the plasma resistance
- Assumed the ablation mass per pulse was constant.

As these factors have a significant influence on the performance of the thruster, some traditional models led to an error of up to 70%, while his tests resulted in a significant error improvement of only 8% (Nada, Semtember, 2013).

3.5 Summary and Conclusion

From the literature on pulsed plasma theory, the one-dimensional general electromechanical model is chosen for this thesis. This is due to the simplicity of the model while delivering fairly accurate performance estimations. From evaluating the slug and snowplow models, the conclusion is made that the slug model is more appropriate for breech-fed thrusters and the snowplow model is more appropriate for side-fed thrusters. Furthermore, due to the minimal increase in performance estimations compared to the high increase in complexity, gas-dynamic and multi-fluid models are neglected for this work.

Chapter 4

Numerical Model Simulation for a Parallel Plate PPT

4.1 Introduction

Following the general electromechanical model discussed in chapter 3.2, this chapter introduces a numerical technique to estimate the performance of the thruster. This chapter is divided into five sections, namely:

- Model simplification and assumptions
- Numerical implementation
- Software design and application guidelines
- Model validation
- A comparison of μ PPT parameters for preliminary design.

Starting this chapter, simplifications and assumptions are clarified to clearly define the electromechanical model for this work. To solve the electromechanical model, a numerical solution is presented. As multiple simulations are required to determine thruster parameters, a software application and guideline are presented. To ensure that the software application deems credible, model validations are presented with known pulsed plasma thrusters. Finally, a μ PPT parameters comparison is presented to understand the relationship between the thruster variables and their effect on thruster performance. Therefore, the initial voltage and capacitor ratio are examined, followed by an evaluation of the aspect ratio. From the results found within the evaluations, suggested preliminary design parameters are presented.

4.2 Model Simplification and Assumptions

Due to the complex physics involved in simulating real case unsteady electromagnetic accelerators, simplifications and assumptions are introduced for this work. The simplifications and assumptions allow for a good approximation of the real case scenario. For that reason, the following model simplifications and assumptions are specified:

- A one-dimensional model is used as it approximates the pulsed plasma thruster as an electromechanical system, which consists of an electrical system interacting with a dynamical system.
- The electric circuit is theoretically idealized as an RLC circuit with discrete, albeit movable elements.
- The system resistance remains constant throughout the acceleration process.
- The initial mass is constant throughout the whole process. Thus, no mass is accumulated along the channel path (Slug Model).
- The dynamical system is theoretically idealized by assuming that the initial mass is being accelerated by means of a Lorentz force.
- If the initial mass is considered constant, the inductance of the plasma sheet with respect to the position will remain constant, when assuming a constant magnetic field in the circuit.
- The only magnetic field consideration used in the model is the field generated by the PPT circuit. These fields are considered constant and perpendicular to the Lorentz force generated in the circuit. Thus, external magnetic fields are considered zero.
- The current density within the plasma layer is considered uniform and constant. Thus, any displacement current is neglected.

4.3 Revision of the General Electromechanical Model

In chapter 3 it was shown that by substituting the mass distribution and plasma resistance models into both the electrical and dynamical equations, a one-dimensional electromechanical model is defined for unsteady electromagnetic acceleration. Therefore, the general electromechanical model discussed in chapter 3 is re-presented below which is used within the numerical model.

Electrical Circuit Model

$$V_c(t) = V_0 - \frac{1}{C} \int_0^t I(\tau) \cdot d\tau = I(t)(R_c + R_e + R_{pe} + R_p) + \dot{I}(t) \left[L_c + L_e + \mu_0 \frac{h_e}{w_e} x_s(t) + \mu_0 \frac{\delta h_e}{2 w_e} \right] + I(t) \mu_0 \frac{h_e}{w_e} \dot{x}_s(t) \quad (3-33)$$

Dynamical Model

$$\frac{d}{dt} [m_T \dot{x}_s(t)] = \frac{1}{2} \mu_0 \frac{h_e}{w_e} [I(t)]^2 = \frac{L'_{pe}}{2} [I(t)]^2 \quad (3-3)$$

Plasma Resistance Model

$$R_p = 8.08 \frac{h_e}{T_e^{\frac{3}{4}} w_e} \sqrt{\frac{\mu_0 \ln \left[1.24 \times 10^7 \left(\frac{T_e^3}{n_e} \right)^{\frac{1}{2}} \right]}{\tau}} \quad (3-30)$$

Mass Distribution Model

$$m_T(t) = m_0 + m_t \left[1 - \left[1 - \frac{x_s(t)}{l} \right]^{1-\alpha} \right] \quad (3-31)$$

Initial Conditions

$$x_s(0) = 0, \quad \dot{x}_s(0) = 0, \quad \int_0^{t=0} I(\tau) \cdot d\tau = 0, \quad I(0) = 0 \quad (3-32)$$

4.4 Numerical Implementation of the General Electromechanical Model

In this section, the transformation of the electromechanical model adhering to the software and mathematical requirements is discussed. To do this, a numerical solution is presented on how to solve the electrical and dynamical equations within the electromechanical model. The electromechanical model for a parallel plate PPT is a set of coupled non-linear second-order

integro-differential equations. Thus, conventional analytical solutions will be math-intensive and tedious to solve. As both the discharge current ($I(t)$) and the plasma sheet position (x_s) are unknown in the electrical and dynamical equations, the Euler method and the Runge-Kutta method were investigated to solve these equations numerically. Thus, for this project, MATLAB® was the preferred choice of simulation software within which the built-in ODE45 solver was used. To further elaborate on the built-in ODE45 solver, it should be noted that the solver uses the Runge-Kutta 4th order solver for ODE solutions.

To solve this non-linear problem, the two non-linear second-order ODEs are written as a set of four first-order differential equations. This is done by converting the system of equations into state space. When introducing the state-space variables into the equations found in the prior chapter 4.3, we define

$$x_1(t) = \int_0^t I(\tau) \cdot d\tau \quad (4-1)$$

$$x_2(t) = I(t) \quad (4-2)$$

$$x_3(t) = x_s(t) \quad (4-3)$$

$$x_4(t) = \dot{x}_s(t) \quad (4-4)$$

Remembering that,

$$I(t) = C \frac{dV_c}{dt} \quad (4-5)$$

and through manipulation, we get

$$\frac{dV_c}{dt} = \frac{1}{C} I(t) \quad (4-6)$$

Thus, inserting the state variables into the system of equations, equations (3-3), (4-6) and (3-33), the state space form of the parallel plate slug model becomes,

$$\dot{x}_1(t) = \frac{1}{C} x_2(t) \quad (4-7)$$

$$\dot{x}_2(t) = \frac{-R_T x_2(t) - x_1(t) - x_2(t) L'_{pe} x_4(t) + V_0}{(L_T)} \quad (4-8)$$

$$= \frac{-R_T x_2(t) - x_1(t) - x_2(t) \mu_0 \frac{h_e}{w_e} x_4(t) + V_0}{(L_T)}$$

$$\dot{x}_3(t) = x_4(t) \quad (4-9)$$

$$\dot{x}_4(t) = \frac{L'_{pe}}{2m_T} (x_2(t))^2 \quad (4-10)$$

Where $R_T = R_c + R_e + R_{pe} + R_p$, $L_T = L_c + L_e + L_{pe} + L_p$ and considering the slug model is used, $m_T = m_0$. From Laperriere (2005) it has been shown that the energy equation can be derived from equation (3-33) by multiplying with the current ($I(t)$) and integrating over time.

$$\int_0^t I(t) V_c dt = \int_0^t \frac{d}{dt} \left\{ \frac{1}{2} [I(t)]^2 L_T(t) \right\} dt + \int_0^t R_T(t) [I(t)]^2 dt + \int_0^t \frac{1}{2} [I(t)]^2 L'_{pe} \dot{x}_s(t) dt \quad (4-11)$$

Substituting equation (4-5) into equation (4-11), the energy equation described by Laperriere (2005) is shown as

$$\frac{1}{2} C V_0^2 - \frac{1}{2} C [V_c(t)]^2 = \frac{1}{2} [I(t)]^2 L_T(t) + \int_0^t R_T(\tau) [I(\tau)]^2 dt + \int_0^t \frac{1}{2} \frac{h_e}{w_e} \mu_0 [I(\tau)]^2 \dot{x}_s(\tau) dt \quad (4-12)$$

From the energy equation, the capacitor energy, energy loss through ohmic heating, energy stored in the magnetic field and energy given to the plasma sheet, are presented. Therefore, the capacitor energy throughout time is given by

$$E_c(t) = \frac{1}{2} C V_c^2 = \frac{1}{2} C x_1(t)^2 \quad (4-13)$$

The energy dissipation to ohmic heating is given by

$$E_\Omega(t) = \int_0^t R_T(\tau) [I(\tau)]^2 d\tau = \int_0^t R_T(\tau) [x_2(\tau)]^2 d\tau \quad (4-14)$$

The energy stored in the magnetic field is given by

$$E_B(t) = \frac{1}{2} \left[L_c + L_e + \mu_0 \frac{h_e}{w_e} x_s(t) \right] [I(t)]^2 = \frac{1}{2} \left[L_c + L_e + \mu_0 \frac{h_e}{w_e} x_3(t) \right] [x_2(t)]^2 \quad (4-15)$$

And the energy used to accelerate the plasma sheet is given by

$$E_{KE}(t) = \frac{1}{2} m_0 V_c^2 = \frac{1}{2} m_0 x_1(t)^2 \quad (4-16)$$

4.5 Software to Implement the Numerical Model

Generally, model simulations consist of repetition, especially when performance estimates are required. For this reason, a software application (consisting of written code and a GUI) was created and is shown in Figure 4-1, to simplify the numerical testing framework and decrease simulation set-up time.

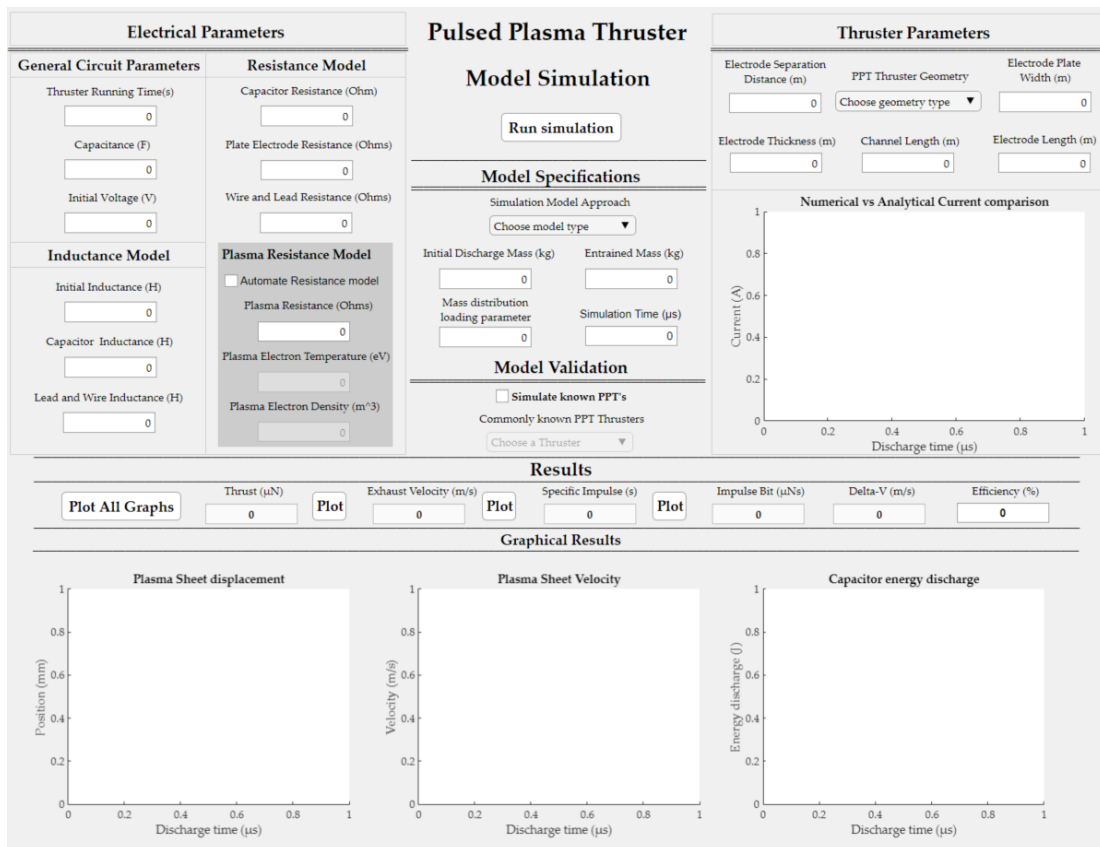


Figure 4-1 MATLAB® One Dimensional model GUI overview

Due to the complex physics governing the electromagnetic pulsed plasma thruster, software plays a significant role in not only eliminating calculation-time, but also when conducting multiple tests successively and manipulating input data variables. Initially, a MATLAB® program was written to determine the performance of the thruster when inserting the system parameters directly into the code. Although this seemed very effective at first, it was not user-

friendly. After creating an additional GUI interface and combining it with the program, also called an ‘*Application*’, simplicity and clarity were ensured to any user. As shown in Figure 4-1, the application mainframe is discretized into sections/pockets around which the system is formed. These sections are composed of namely: ‘*Electrical Parameters*’, ‘*Thruster Parameters*’, ‘*Model Specifications*’, and an additional ‘*Model Validation*’ section.

Electrical Parameters

The ‘*Electrical Parameters*’ section is divided into four sections, namely: ‘*General Circuit Parameters*’, ‘*Inductance Model*’, ‘*Resistance Model*’ with the sub-section, ‘*Plasma Resistance Model*’. As the initial voltage and capacitance are not defined by other system parameters, they form part of the general layout of the electrical model.

Electrical Parameters	
General Circuit Parameters	Resistance Model
Thruster Running Time(s) <input type="text" value="0"/>	Capacitor Resistance (Ohm) <input type="text" value="0"/>
Capacitance (F) <input type="text" value="0"/>	Plate Electrode Resistance (Ohms) <input type="text" value="0"/>
Initial Voltage (V) <input type="text" value="0"/>	Wire and Lead Resistance (Ohms) <input type="text" value="0"/>
Inductance Model	Plasma Resistance Model
Initial Inductance (H) <input type="text" value="0"/>	<input type="checkbox"/> Automate Resistance model
Capacitor Inductance (H) <input type="text" value="0"/>	Plasma Resistance (Ohms) <input type="text" value="0"/>
Lead and Wire Inductance (H) <input type="text" value="0"/>	Plasma Electron Temperature (eV) <input type="text" value="0"/>
	Plasma Electron Density (m ⁻³) <input type="text" value="0"/>

Figure 4-2 Electrical input parameters

On the other hand, as shown in equations (4-1) and (4-2), the resistance and inductance models have multiple factors influencing their final value. In chapter 3.2, it is stated that the total resistance is a summation of all resistances within the system, therefore

$$R_T(t) = R_c + R_e + R_{pe} + R_p(t) \quad (4-1)$$

where $R_T(t)$, R_c , R_e , R_{pe} and $R_p(t)$ represent the total resistance in the system, the capacitor resistance, the electrode resistance, the lead and wire resistance, and the plasma resistance. Similarly, this characteristic is also seen within the inductance model as

$$L_T = L_c + L_e + L_{pe} \quad (4-2)$$

where L_T , L_c , L_e and L_{pe} represent the total inductance in the system, the capacitor inductance, the inductance due to the electrode, and the inductance due to the leads and wires. To insert a desired or estimated plasma resistance for initial testing, a general plasma resistance input is created in Figure 4-3(a). Activating the plasma resistance model in Figure 4-3(b) becomes useful once physical data on the plasma discharge is collected. Therefore, the plasma resistance model described in equation (3-30) is adopted to improve the accuracy of the simulation.

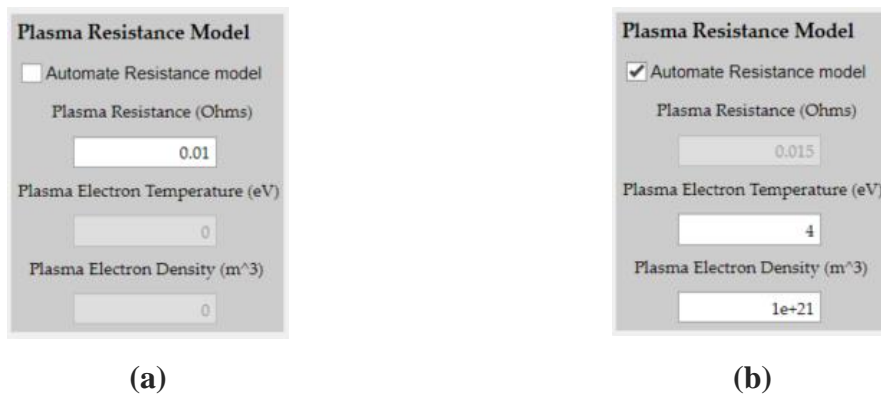


Figure 4-3 Plasma Resistance input parameters

Thruster Parameters

From Figure 4-4, the thruster parameters define the geometry of the thruster. This includes the electrode separation distance, electrode width, electrode thickness, channel length, electrode length and the geometry type of the thruster.

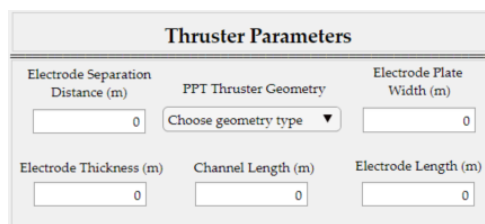


Figure 4-4 Thruster input parameters

As observed in Figure 4-5, the geometry selection includes the rectangular and coaxial formations. Although visible, it is important to note that the co-axial configuration strictly represents future work and therefore, the application is only limited to the rectangular configuration.

Figure 4-5 Thruster geometry selection

Model Specifications

Within the model specification section, simulation conditions are defined. This includes the simulation time, the initial discharge mass, entrained mass (Snowplow Model), mass distribution loading parameter and simulation model approach.

Figure 4-6 Model Specification input parameter

From Figure 4-7, it is seen that the ‘*Simulation Model Approach*’ can switch between the slug and snowplow model approach, described in chapter 3.4. Similar to Figure 4-5, the snowplow model represents future work and therefore, the application is only limited to the slug model.

Figure 4-7 Simulation modelling approach

Model Validation

As mentioned at the beginning of this chapter, the credibility of the simulation lies in whether the software is trustworthy or not. Therefore, the model validation section in Figure 4-8 was

added to the application to effectively determine the performance of two known thrusters. Since the parameters of each thruster are embedded into the software, redundancy is eliminated with the added advantage of easily comparing results to other models.

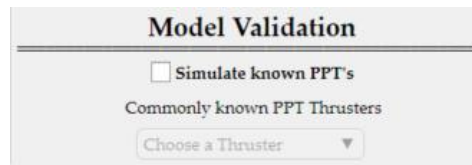


Figure 4-8 Model validation checkbox

As shown in Figure 4-9, the LES-6 and LES 8/9 thrusters (Burton & Turchi, 1998) were used for model validation. The LES-6 and LES 8/9 thrusters were chosen due to the popularity and wide range of information available. Simulation results of these thrusters can be found in chapter 4.6.

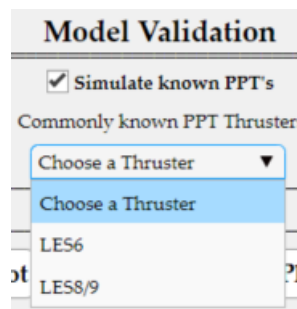


Figure 4-9 Simulation model dropdown list

Results

To run the simulation, the application GUI has a '*Run simulation*' button in the top centre of the interface. Once the program has completed its simulation, the results tab will be populated with the appropriate information as presented below in Figure 4-10.

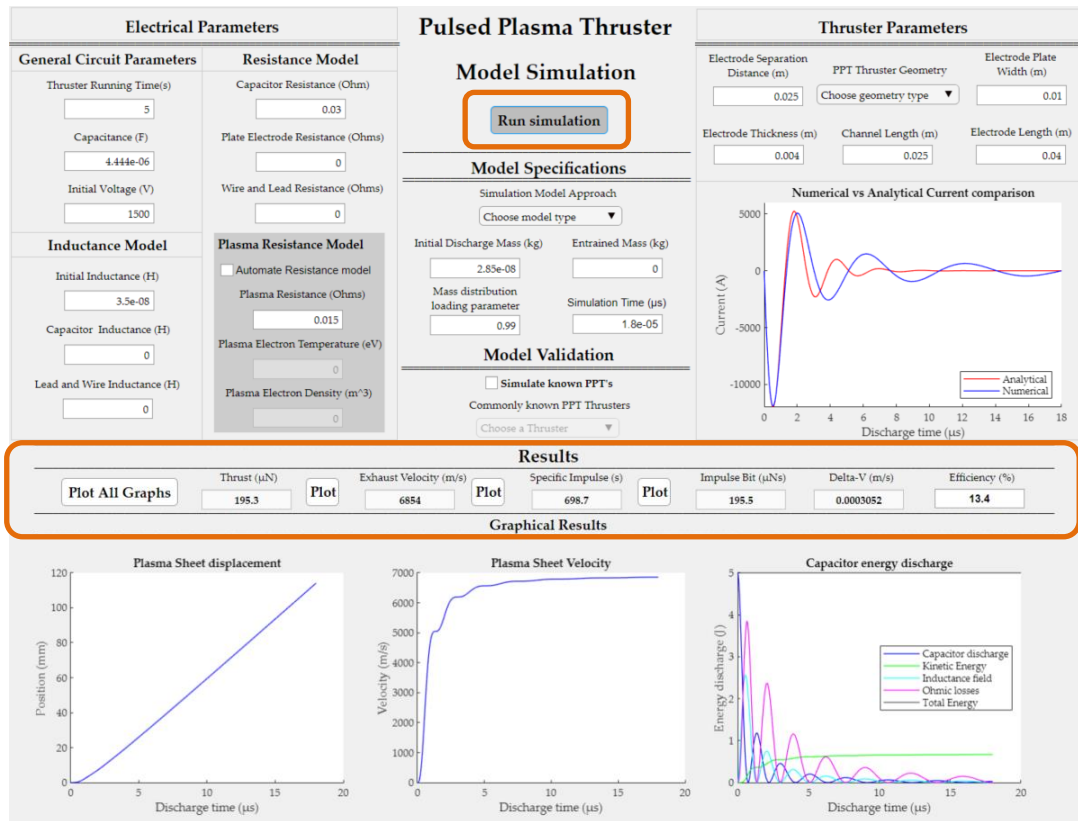


Figure 4-10 Simulation results of the general electromechanical model

4.6 Model Validation

For model validation, the results of the software model are compared to experimental data of two well-known thrusters. These thrusters are the LES-6 thruster and the LES-8/9 thruster. Therefore, from Table 4-1, two diverse data sets of these thrusters are represented.

Table 4-1 Experimental data control thrusters

Parameters	LES-6	LES-8/9
Initial Voltage (V)	1360	1538
Capacitance (μF)	2	17
Capacitor resistance ($\text{m}\Omega$)	30	30
Initial inductance (nH)	34	35
Electrode separation distance (cm)	3	2.45
Plate Width (cm)	1	2.54
Channel Length (cm)	0.6	2.54
Mass Bit (μg)	10	28.5
Pulse Time (μs)	0.4	1.0
Plasma Temperature (eV)	1.5	5
Electron Density (m^{-3})	1e21	1e21

As this thruster is intended for satellite propulsion, certain orbital mechanics parameters are considered to be crucial for the success of this device. These parameters include the exhaust velocity, specific impulse, and impulse-bit as they are required to determine the thrust and delta-v of a space vessel. For this reason, these parameters are the primary means by which the simulation software is compared and validated. To measure the accuracy of each comparison, two aspects will be taken into consideration, namely:

1. The similarities in the simulation data graph curves and experimental data graph curves.
2. The similarity between the simulation results and experimental results for:
 - Exhaust velocity
 - Thrust
 - Specific impulse
 - Efficiency

4.6.1 LES-6 model comparison

For the first data set comparison, the model was compared to the performance characteristics measured on the LES-6 thruster. Figure 4-11 shows graphs of capacitor voltage, discharge energy, exhaust velocity and propellant displacement as a function of time from our simulation together with experimental measurements of the LES-6 thruster (Burton & Turchi, 1998). From these graphs we see a number of similarities as follows:

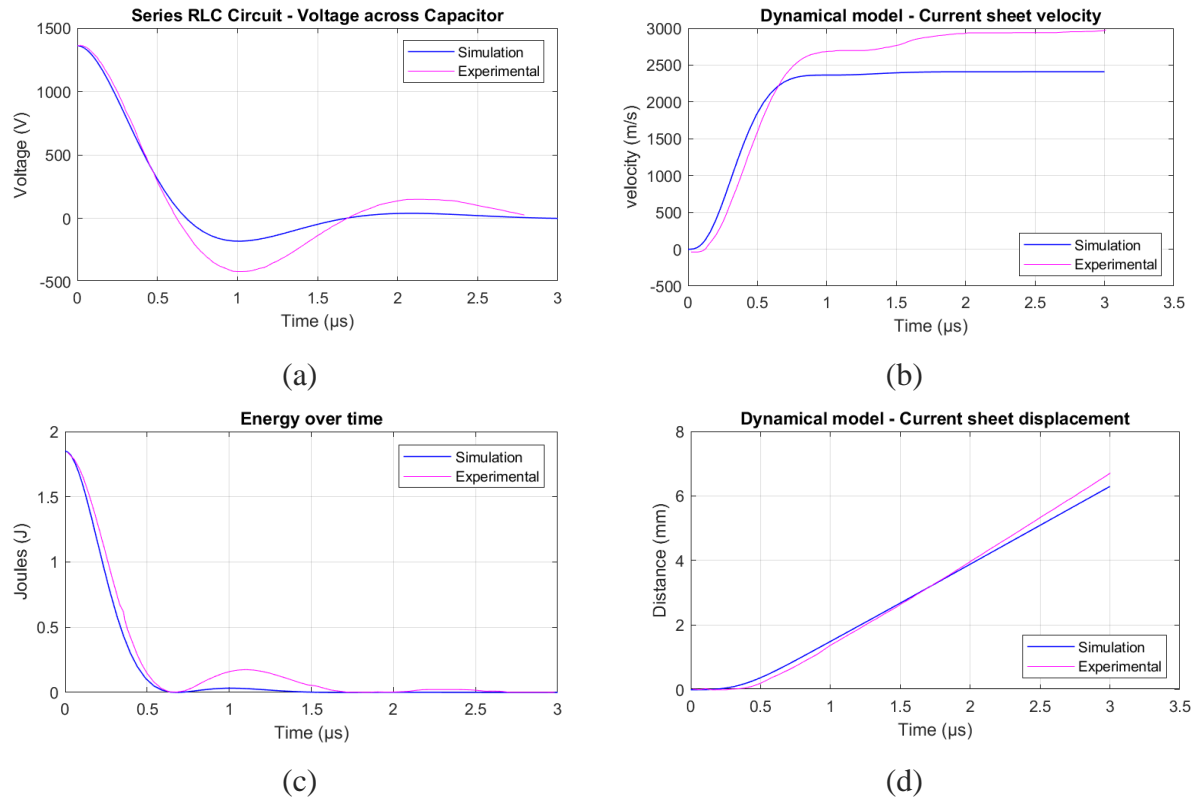


Figure 4-11 LES-6 experimental data and numerical model simulation comparison

As shown in Figure 4-11, the simulation results fit the curves of the experimental data well, although a clear underprediction in simulation performance is observed in Table 4-2. Comparing the simulation results with the work of Laperriere (2005), similarities arose with his findings. The first similarity between the simulation results and Laperriere’s (2005) results is that the simulation voltage waveform does not correspond with the voltage waveform found in the experimental data. This deviation might be due to the unaccounted resistance and inductance within the discharge capacitor.

Table 4-2 Comparison of simulation results and experimental data from Burton & Turchi (1998) for the LES 6 thruster.

Parameters	Experimental	Simulation	Similarity
Exhaust Velocity (m/s)	3000	2411	80.37%
Thrust (μN)	26	24.11	92.73%
I_{SP} (s)	300	245.7	81.9%
η (%)	2.2	1.571	71.41%

The underprediction of the simulation model agrees with (Laperriere, 2005) in stating that it is most likely caused by the combination of the negligence of the gas-dynamic forces acting on the system and the complexity of determining the plasma resistance throughout the discharging process. Considering these factors while appropriate scaling factors are still under investigation for the determination of thruster performance; we acknowledge that differences are to be expected.

4.6.2 LES-8/9 model comparison

For the second model comparison, the model was compared with the experimental data of the LES-8/9 thruster (Burton & Turchi, 1998). The comparison was made using the same ideology previously used with the LES-6 performance characteristics comparison.

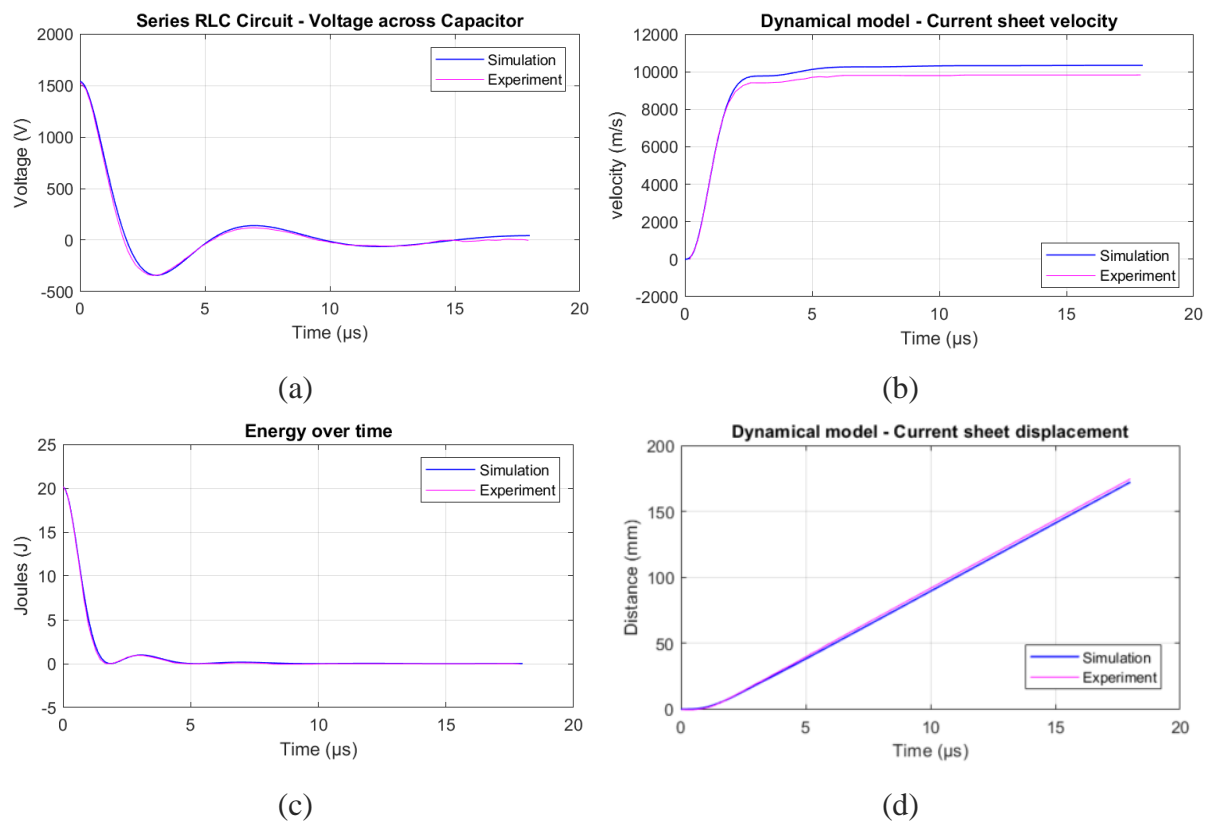


Figure 4-12 LES-8/9 experimental data and numerical model simulation comparison

Similar to the LES-6 comparison, Figure 4-12 shows graphs of capacitor voltage, discharge energy, exhaust velocity and propellant displacement as a function of time from our simulation together with experimental measurements of the LES-8/9 thruster (Burton & Turchi, 1998). When analysing the simulated voltage waveform with the experimental data, dissimilarities are

minimal. This could be due to the correct estimation of internal resistance and inductance within the capacitor.

Table 4-3 Comparison of simulation results and experimental data from Burton & Turchi (1998) for the LES 8/9 thruster.

Parameters	Experimental	Simulation	Similarity
Exhaust Velocity (m/s)	9810	10034	97.77%
Thrust (μ N)	297	294.7	99.26%
I_{SP} (s)	1000	1054	94.88%
η (%)	Just above 7	7.58	\pm 94.0%

Furthermore, unlike the LES-6 results shown in Figure 4-11, performance underprediction does not seem to be visible in the LES-8/9 comparison. Evaluating the results, the assumption is made that the plasma resistance determined by this model was very accurate and that gas-dynamic forces were minimal. From Table 4-3, it can be seen that the simulation model predicted the thruster results with a high level of accuracy.

4.7 μ PPT Parameters Comparison for Preliminary Design

Within this thesis, the design of the software application mainly steered towards approximating system performance by using input parameters of the thruster. Therefore, the following section describes the modelling conducted to approximate the appropriate system parameters for the preliminary design. Simulating a thruster's performance using various system parameters, essentially creates an opportunity to evaluate and compare each simulation with one another. The comparison allows for easier determination of the best theoretical system design. Therefore, this section discusses two combinatorial parameters essential to the performance of the thruster, namely:

- Initial voltage to capacitance ratio
- Aspect ratio

For the combinatorial parameters mentioned, all designs will be based on the combination of these parameters. Therefore, the results of the simulations will determine the required system parameters for the preliminary design.

4.7.1 Evaluation of the Initial Voltage to Capacitance Ratio

The first combinatorial parameter is the relationship between the initial voltage and capacitance of the PPT circuit under the same discharge energy. To understand the importance of this relationship, the discharge power is analysed as it is one of the influential parameters in PPT performance. The discharge power is directly related to the discharge energy and operating frequency of the PPT, therefore,

$$P = f \cdot E_0 \quad (4-3)$$

where P , f and E_0 represent the discharge power, the operating frequency, and the discharge energy, respectively. As the discharge energy is related to the capacitance and initial voltage of the system, the energy stored in a capacitor is given by (Rezaeiha & Schonherr, 2012),

$$E_0 = \frac{1}{2} CV_0^2 \quad (4-4)$$

where C and V_0 represents the capacitance and the initial voltage of the system. Multiple simulation tests were conducted within the simulation model to determine which relationship displayed the best results when varying the capacitance and initial voltage for a 5 W system operating at a frequency of 1 Hz (a single impulse-bit). A frequency of 1 Hz was used to determine the characteristics of a single discharge. The simulation tests conducted are presented in Table 4-4. As the electrical parameters were evaluated first, the mechanical system was kept constant by setting the electrode separation distance and electrode width equal to 10 mm and 10 mm, respectively.

Table 4-4 Simulation tests of initial voltage to capacitance ratio for a 5 W system

5 W μPPT		
Test	Initial Voltage (V_0)	Capacitance (C)
1	1500 V	4.44e-06 F
2	1400 V	5.10e-06 F
3	1300 V	5.92e-06 F
4	1200 V	6.94e-06 F
5	1100 V	8.26e-06 F
6	1000 V	1.0e-05 F
7	900 V	1.23e-05 F
8	800 V	1.56e-05 F
9	750 V	1.78e-05 F

Theoretical and practical tests conducted by Nawaz et al (2010) found that an increase in capacitance led to an increase in performance. This is due to the increase in energy density found in the discharge arc. Therefore, a high voltage/low capacitance test was first conducted, after which each test incremented the capacitance and lowered the voltage. Results of these simulations are compared in efficiency, exhaust velocity, specific impulse, and delta-v as shown in Figure 4-13 to Figure 4-16.

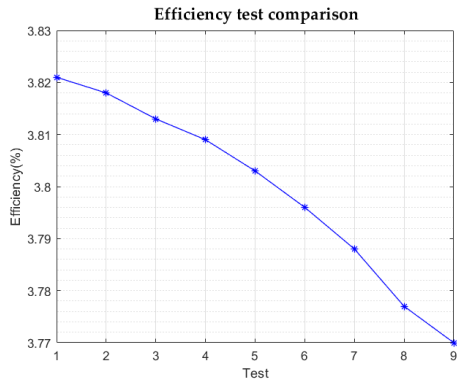


Figure 4-13 Efficiency-electrical test comparison

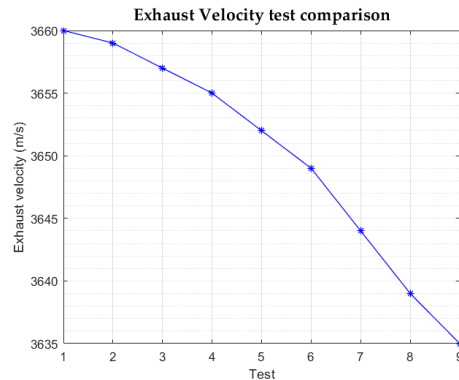


Figure 4-14 Exhaust velocity-electrical test comparison

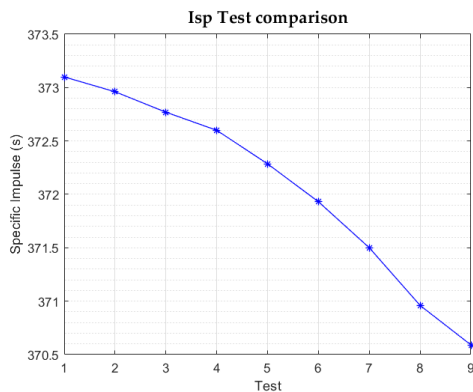


Figure 4-15 Specific impulse-electrical test comparison

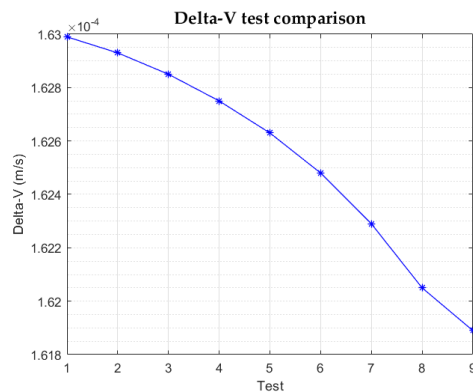


Figure 4-16 Delta-v- Electrical test comparison

From Figure 4-13 to Figure 4-16, the graphs show that the performance drops when the initial voltage drops. Although studies by Nawaz et al. (2010) stated that an increase in capacitance leads to an increase in performance, simulations conducted for this project show that this statement is only true when the system power increases in relation to the capacitance ($\uparrow P = \uparrow C$). Therefore, as the initial voltage decreases and the capacitance increases, while keeping a constant system power, a degradation in performance is observed. Throughout the simulation tests in Table 4-4, a non-linear relationship is observed between the capacitor and discharge current. This non-linearity can be observed in Figure 4-17 and Figure 4-18 where a numerical

approach (chapter 4.4) and analytical approach (equation (4-6)) were used to calculate the discharge current from a set capacitor value.

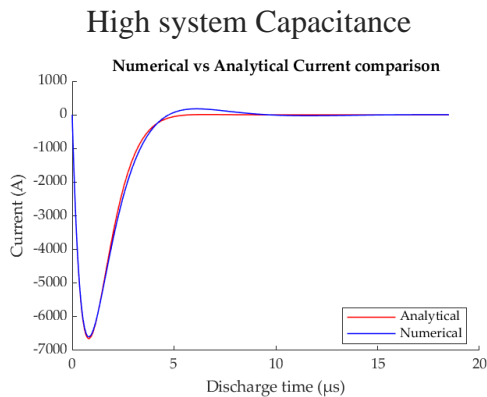


Figure 4-17 High capacitance discharge

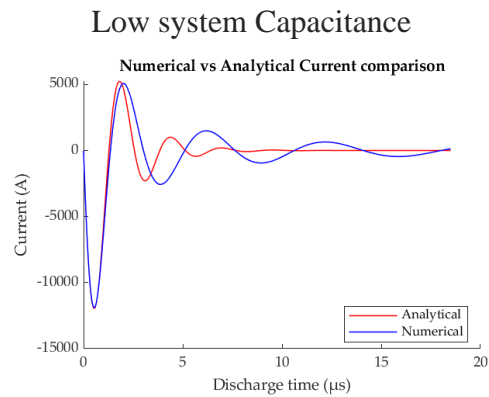


Figure 4-18 Low capacitance discharge

This non-linearity can best be described by analysing Figure 4-17 and Figure 4-18 and observing the difference in the capacitance ratio to discharge current ratio in Table 4-5. The capacitance ratio is calculated by dividing the ‘high systems capacitance’ by the ‘low system capacitance’. The current ratio is determined by dividing the current discharge result of the ‘high system capacitance’ by the current discharge result of the ‘low system capacitance’. Comparing the highest and lowest system capacitance from Table 4-4 to the current discharge, a non-linear relationship is observed in that a capacitor four times smaller does not generate a current discharge four times bigger.

Table 4-5 Capacitance to peak discharge current comparison when varying the capacitance value and analysing the discharge current in Figure 4-17 and Figure 4-18.

	Capacitance (F)	Peak Current (A)
Highest system capacitance	1.78e-05	6650
Lowest system capacitance	4.444e-06	11900
Ratio (Highest/Lowest)	4	1.789

Furthermore, increasing the capacitance of the system leads to a reduction in system oscillations. Also, comparing all of the ‘initial voltage to capacitor’ simulations from Table 4-4, an increase in capacitance yielded a longer discharge period as first mentioned by Nawaz et al. (2010). Thus, one could speculate the capacitor acts as a damper to the system.

4.7.2 Evaluation of the Aspect Ratio

The second combinatorial parameter is the aspect ratio (ratio between the electrode separation distance h_e and the electrode width w_e). According to fellow researchers, it was found that an increase in aspect ratio will increase the performance of the thruster. This is due to the proportionality factor between the aspect ratio, thrust and power (Pottinger & Scharlemann, 2007).

$$\frac{T_F}{P} \propto \frac{h_e}{w_e} \quad (4-5)$$

Although equation (4-5) describes the relationship between the aspect ratio, thrust and power, it should be noted that it does not hold for all cases. As described by (Burton & Turchi, 1998), it was found that the aspect ratio of a breech-fed μ PPT should ideally range between 0.69 and 3.8 as it was observed that theoretical simulations and practical results match best in this region. Analysing the energy dissipated per cm^2 ($h_e \times w_e$), found to be an effective method to determine the aspect ratio. Therefore, similar to the initial voltage to capacitance simulations, the relationship between the electrode separation distance and the electrode width was simulated and is presented in Table 4-6. This was done by varying the aspect ratio between 0.4 and 2.5 while keeping a constant surface area of 250 mm^2 .

Table 4-6 Aspect ratio simulation tests

Surface area = 250 mm^2		
Test	Height (h_e)	Width (w_e)
1	10 mm	25 mm
2	12.5 mm	20 mm
3	15.8 mm	15.8 mm
4	20 mm	12.5 mm
5	25 mm	10 mm

Similar to the ‘initial voltage to capacitance’ ratio, the results of these simulations are compared in efficiency, exhaust velocity, specific impulse, and delta-v as shown in Figure 4-19 to Figure 4-22 below.

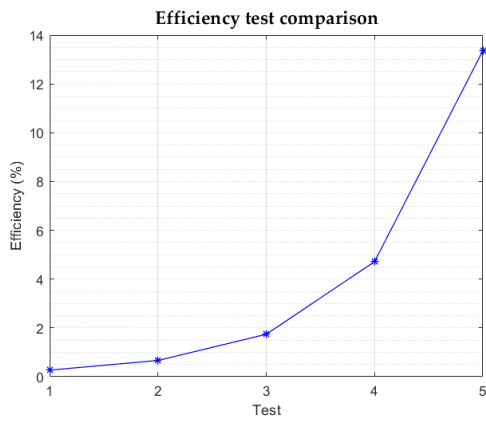


Figure 4-19 Efficiency-Dynamical test comparison

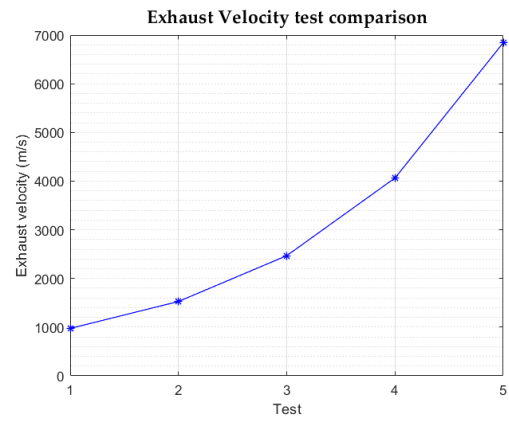


Figure 4-20 Exhaust velocity- Dynamical test comparison

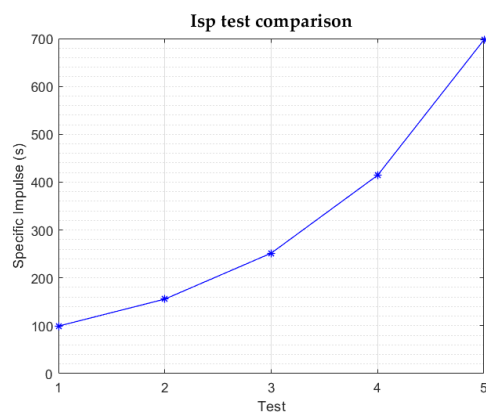


Figure 4-21 Specific Impulse- Dynamical test comparison

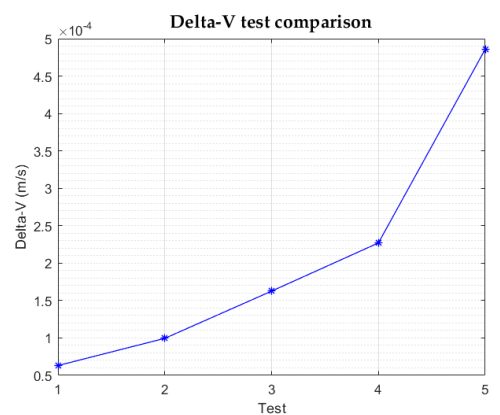


Figure 4-22 Delta-V- Dynamical test comparison

Comparing Table 4-6 with Figure 4-19 to Figure 4-22, a rate of increase is observed and therefore the aspect ratio does indeed show an increase in theoretical performance of the thruster as described by (Pottinger & Scharlemann, 2007). Observing Figure 4-20 and Figure 4-21 demonstrates the known correlation between the exhaust velocity and the specific impulse as shown in equation (1-3), while Figure 4-19 and Figure 4-22 show some similarities in their shapes. To illustrate the dangers of exceeding the boundary limits of the aspect ratio, an example is presented with the aspect ratio $\gg 3.8$, in Figure 4-23.

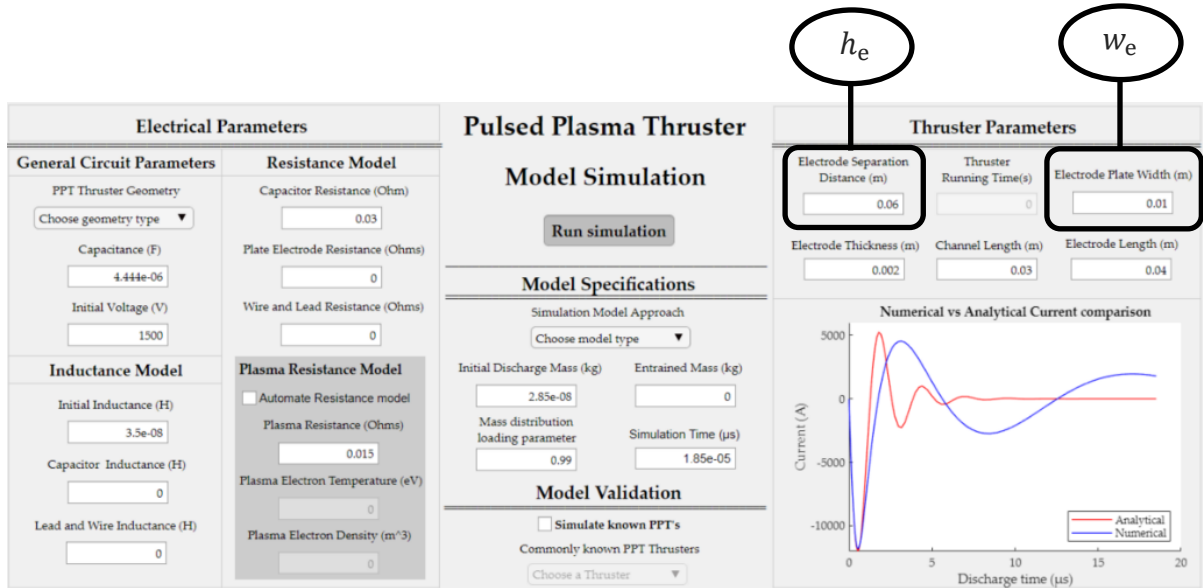


Figure 4-23 Exceeded aspect ratio boundary example

From Figure 4-23, it can firstly be seen that the numerical model's discharge current curve deviates from the analytical model discharge current curve. This change in characteristic is due to the inductance gradient variable, shown in equation (3-33), being present in the electrical equation of the electromechanical model.

$$V_c(t) = V_0 - \frac{1}{C} \int_0^t I(\tau) \cdot d\tau = I(t) (R_c + R_e + R_{pe} + R_p) + \dot{I}(t) \left[L_c + L_e + \mu_0 \frac{h_e}{w_e} x_s(t) + \mu_0 \frac{\delta h_e}{2 w_e} \right] + I(t) \mu_0 \frac{h_e}{w_e} \dot{x}_s(t) \quad (3-33)$$

The analytical model (Wallangen, 2014), presented in equation (4-6), relies on electrical parameters only to determine the current discharge, whereas the electromechanical model includes the thruster geometry. Therefore, a difference in results is expected.

$$I = \frac{V_0}{L_0} \frac{1}{\sqrt{\frac{1}{L_0 C} - \frac{R^2}{4L_0^2}}} \exp\left(-\frac{R}{2L_0} t\right) \sin\left\{\left(\sqrt{\frac{1}{L_0 C} - \frac{R^2}{4L_0^2}}\right) t\right\} \quad (4-6)$$

Figure 4-24 further illustrates the instability of the model when exceeding the aspect ratio limit of 3.8. From this, it can be seen that the results are unrealistic and unreliable. Therefore, for a stable system, the aspect ratio needs to be limited.

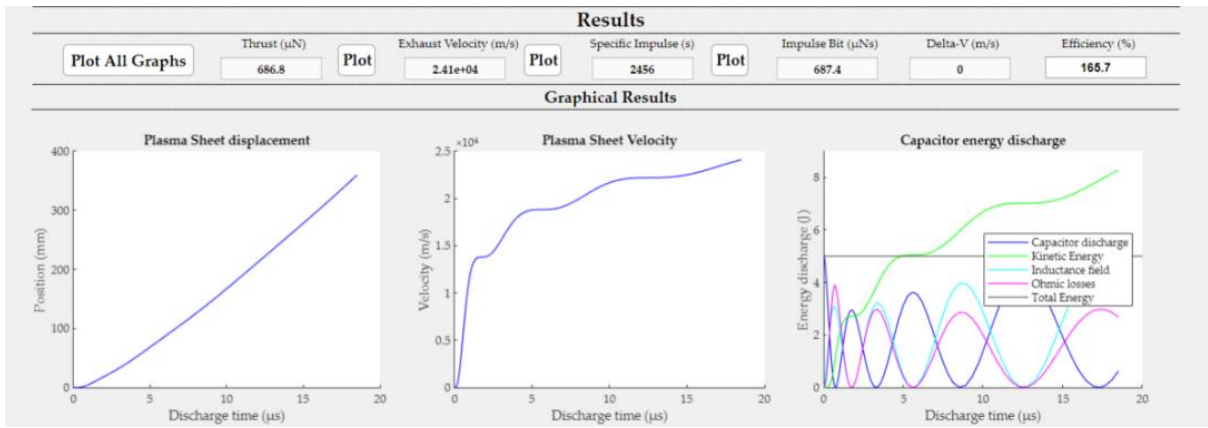


Figure 4-24 Aspect ratio boundary example results

4.7.3 Suggested Preliminary Design Parameters

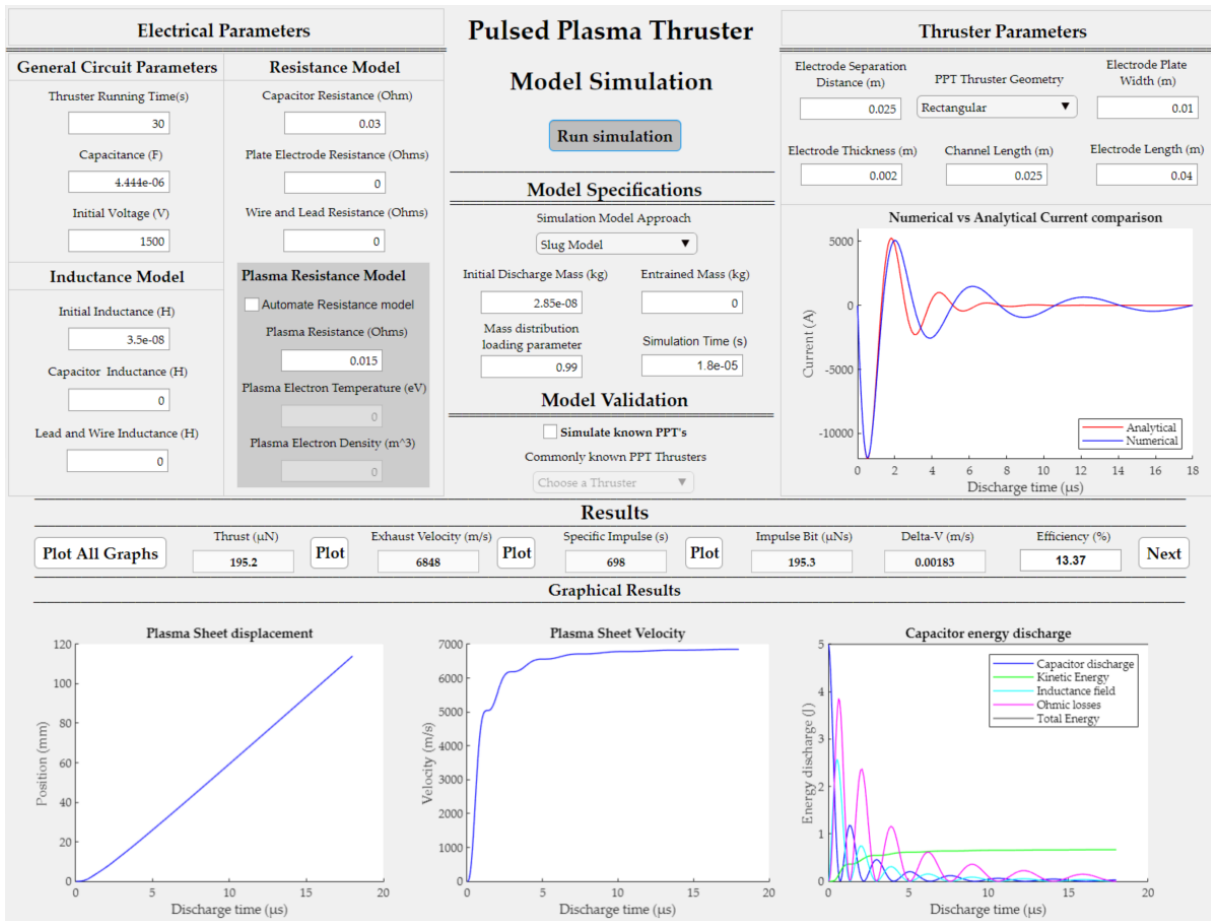


Figure 4-25 Numerical simulation for preliminary μ PPT design

From the initial voltage to capacitance ratio in section 4.7.1 and the aspect ratio within section 4.7.2, performance evaluations were conducted. From the initial voltage to capacitance tests, results show that the thruster performs best when subjected to 4.44 μ F capacitance operating at

1500 V. From the aspect ratio tests, results show that separating the electrodes by 25 mm, with an electrode width of 10 mm, delivered the best results. To simulate this model, estimated input parameter values are used from thrusters of similar stature. These estimated values include the circuit resistance, plasma resistance, initial inductance, and the initial discharge mass. Using these input parameters within the numerical simulation shown in Figure 4-25, the best theoretical results are presented.

To summarise the performance results of Figure 4-25, Table 4-7 is presented.

Table 4-7 Preliminary design performance simulation results

Performance parameter	Result
Thrust	195.2 μN
Exhaust velocity	6848 m/s
Specific impulse	698 s
Impulse-Bit	195.3 $\mu\text{N}\cdot\text{s}$
Efficiency	13.37 %

4.8 Summary and Conclusion

Within this chapter, insight into the implementation of the general electromechanical slug model was presented. This includes the simplifications and assumptions which were made, followed by the general electromechanical mathematical model used for this work. For user compatibility, a software application was described with a user interface presentation and description. This was followed by a model validation for software reliability support. To end the chapter, a design approach was described to determine the required parameters of the thruster. Model simplifications and assumptions allowed for a simplified design, essentially eliminating unnecessary system requirements with minimal performance effects. Furthermore, it was found that designing a software application proved useful to simplify the simulation process, especially when multiple tests and iterations are required. As this numerical model was initially written as a software program, work steered into designing a GUI interface to easily manipulate input data variables within the model. This led to an application with a user-friendly interface that can be installed onto any computer. This improved the simulation time when conducting multiple simulations consecutively. While validating the software model with known thrusters, it was found that non-linearity is apparent in thruster size. For this reason, dedicated time should be spent on the understanding of thruster performance compared to physical parameters. Comparing two known thrusters with the simulation model, show a model accuracy of 81.6% for the LES-6 thruster and 96.48% for the LES-8/9 thruster. From the results, it is concluded that the one-dimensional general electromechanical model predicts the performance characteristics of a parallel plate pulsed plasma thruster very well. The simulation model was used to determine the performance of the thruster. By analysing the initial system voltage, capacitance, electrode separation distance and electrode width with one another, the best performance parameters were determined. Results of the tests concluded that a higher voltage/lower capacitance, as well as an increase in aspect ratio, led to an increase in thruster performance. Therefore, from the simulation tests observed in section 4.7.3, it was concluded that the μ PPT will perform best when a 4.444 μ F capacitor of 1500 V is discharged between two electrodes spaced 25 mm apart, with each electrode 10 mm wide. To conclude this chapter, the addition of a software architecture flow diagram, found in Figure 4-26, is added below to describe the basic working principle of the software application.

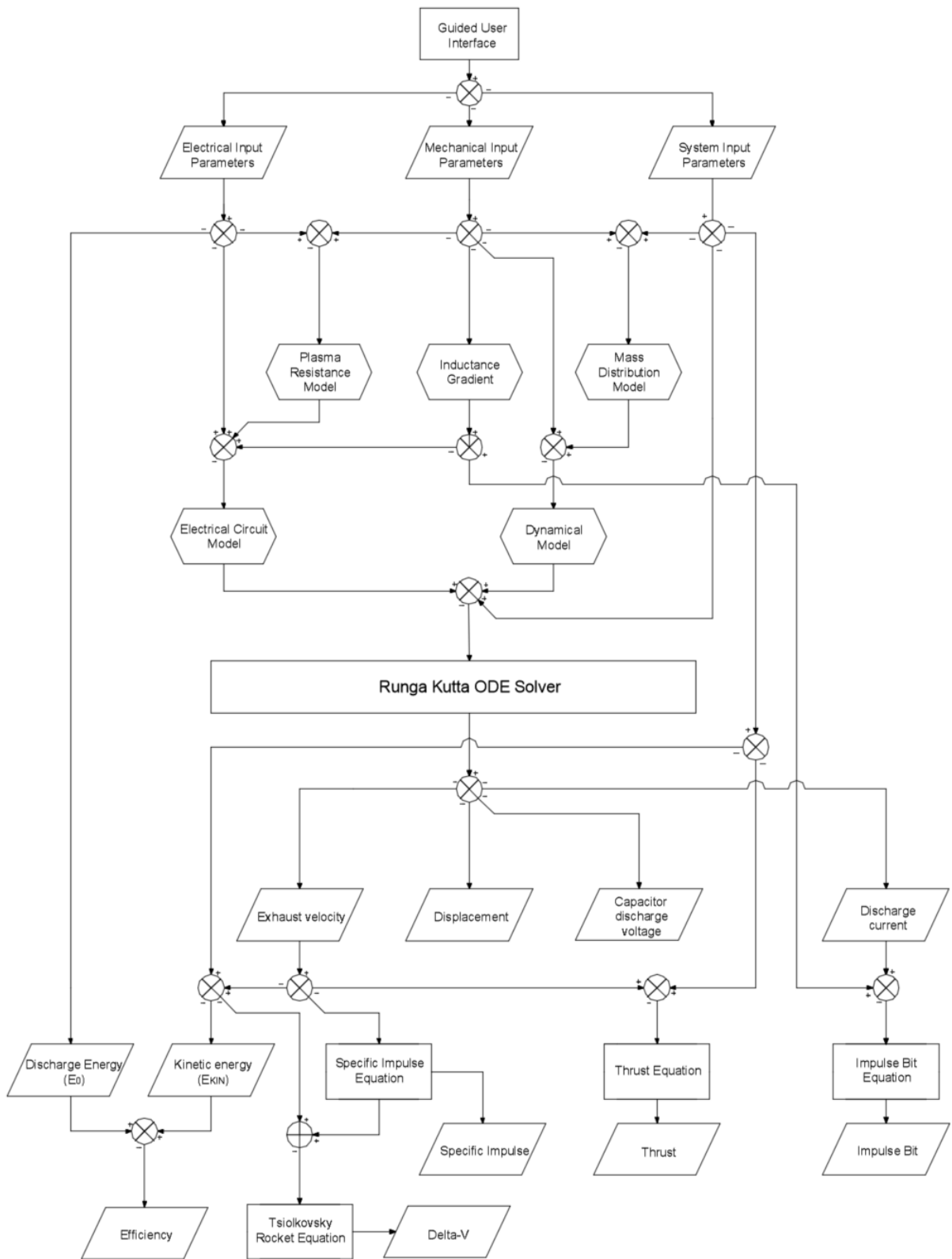


Figure 4-26 Software architecture flow diagram

Chapter 5

Thruster and Power Circuit Design

After a survey was conducted on electric propulsion models found in appendix A, the pulsed plasma thruster was selected from the alternative's propulsion devices. Therefore, in this chapter, three main sections are presented, namely:

- conceptual design,
- preliminary design, and
- final experimental prototype.

Within the conceptual design section, multiple design concepts are presented. These concepts encapsulate both the power circuit and geometry types. Within the power circuit section, the Marx circuit, inductive storage unit and capacitive storage unit are discussed. The geometry section comprises of comparisons between rectangular and coaxial geometries, both consisting of breech-fed and side-fed feeding types. Following this, a preliminary design is presented. The design comprises of the PPT geometry and power circuit designs chosen and discussed in section 5.1 of this chapter while using the additional insight gained from simulations discussed in section 4.7.3 in chapter 4, with regards to choosing the best system parameters. Within the final experimental prototype section, information on the final experimental PPT is presented. This includes a description and visual representation of the design changes made from the preliminary design, the experimental circuit layout, the operation of the mechanical triggering system, a physical description of the working model, and the numerical simulation of the experimental prototype. The experimental prototype is used to analyse the μ PPT operation and to gain an understanding of the field. Therefore, only a partial solution is presented for a flight model μ PPT. To accommodate the complex electrical circuitry, recommended future work is presented in chapter 8.2.

5.1 Conceptual Designs

5.1.1 PPT geometry types

To determine what type of PPT thruster is most suitable for this project, six design geometries are considered. From the subsequent description, Figure 5-1(1),(2),(4), and (6) represent the original PPT geometry designs of Burton & Turchi (1998) as described in section 2.2 in chapter 2. Additional design derivatives are also presented in Figure 5-1, where (3) is a derivative of (1) and (5) is a derivative of (4).

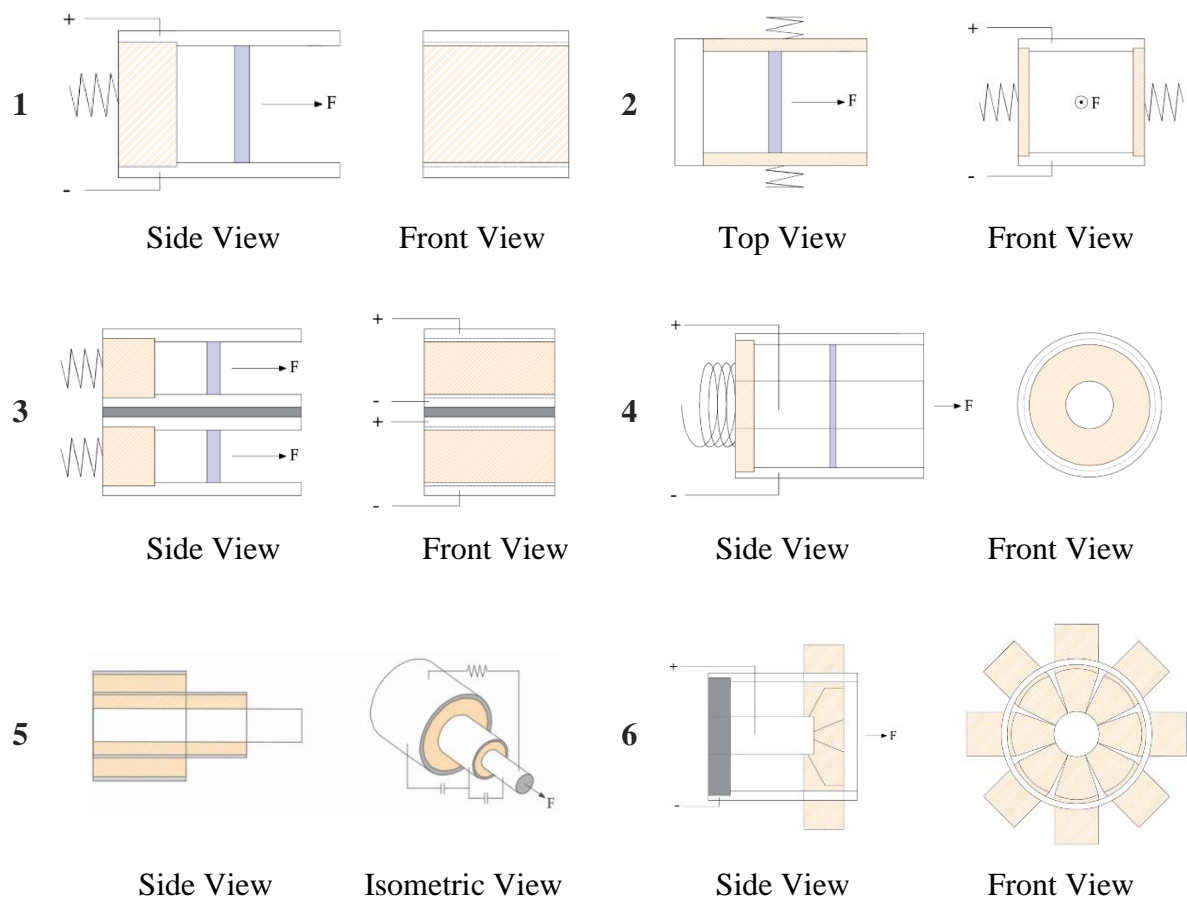


Figure 5-1 PPT geometry design considerations (Adapted from Burton & Turchi (1998)). (Top left) Design 1: Rectangular Breach-fed concept, (Top right) Design 2: Rectangular Side-fed concept, (Middle left) Design 3: Rectangular Breach-fed sandwich concept, (Middle right) Design 4: Coaxial Breach-fed concept, (Bottom left) Design 5: Coaxial three electrode concept, (Bottom right) Design 6: Coaxial side-fed concept.

Design 1 (Rectangular Breech-fed concept)

This design concept is found to be the most common and frequently used among all PPT geometries. It has been used in the LES-6, SMS, LES 8/9 and TIP-II space mission projects (Burton & Turchi, 1998). It is also the only design that has been space verified. Generally, this geometry type adopts the slug model (chapter 3.4) approach since acceleration includes all of the ablated mass as a single unit. Flight and flight-qualified models mentioned above all fall under the rectangular breech-fed geometry.

Design 2 (Rectangular Side-fed concept)

Although not as widely used as the breech-fed geometry, research and development are being carried out for the rectangular side-fed PPT. This geometry type can be found in the MIT-Lab, MIPD-3 and Millipound thruster (Burton & Turchi, 1998). For such a model, the snowplow model (chapter 3.4) approach would be more appropriate due to the accumulation of mass as it accelerates down the channel.

Design 3 (Rectangular Breech-fed sandwich concept) / Derivative of 1

The sandwich rectangular breech-fed type PPT can be seen as a derivative of design 1. It is identical to design 1, but duplicated. Therefore, all of the same principles apply as in design 1.

Design 4 (Coaxial Breech-fed concept)

Since the rectangular and coaxial breech-fed designs are governed by the same equations, with the exception of coordinate systems, the same principles apply to the coaxial breech-fed PPT. Therefore, from this geometry type, the coaxial breech-fed PPT will be best described when using the slug model (chapter 3.4) approach.

Design 5 (Coaxial three electrode concept) / Derivative of 4

This concept design introduces three co-axial electrodes. An 'inner', 'intermediate' and 'outer' electrode, separated by an annulus of Teflon propellant. Within this configuration, the thruster allows for a primary discharge as the 'outer' and 'intermediate' electrode interacts and then a secondary discharge as the 'intermediate' and 'inner' electrode interacts. Similar to Design 4,

this design can best be described by using the slug model approach. This PPT electrode configuration was first seen in the literature of Spanjers & et al (2002).

Design 6 (Coaxial side-fed concept)

In this design, propellant bars are inserted around the inner core of the thruster to form a boundary within the discharge channel. For evaluation, this geometry will require the snowplow model (chapter 3.4) approach, as similarly used in the rectangular side-fed geometry (Design 2).

Having discussed the various designs in Figure 5-1, we will now examine a comparison between the various designs in terms of performance, complexity and thruster characteristics. Testing conducted on side-fed PPTs by Vondra & Thomassen (1972) and evaluated by Guman (1975) provided a platform to understand the relationship between the breech-fed and side-fed PPTs for both the specific impulse and the impulse bit. The principal results showed that the specific impulse is independent of geometry type, while the impulse-bit is dependent on geometry type. Furthermore, the thrust was found to be less with the side-fed thrusters (Burton & Turchi, 1998). With all considered, a geometry comparison was made on designing, building, and testing the thrusters. The critical factors considered included, simplicity, compactness, ease to manufacture, thrust vector accuracy, unit mass and spacecraft contamination. After evaluating designs 1-6 from Figure 5-1, the decision was made to eliminate designs 3 and 5. This was due to the complexity to manufacture, additional power requirements, weight, and lack of basic information. Therefore, only the single rectangular breech-fed and side-fed geometries as well as the general coaxial breech-fed and side-fed geometries were considered. Evaluating these critical factors on a numbering system from 1 (least ideal) to 3 (most ideal), yields,

Table 5-1 PPT geometry comparison

	Rectangular Breech-fed (Design 1)	Rectangular Side-fed (Design 2)	Coaxial Breech-fed (Design 4)	Coaxial Side-fed (Design 6)
Simplicity	3	2	1	1
Compactness	3	2	3	2
Thruster Vector Accuracy	2	2	3	3
Ease of Manufacture	3	3	1	1
Unit Mass	3	2	3	2
Number of Pulses	2	2	3	3
Spacecraft Contamination	2	2	3	3
Total	18	15	17	15

From Table 5-1, it was found that both the side-fed configurations (rectangular and coaxial) fell well short of being chosen. This was primarily due to the complexity of the design, ease to manufacture and overall performance. Comparing the rectangular breech-fed with the coaxial breech-fed geometry, it is shown that the coaxial geometry outperforms the rectangular geometry in minimal spacecraft contamination, number of pulses and thrust vector accuracy. Although the coaxial breech-fed geometry shows promising performance in certain areas, it is seen that the rectangular breech-fed geometry generally outperforms the other PPT geometry types in Table 4-1. Therefore, the rectangular breech-fed geometry was chosen for this project.

5.1.2 PPT Power Circuit Design

To design an electrical system for the pulsed plasma thruster, three distinctive methods were taken into consideration. These three methods are, using a Marx circuit, an inductive storage unit or a capacitive storage unit. The Marx generator, first described by Erwin Otto Marx, can be seen as a circuit converting a low input voltage to a high output voltage. This is done by placing capacitors in parallel while connecting a spark gap in series (Figure 5-2). When voltage breakdown occurs at the spark gap, a series orientation of the capacitors is formed, creating a high voltage.

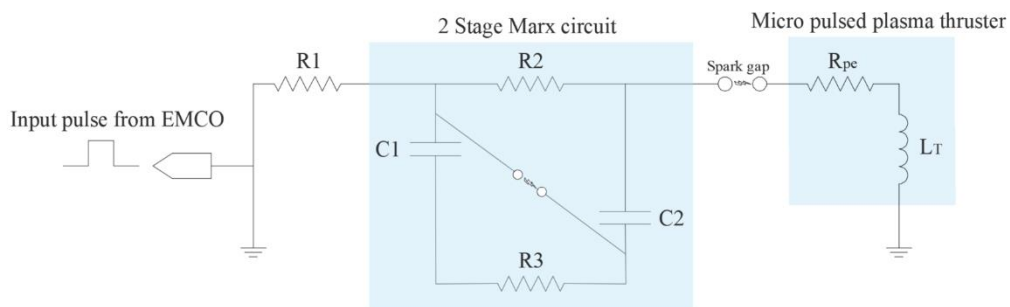


Figure 5-2 Marx circuit representation (Adapted from Eslava (2014))

Burton & Turchi (1998) described the inductance storage unit as a two-stage process (see Figure 5-3). The first stage transfers energy from the capacitor to an inductance store. The second stage transfers the energy from the inductor to the PPT. This is done to compensate for the impedance mismatch between the electrical circuit and the PPT without the complexities of adding a pulse-forming network (PFN). Consequently, this allows for a second discharge at approximately the moment the capacitor voltage reverses. This second discharge can be seen as a second PPT and is visually described in Figure 5-3.

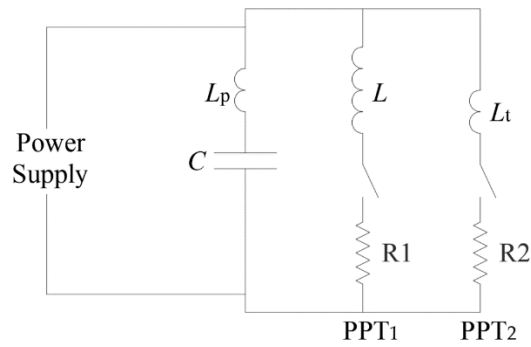


Figure 5-3 Inductive Storage Unit (Adapted from Burton & Turchi (1998))

As previously stated in section 2.5 of chapter 2, a capacitor energy storage unit in its autological nature is described as a physical capacitor being charged up to a required voltage at which voltage breakdown can occur in the thruster. Therefore, these capacitors are generally charged to high voltages between 700-2000V (Eslava, 2014), which leads to the requirement of a DC-DC converter.

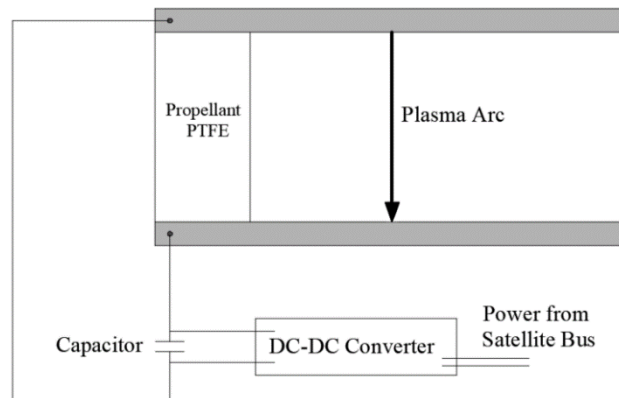


Figure 5-4 Capacitive energy storage unit (Adapted from (Spanjers & et al., 2002))

The capacitive energy storage unit is the most common method used for pulsed plasma thrusters. This type of storage unit is popular, firstly, because of the ‘ease’ at which it can be characterised, and secondly, due to its past success and space heritage as found in the literature (Burton & Turchi (1998), Spanjers & et al (2002) and Pottinger & Scharlemann (2007)).

5.2 Preliminary Design

Within this section, comprehensive descriptions of both the mechanical and electrical designs of the μ PPT are presented. Therefore, within the mechanical design section, a clear description of the mechanical geometry is presented, followed by a descriptive μ PPT extruded design

figure. This is followed by the electrical section described as power circuit design. The power circuit design section consists of an overview, an arc power circuit design description, a triggering circuit design description, and ends off with a preliminary circuit design.

5.2.1 Geometry of PPT

From the conceptual designs mentioned in section 5.1, the parallel plate PPT (design 1) was chosen for further development. Figure 5-5 shows a 3D view of the preliminary μ PPT design. With Teflon being the primary propellant source, a solid Teflon block of (10 x 15 x 26) mm is inserted between the electrodes. Considering an assumed mass flow rate of $2.85e-08$ kg/s, with the propellant block volume amounting to 3750 mm^3 , an adequate amount of testing can be conducted. As the height of the propellant block reaches 25 mm and the width 10 mm, a surface area of 250mm^2 is exposed to the discharge region. Within chapter 4, it can be observed that this configuration delivered the best theoretical results from all the tests conducted. To ensure that the propellant to spark-igniter distance is not affected after multiple discharges, a spring mechanism is inserted to keep the propellant within the discharge region. Copper is the chosen material for the electrodes as it appears to be the most common among the working models. The outer support body consists of 3D-printed ABS plastic. Nylon screws are used to ensure the PPT model stays compact without the risk of electrical conduction. For further information on the preliminary mechanical design in terms of the geometry dimensions, detailed drawings are presented in Appendix B.

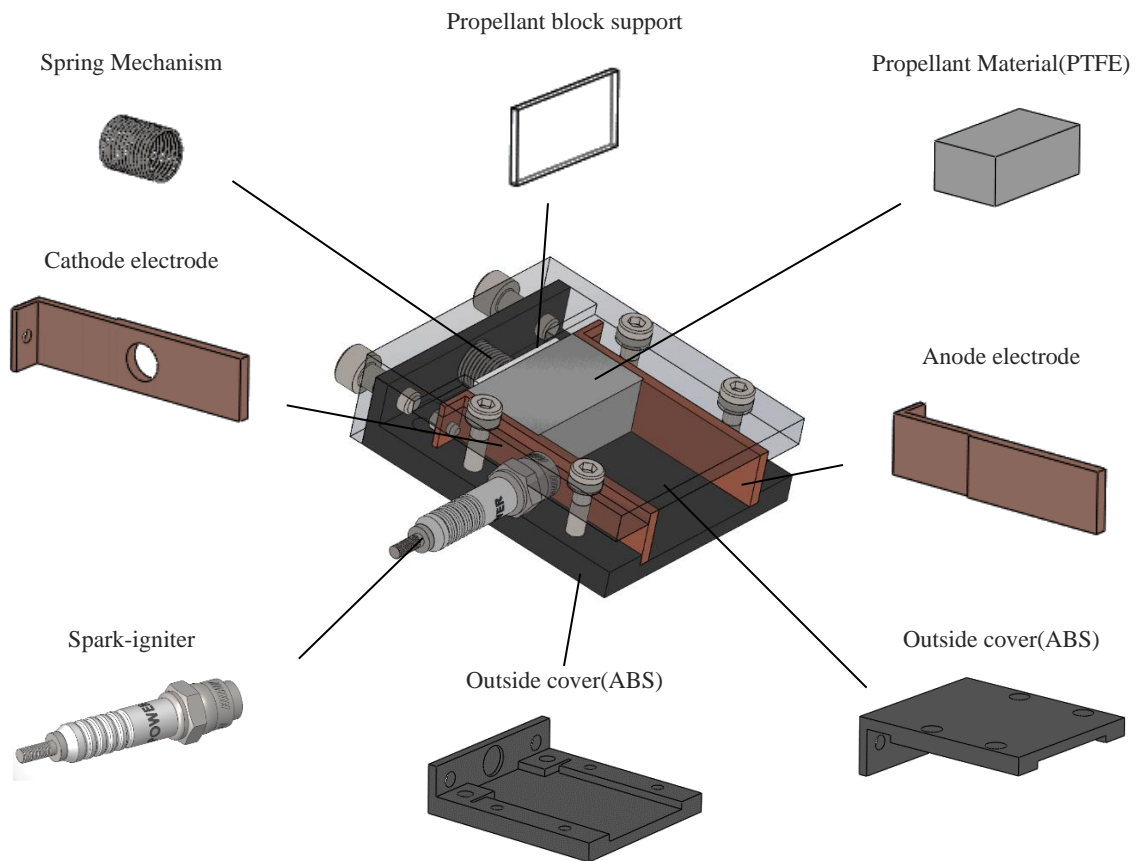


Figure 5-5 Extruded view of the preliminary PPT design

5.2.2 Design of PPT Power Circuit

The work conducted towards this thesis consists of no complex circuitry. Therefore, a partial electrical solution is presented by designing a system focused on delivering the required system power without the complexity of automatically monitoring and controlling the system. Thus, capacitor voltage charge-up and maintenance are done manually, supply voltage and discharge pulses are controlled manually, and all the monitoring of the system is conducted from external devices.

Overview of Arc Power and Triggering Circuits

For the main discharge of a PPT, a systematic sequence of events needs to occur. When the potential between the cathode and anode is at the desired voltage, the spark-igniter is activated to allow for the initial ablation of the propellant material. This leads to the required dielectric

strength within the discharge region for arc generation between the two electrodes. Therefore, as seen in Figure 5-6, two circuits are required for thruster discharge, namely: to charge the capacitors to the required voltage and secondly, to trigger the spark-igniter.

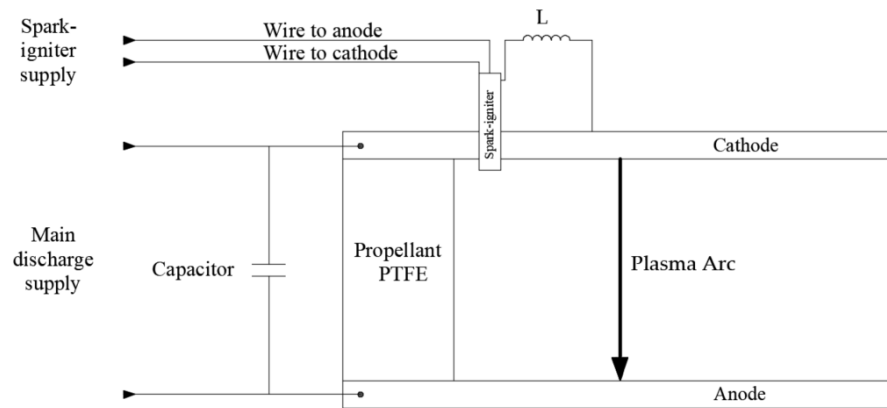


Figure 5-6 PPT power distribution concept

As established in chapter 4, a $4.44 \mu\text{F}$ capacitor operating at a voltage of 1500 VDC delivered the best system performance. Therefore, the main discharge supply and spark-igniter supply, seen in Figure 5-6, is supplied with 1500 V generated by an XP⁴ Power E15 DC-DC converter.

Table 5-2 XP Power E15 specifications

Input voltage	0-12 V
Output voltage	0-1500 V
Output current	2 mA
Minimum operating temperature	-10 °C
Maximum operating temperature	+60 °C

From the product specification sheet of the DC-DC converter, it is found that a 12V input is required to deliver the desired voltage output of 1500V. This input voltage will be supplied by an external DC power supply.

Arc Power Circuit

As discussed in the previous section, a 1500 V output will be used to charge the main capacitors. To do this, a current limiting resistor is required. This is due to the maximum current capabilities of the DC-DC converter observed in Table 5-2. As the capacitor charging circuit is limited to a

⁴XP Power is the manufacturer of the E15 DC-DC converter

maximum drawing current of 2 mA and the required voltage is 1500 V, Ohm's law is used to determine the current limiting resistor. From the above-mentioned parameters, it is calculated that a 750 k Ω resistance is required to limit the circuit current to 2 mA. Therefore, the electrical design can be represented as

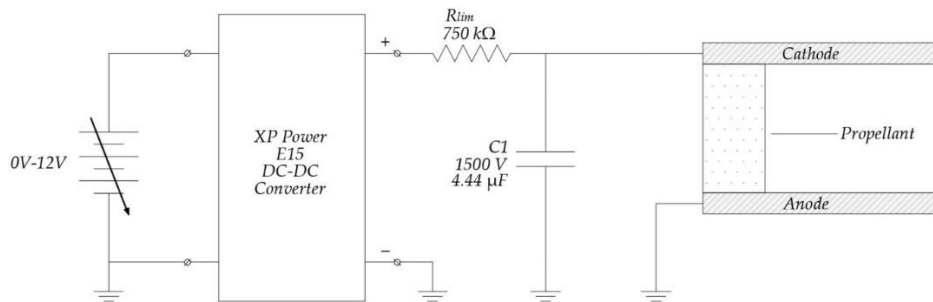


Figure 5-7 preliminary design of the main discharge circuit

Triggering Circuit

As discussed in section 2.6, an initial ablation of propellant is required to create a conducting path for the main discharge. After evaluating all the possible candidates in Table 2-7, it was found that the triggerless vacuum arc ignition system is best suited for this project due to the simplicity of design. Therefore, this system only requires an arc switch and booster system. As the general spark-igniter operating voltages measure between 700 V and 2000 V (Eslava, 2014), the spark-igniter voltage is rated at 1500 V. The spark-igniter circuit is presented below in which a discharge capacitor is charged up to 1500 V. Similar to the arc power circuit, a current regulating resistor of 750 k Ω is placed in series with the discharge capacitor to protect the DC-DC converter from inrush current.

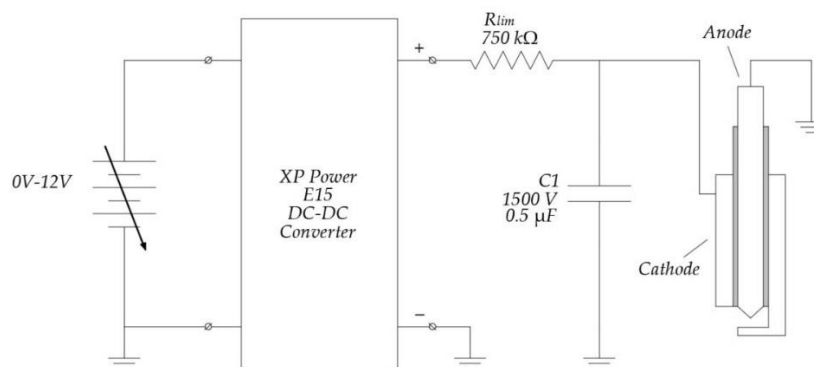


Figure 5-8 Preliminary design of spark-igniter discharge circuit

Preliminary Circuit Design

Figure 5-9 shows the combined electrical circuit, consisting of two individual circuits namely, the main plasma discharge circuit and the triggering circuit. To control the charge and discharge of the system, a control signal operation (Appendix E) or mechanical switching is required.

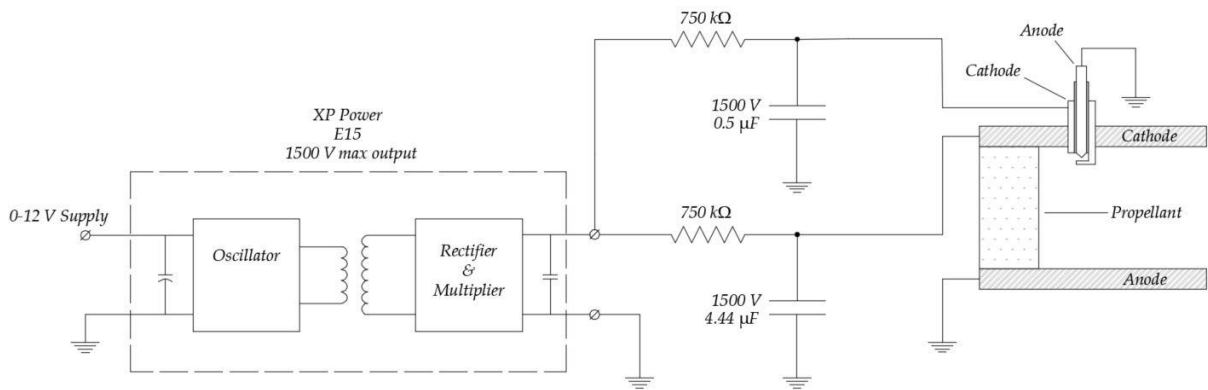
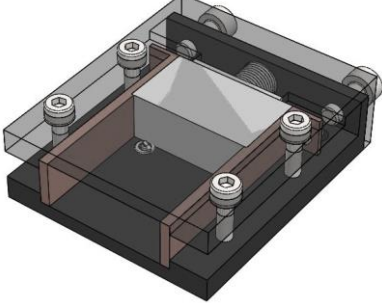
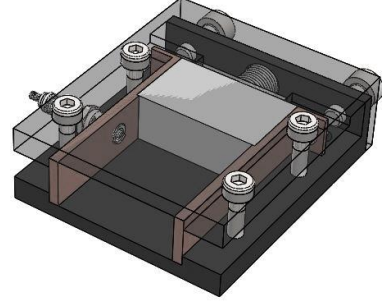


Figure 5-9 Preliminary circuit design

5.3 Final Experimental Prototype

Practical implications prevent the experimental prototype from adhering to the preliminary design. Therefore, the ideally 4.44 μF capacitor operating at 1500 V is substituted with two parallel CBB15-1200-3 Film capacitors of 3 μF operating at 1200 V. Irrespective of the design change, the circuit still consists of a capacitive storage unit supplied by a standard laboratory DC power supply. To reach a 1200 V discharge voltage, an E15 XP power DC-DC converter is used. Considering a thruster discharge frequency of 1 Hz, the power of the thruster equals 4.32 W.

Table 5-3 Experimental prototype and preliminary design parameters

Experimental Prototype		
Operation Parameters	Values	Visual representation of 40 mm electrode thruster
Capacitance	6 μ F	
Rated initial voltage	1200 V	
Rated discharge energy	4.32 J	
Electrode separation distance	25 mm	
Electrode width	10 mm	
Electrode thickness	2 mm	
Electrode length	40 mm	
	25 mm	
Preliminary Design		
Operation Parameters	Values	Visual representation
Capacitance	4.44 μ F	
Rated initial voltage	1500 V	
Rated discharge energy	4.995 J	
Electrode separation distance	25 mm	
Electrode width	10 mm	
Electrode thickness	2 mm	
Electrode length	40 mm	
	40 mm	

During the physical construction of the μ PPT, a difficulty arose in placing the spark-igniter into the electrode. This was due to the trouble of electrically isolating the spark-igniter from the cathode electrode. Therefore, it was decided to shift the spark-igniter from the electrode (preliminary design) to a perpendicular position within the outer casing of the μ PPT (experimental prototype). This change in position can be seen in Table 5-3 when viewing the position of the spark-igniter in the experimental prototype and the preliminary design. Furthermore, as previously presented in the preliminary power circuit design (chapter 5.2.2), no complex circuitry is used within the experiment. Therefore, a mechanical triggering system, described in Table 2-7, is used within the experimental work and presented in Figure 5-10.

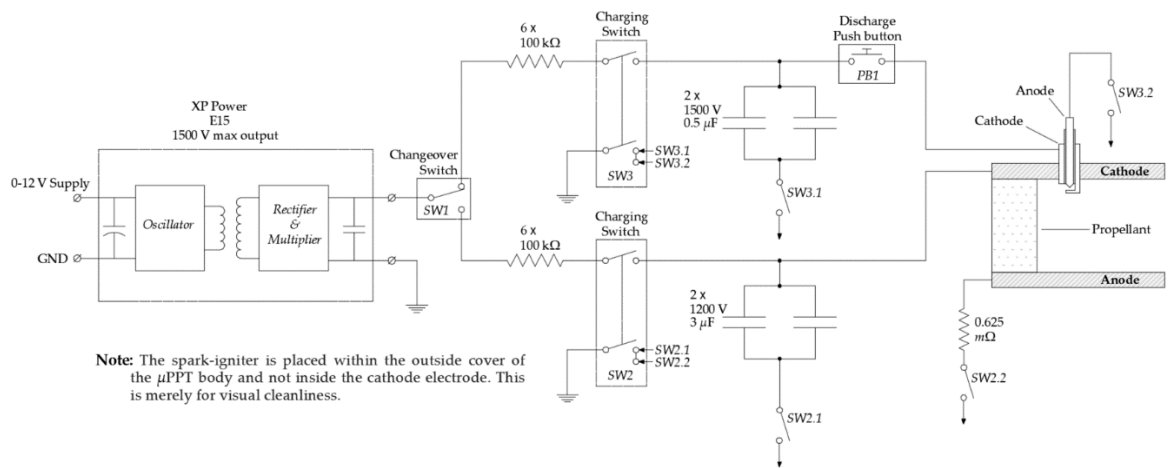


Figure 5-10 Circuit layout for the experimental prototype using a mechanical triggering mechanism

To accommodate the current capabilities of the DC-DC converter, a set of 6 x 100 kΩ resistors were added to both the main discharge circuit and the spark-igniter circuit. From Figure 5-11, it was determined that a theoretical voltage of 9.6 V is required at the input of the DC-DC converter to charge the capacitors to 1200 V.

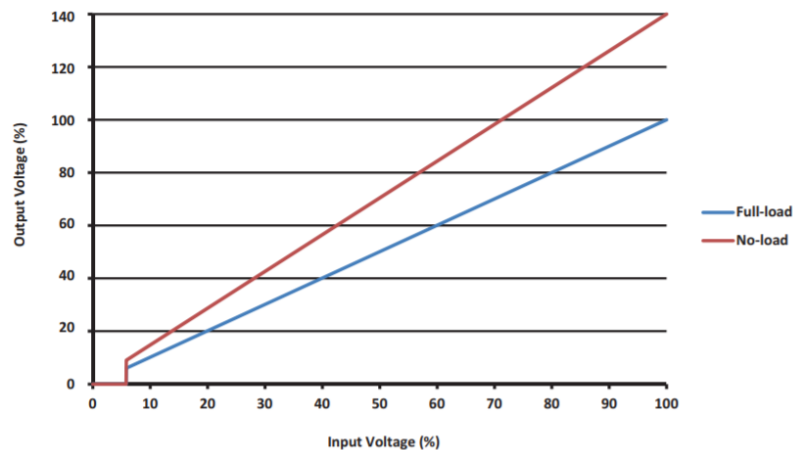


Figure 5-11 XP Power E15 input to output ratio (Power, 2020)

As previously mentioned in the preliminary power circuit design within section 5.2.2, a systematic sequence of events needs to occur for a PPT discharge. Therefore, the mechanical triggering system used to charge and discharge the experimental μPPT is presented in Figure 5-12. This is followed by the operating sequence description in Figure 5-13.

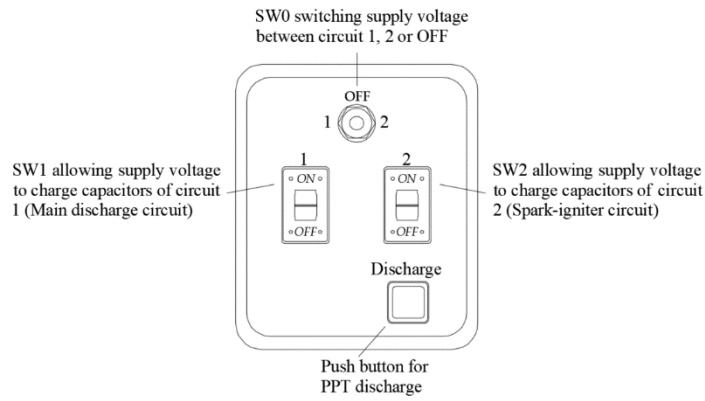


Figure 5-12 Circuit enclosure and mechanical trigger interface for experimental prototype testing

To describe the operating sequence of the experimental prototype within this thesis, a descriptive summary is presented in Figure 5-13.

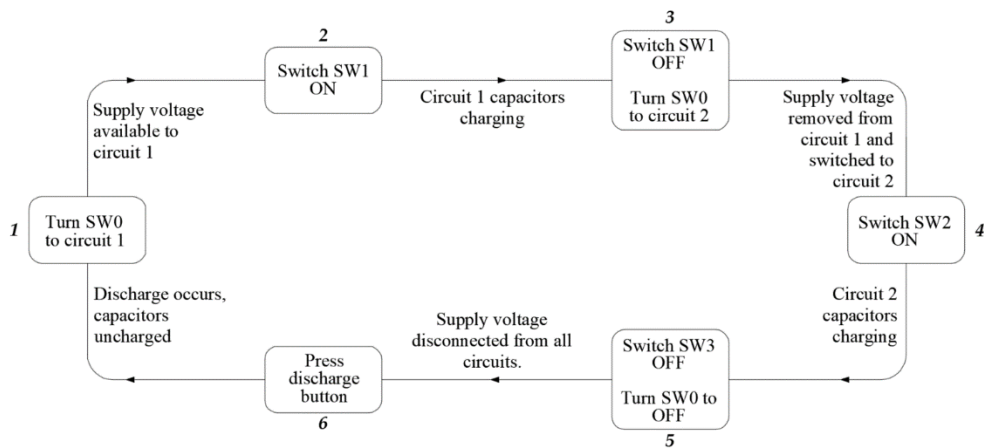


Figure 5-13 μ PPT operation sequence for both the charging and discharging of the main circuit and the spark-igniter circuit.

Furthermore, for all mechanical designs, the experimental prototype remains unchanged from the preliminary design, except for the spark-igniter position and electrode length. As a PTFE (Teflon) block of (25×10×15) mm was used, the discharge region is exposed to 250 mm² of surface area. With copper electrodes, ABS outer covers, nylon screws and a spring to keep the propellant against the discharge region, all experimental changes towards the mechanical section focused on the spark-igniter moving from the cathode electrode to a perpendicular position within the μ PPT casing. To ensure that the discharge arc avoids the spark-igniter and transfers to the anode, a 270 nH inductor was connected between the cathode electrode and the spark-igniter. To summarise the experimental prototype, Figure 5-14 is presented to visually describe the construction of the μ PPT. This is followed by the overall μ PPT parameters consisting of both mechanical and electrical sections.

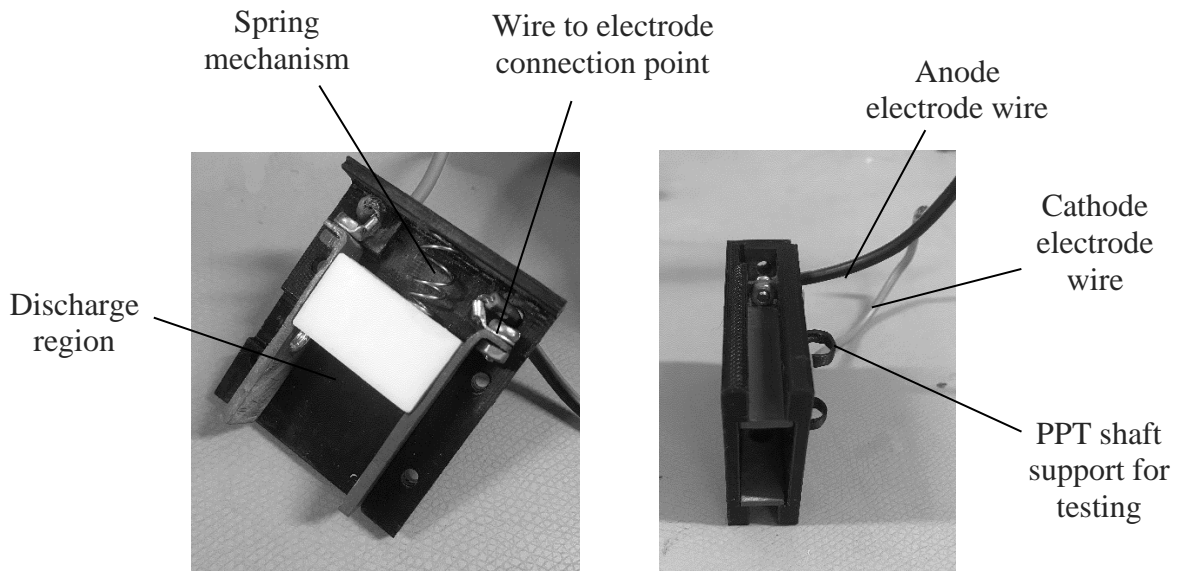
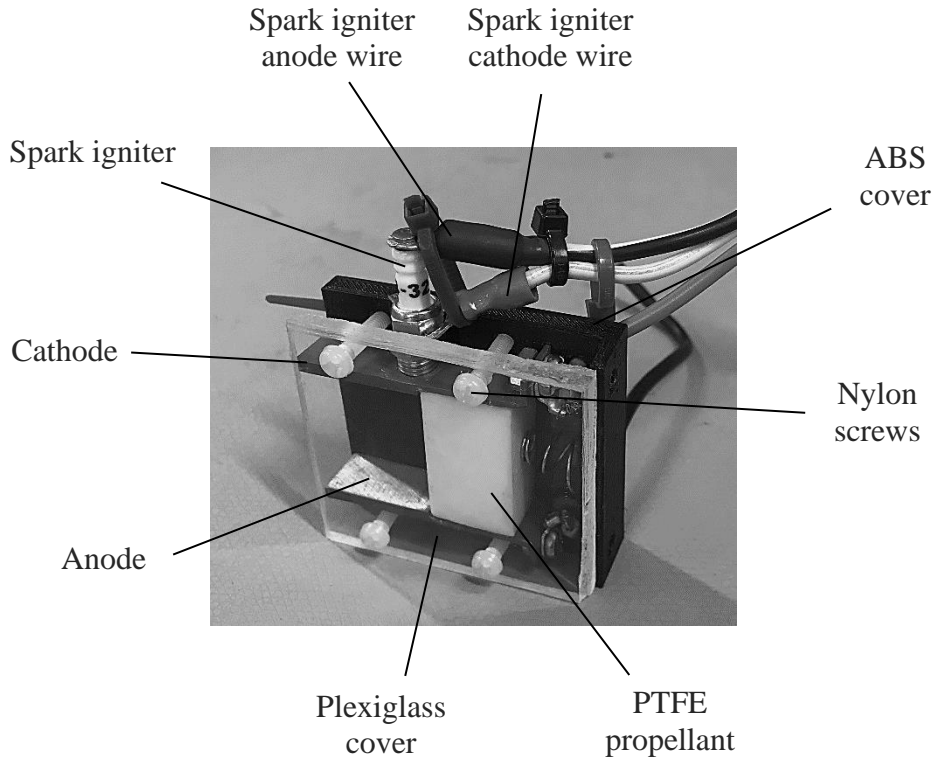


Figure 5-14 Final experimental design

Table 5-4 Measured parameters for experimental prototype

Geometry Type	Rectangular
Feeding Type	Breech-fed
Electrode width	10 mm
Electrode length	40 mm
Electrode thickness	2 mm
Electrode separation distance	25 mm
Chamber length	30 mm
Electrode material	Copper
Propellant Material	PTFE
Spark-igniter voltage	1200 V
Power	4.32 W
Capacitor voltage	1200V

Considering the change of input parameters from the preliminary design to the experimental prototype, a numerical simulation was conducted within the MATLAB® application to determine the estimated performance values of the experimental prototype. Therefore, the input parameters for this simulation are presented in Table 5-4. Additional input parameters are presented below in Table 5-5.

Table 5-5 Additional input parameters for the numerical simulation on the experimental prototype

Parameters	Values
Initial inductance	†35 nH
System resistance	†0.045 Ω
Mass shot	†28.5 μg

† Estimated values

Observing Table 5-6, a clear decrease in overall performance is presented when comparing the experimental prototype simulation results with the preliminary design simulation results. Therefore, it should be stated that the experimental prototype does not represent the ideal design, but it appears to be satisfactory for the experimental work for this thesis.

Table 5-6 Numerical simulation results of experimental prototype and preliminary design using the MATLAB® application

Experimental prototype results from numerical model		Preliminary design results from numerical model	
Result	Value	Result	Value
Thrust	165.6 μ N	Thrust	195 μ N
Exhaust velocity	5803 m/s	Exhaust velocity	6841 m/s
Specific Impulse	591.9 s	Specific Impulse	697.3 s
Efficiency	11.13 %	Efficiency	13.36 %
Discharge energy	4.32 J	Discharge energy	4.995 J
Impulse-Bit	165.6 μ N-s	Impulse-Bit	195 μ N-s
Discharge current	10.52 kA	Discharge current	11.9 kA

5.4 Summary

Within this chapter three design processes were presented, namely: the Conceptual design, preliminary design, and experimental prototype. Within the conceptual design, the rectangular breech-fed pulsed plasma thruster operating with a capacitive-driven circuit was chosen. From a geometry type comparison, it was found that the rectangular breech-fed design generally performed the best out of all the geometry types. Within the power circuit design, the capacitive energy storage unit was favoured due to its wide popularity and ‘ease’ to characterise.

Within the preliminary design, a detailed description of the rectangular breech-fed geometry was presented which was followed by a visual representation. Thereafter, an overview of the arc power and triggering system was presented. From the overview, an arc power circuit and triggering circuit was presented and discussed individually. After the description of these two circuits, a preliminary circuit design was presented and discussed. The preliminary circuit design led to a 4.44 μ F capacitor operating at 1500 V for the main discharge circuit and a 0.5 μ F capacitor operating at 1500 V for the spark-igniter circuit. To limit the current to 2 mA for both circuits, it was determined that a 750 k Ω resistor is required and placed in series with both the main discharge capacitor and the spark-igniter capacitor.

Within the final experimental prototype section, design changes from the preliminary design to the experimental prototype were presented. This was followed by a visual representation of the physical circuit developed. As the system operates with a mechanical triggering system, the

operating sequence of the system was presented. A revision on the charge/discharge sequence of the experimental prototype is presented in Figure 5-7.

Table 5-7 Experimental charge/discharge sequence revision

Sequence	Description
1	Turn SW1 to the main discharge circuit (1). This will allow access to the supply voltage delivered by the DC-DC converter
2	Switch SW2 on and allow the capacitors to charge.
3	Once the discharge capacitors in circuit 1 have reached the desired voltage, switch SW2 off and change SW1 over to the spark igniter circuit (2).
4	Switch SW3 on and allow the capacitor to charge.
5	Once the discharge capacitors in circuit 2 have reached the desired voltage, switch SW3 off and change SW1 over to OFF.
6	Push the discharge button and observe a PPT discharge.

Furthermore, using camera images of the μ PPT, a physical description of the experimental prototype was presented. To end the chapter, a numerical simulation of the experimental prototype was conducted within the MATLAB® application. From the results, it was estimated that the μ PPT will deliver 165.6 μ N of thrust with an exhaust velocity of 5803 m/s, a specific impulse of 591.9 s and a thruster efficiency of 11.13%.

Chapter 6

Experimental Setup and Test Procedures

In this chapter, all experimental work relating to the pulsed plasma thruster is discussed. This includes the experimental test setups, describing the implementation of instrumentation, and why variable electrode lengths are tested. Within the experimental test setup section, four critical points are discussed concerning the setup of the experimental tests. These points include a clear description of the components required outside of the vacuum chamber, a clear description of the components inside of the vacuum chamber, displaying the circuit to be tested, and showing how the circuit will be connected to the measuring equipment. Thereafter, an experimental test methodology is introduced to clearly define the testing methods used for this thesis. These experimental tests are conducted to gain an understanding of pulsed plasma thrusters. Therefore, the section discusses the voltage discharge, current discharge, and thrust generated. These variables are used to characterise the overall plasma propulsion system. First, a 40 mm electrode μ PPT (Experiment 1) is tested to evaluate the voltage, current, and thrust results. This is followed by an adjusted electrode length PPT where the experiments are repeated (Experiment 2). The secondary experiment is to evaluate the effect of electrode length on the μ PPT performance. To end the chapter, a torsion balance system is introduced to determine the thrust of the μ PPT. To ensure a reasonable level of thrust measuring accuracy, an oscillation technique is applied to calibrate the torsion balance. Table 6-1 summarizes the experimental tests to be conducted. All experiments were conducted in the physics lab located in the Electrical, Electronics and Computer engineering building, room B0.03.

Table 6-1 Experimental test descriptions

Experiment	Description
Experiment 1	Within this test, voltage, current and thrust performance parameters are measured for a 40 mm electrode μ PPT. To do this, an HV attenuator, shunt resistor and self-made thrust balance are used.
Experiment 2	Within this test, voltage, current and thrust performance parameters are measured for a 25 mm electrode μ PPT. To do this, an HV attenuator, shunt resistor and self-made thrust balance are used.

Note: Within both tests, various voltages and pressures were evaluated to gain an understanding of the μ PPT under variable operating conditions.

6.1 Experimental Test Setup

Within the experimental tests, the μ PPT performance is evaluated under variable conditions. Most propulsion characteristics for EP systems depend on the voltage discharge, current discharge, and thrust of the μ PPT. Therefore, those three parameters are examined. Tests were performed using a degassing cylindrical chamber of 200 mm in diameter and 200 mm in depth, connected to a rotary pump to set the operating pressure at approximately 0.75 Torr within the chamber. Table 6-1 summarizes the experimental tests to be conducted.

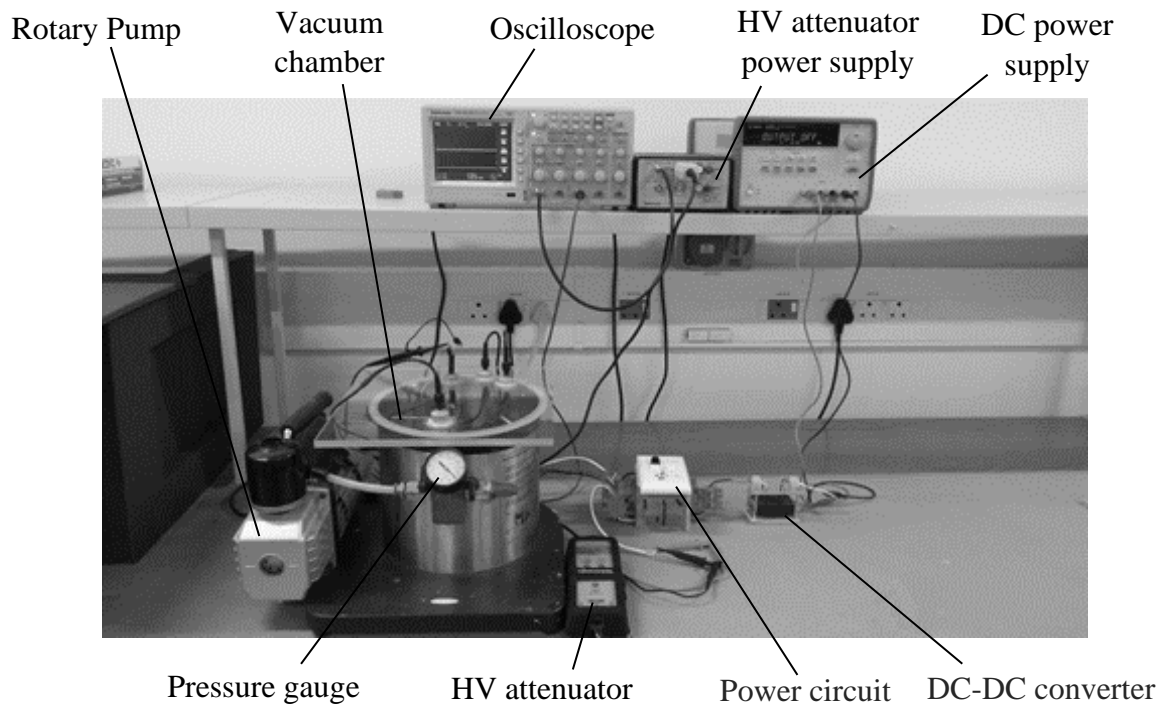


Figure 6-1 Experimental test setup for all equipment outside of the vacuum chamber

In addition, an Agilent E3634A DC power supply is used to supply the DC-DC converter with the required input voltage, while a Tektronix TDS2024B oscilloscope is used to measure the various electrical signals. To measure the high voltages within the system, a high-voltage Tektronix P5205 attenuator is used, which is capable of measuring up to a maximum voltage of 1.3 kV. As mentioned in chapter 5.3 and observed in Figure 6-1 and Figure 6-3, all charge and discharge cycles were operated manually via switches. All of the components within the vacuum chamber are presented in Figure 6-2. This includes the μ PPT itself, combined with the capacitor banks for both the spark-igniter circuit and the main discharge circuit. Additionally, a shunt resistor and thrust balance are placed within the vacuum chamber to measure the discharge current and the thrust, respectively. The current is calculated by measuring the voltage drop over the shunt resistor and the thrust is measured with a self-made thrust balance. The self-made thrust balance incorporates a laser, mirror, and a graded scale. A full description of the current measurement is found in section 6.2, and that of the thrust balance can be found in section 6.3.

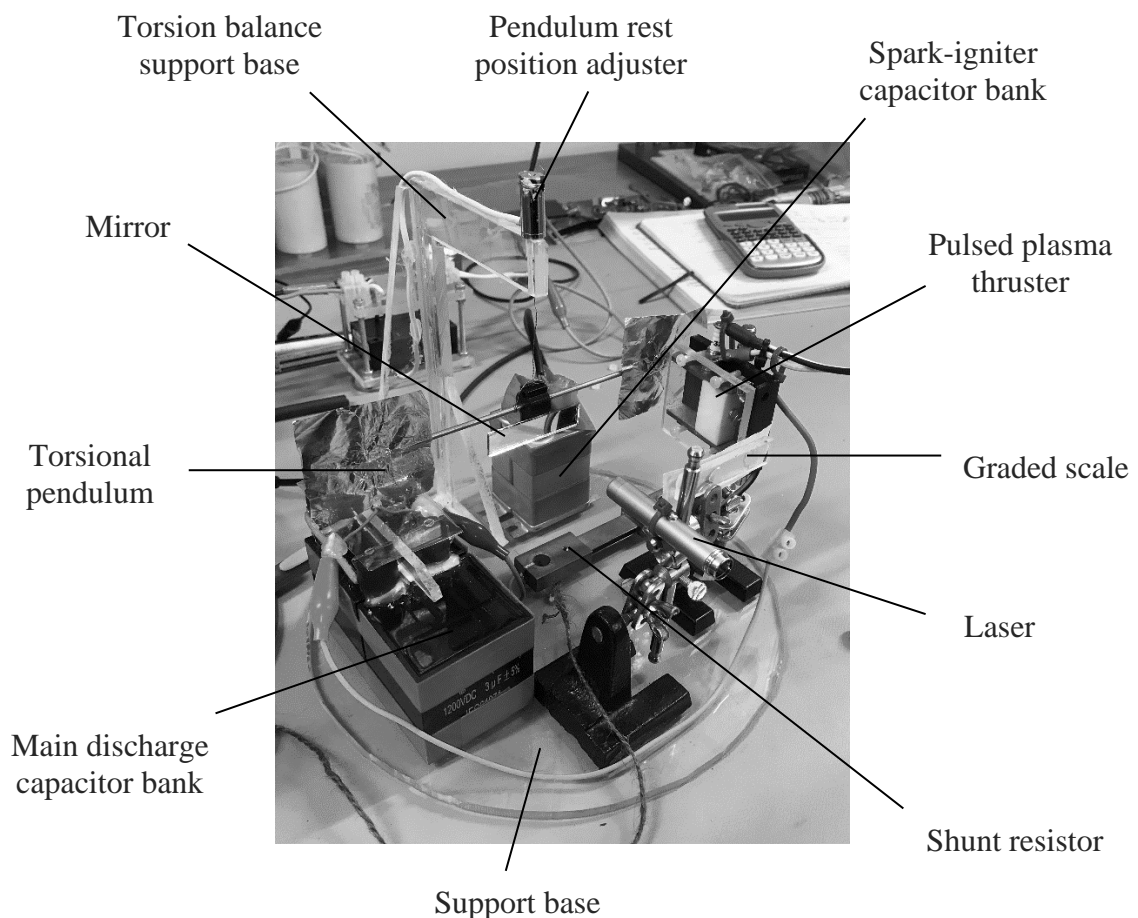


Figure 6-2 Experimental test setup for all components inside of the vacuum chamber

The electrical circuit for both experiment 1 and experiment 2 is shown in Figure 6-3 and Figure 6-4. This shows the setup for the electrical measurements to be made.

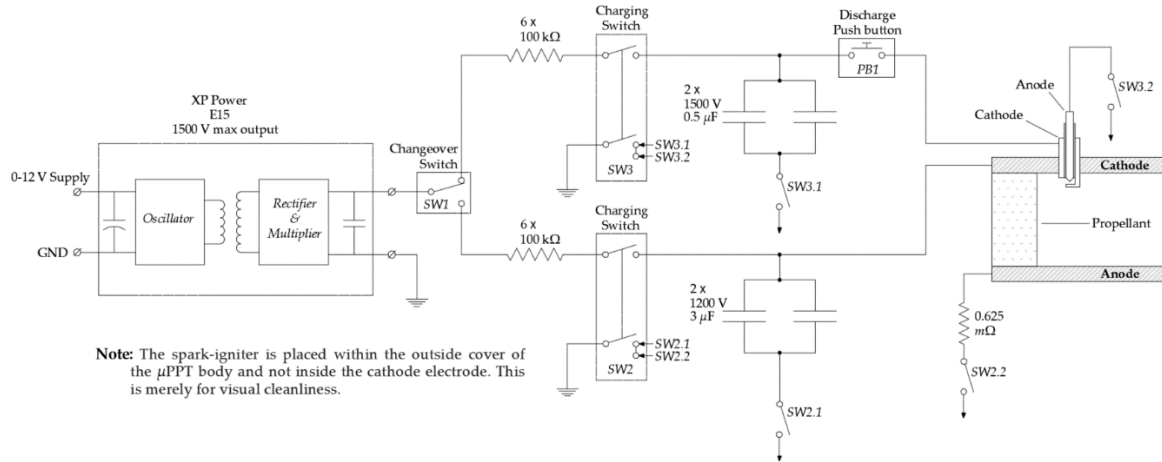


Figure 6-3 Circuit layout of experimental prototype to test both experiment 1 and experiment 2

To measure the voltage and current discharge, two voltage probes are required. The first probe is placed across the main capacitor bank. The second voltage probe measures the voltage drop over the shunt resistor. For a visual illustration, Figure 6-4 is presented.

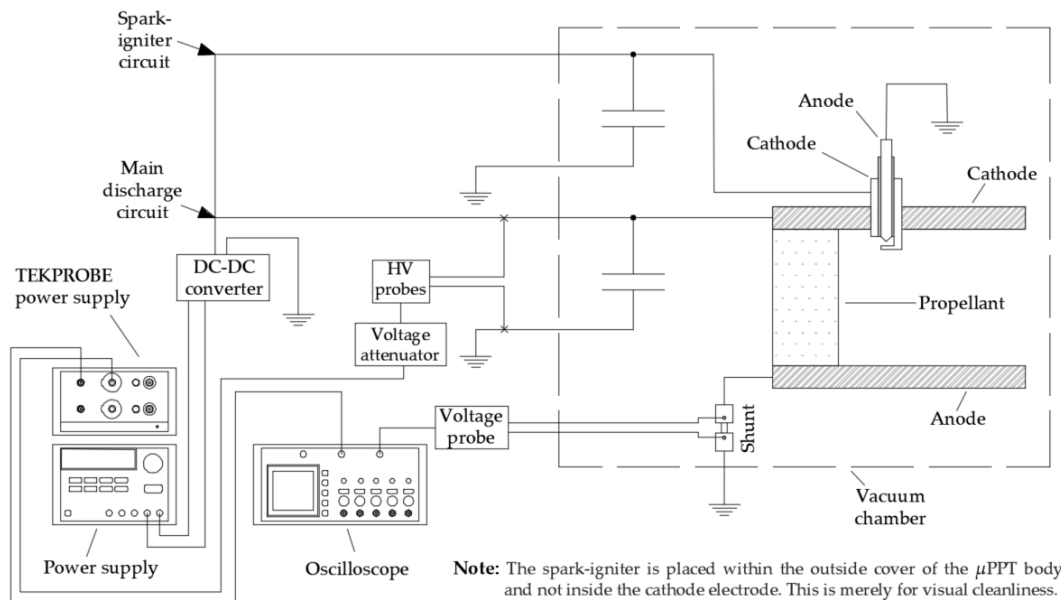


Figure 6-4 Instrumentation setup of experimental prototype tests. This includes the voltage measurements for both the voltage discharge and current measurements.

6.2 Experimental Testing Approach

Within this section, the experimental testing approach is described. For this purpose, three desired variables are discussed, namely: voltage discharge, current discharge, and generated thrust. Thereafter, the significance of the impulse-bit is discussed and the relationship with the thrust generated is explained. To end the section, the effect of electrode length on thruster performance is explained, followed by a discussion on the experimental tests to be conducted.

Voltage discharge measurements

During initial testing, a self-made voltage divider was used to measure the voltage discharge of the μ PPT. Due to the unsatisfactory results delivered by the voltage divider, further tests were done using a commercial high voltage (HV) attenuator. Therefore, the Tektronix P5205 voltage attenuator is used to determine the voltage discharge of the μ PPT. As the attenuator is restricted to a maximum input voltage of 1.3 kV, the maximum attenuation setting of 500x is used. From the voltage discharge curve, five parameters are identified which can contribute to the understanding of the μ PPT. These parameters are:

- The system resistance,
- Is the system over/under or critical damped?
- Does the capacitor release all of its energy?
- How smooth is the supply voltage and how accurately is it delivered?
- The discharge time.

Current discharge measurements

For the determination of the μ PPT discharge current, a shunt resistor is used. This method was primarily chosen due to the difficulty of sourcing a desirable Rogowski coil. By measuring the volt drop over the shunt resistor, Ohm's Law can be used to determine the discharge current. The shunt resistor is placed in series between the anode electrode and the capacitor (Figure 6-5). To ensure that the shunt resistor has minimal effect on the system, a low resistance was required. Therefore, a 0.625 m Ω shunt resistor is used. Using the numerical peak current obtained during the experimental prototype simulation, a 6.575 V drop is expected for a 1200V system.

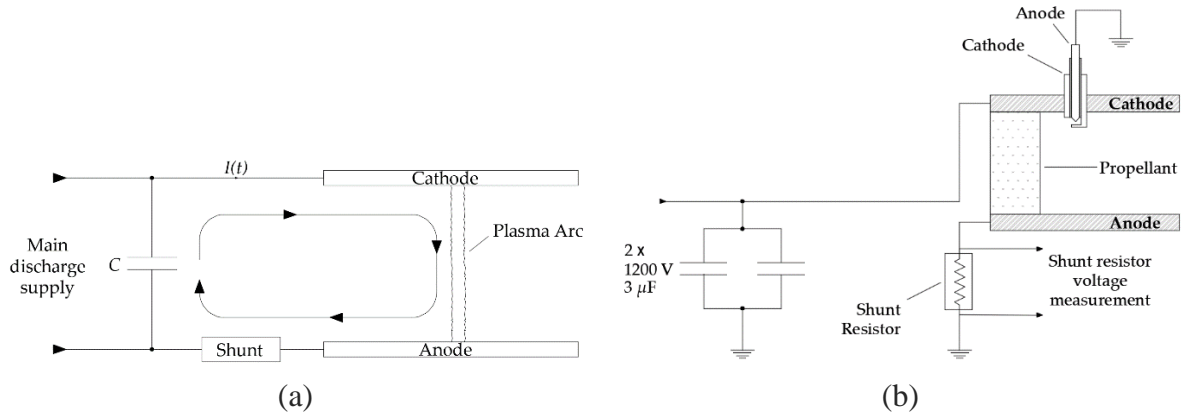


Figure 6-5 Implementation of current measuring shunt resistor into the experimental circuit

From the current discharge measurements, the plasma resistance can be estimated using the plasma resistance model from equation (3-30). Furthermore, the impulse-bit of the thruster is determined by the multiplication of half the inductance gradient and the integral of the current squared found in equation (2-1).

Thrust measurements

In this thesis, the thrust of the μ PPT is measured using a torsional thrust balance. This torsion balance is described in section 6.3. A laser, mirror, and graded scale are utilized to determine the angle of rotation of the pendulum arm. To ensure a fair amount of measurement accuracy, a calibration technique is applied by determining the natural oscillating frequency caused by the torsional constant of the wire. From the thrust derivation described in chapter 6.3, it was determined that the thrust of the μ PPT is represented by,

$$F_{\text{PPT}} = \frac{4\pi^2\theta}{T_{\text{oscillation}}^2} \left[R_{\text{rod}} \left(\frac{1}{3}m_{\text{rod}} + 2m_{\text{foil}} \right) + \frac{m_{\text{con}}(a_{\text{con}}^2 + b_{\text{con}}^2) + m_{\text{mir}}(a_{\text{mir}}^2 + b_{\text{mir}}^2)}{12} \right] \quad (6-19)$$

Where F_{PPT} is the force generated by the μ PPT, $T_{\text{oscillation}}$ is the oscillation period of the pendulum, θ is the rotational angle of the pendulum, R_{rod} is the radius of the rod, m_{con} is the mass of the connecting pin, a_{con} is the width of the connecting pin, b_{con} is the length of the connecting pin, m_{mir} is the mass of the mirror, a_{mir} is the width of the mirror, b_{mir} is the length of the mirror and m_{foil} is the mass of the foil sheet.

The effect of variable electrode lengths on μ PPT performance

From the research conducted by Guman & Peko (1968), Arrington et al. (1997) and Rezaeiha & Schonherr (2012), ambiguity is observed in the effect of electrode length on the thruster performance. Research by Guman & Peko (1968) concluded that shorter electrodes deliver higher specific thrust (Thrust/ Power) and specific impulse, whereas research by Arrington et al. (1997) concluded that longer electrodes deliver higher specific impulse and thruster efficiency but deliver lower specific thrust and impulse-bit. Since both these experiments were conducted under the same operating conditions, except for different discharge energies; researchers posed the question of whether there is a possible correlation between the electrode length, discharge energy, and performance (Rezaeiha & Schonherr, 2012). Furthermore, evaluating the current flow within a discharge cycle of a parallel plate PPT, illustrated in Figure 6-6, it is shown that the current through the electrode stretches only as far as the plasma arc is distanced from the propellant (x_s). As no/minimal current flows through the additional electrode material (marked with an \times in Figure 6-6), it is assumed that no magnetic fields contribute to the acceleration of the discharge material in that region.

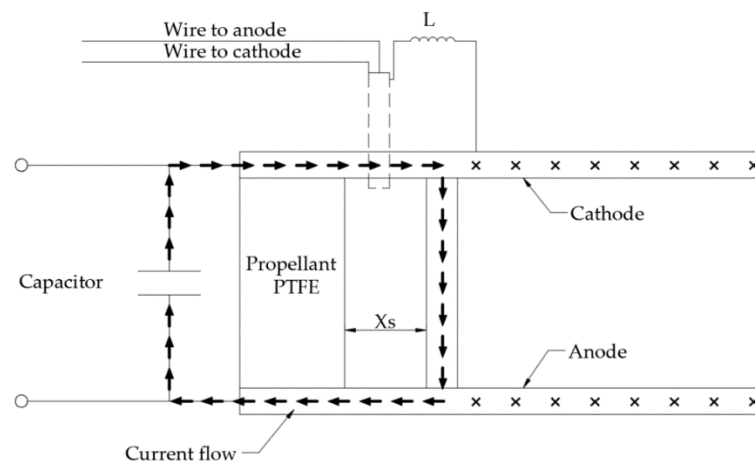


Figure 6-6 Parallel plate PPT current discharge path

Throughout experiment 1, a discharge region is given by the positioning of the cathode spots⁵ generated after multiple discharges. Evaluating the cathode spots after experiment 1, the electrodes are shortened, and experimental tests are repeated within experiment 2. For more insight into the cathode spots region, section 7.2.5 in chapter 7, section 8.2.2 in chapter 8 and the literature of Jonathan Lun (2008) can be read.

⁵ Cathode spots is the result of emission of cathode material due to the high energy discharge. This essentially causes small holes in the electrode known as spots. This phenomenon is directly related to cathode erosion.

6.3 Direct Thrust Measuring System

6.3.1 DTMS Overview

To measure the thrust of the μ PPT, one of two measuring techniques can be used, namely the direct thrust measuring system (DTMS) and the indirect thrust measuring system (ITMS). Unlike the ITMS, which mathematically derives the thrust from other variables; the DTMS directly measures the thrust through an experiment. Considering that a DTMS system will be used for this project, the following DTMS methods (seen in Table 6-2) are taken into consideration.

Table 6-2 DTMS design concepts

Concept	Concept Name	Used by
a	Pivoting balance	(Larangot, et al., 2002)
b	Strain gauge cantilever balance	(Lun, 2008)
c	Torsional pendulum	(Seifert, et al., 2013) , (Gamero-Castano & Hruby, n.d.), (Scharlemann, et al., 2011)

The first conceptual design, Figure 6-7 (a), describes a long, thin, rigid arm moving freely around a pivot. The thruster is connected at the other end of the rigid arm creating a ‘swinging arm’ effect. A measuring device is then placed in line with the thruster. Various measuring techniques have been used. These techniques include optics, LVDT and proximity sensors. In the case of Larangot (2002), a permanent magnet was used to create a magnetic inductance field in which a coil was placed. With the rotation of the pendulum, a voltage is generated within the coil which is proportional to the force of rotation; this essentially led to the description of the thrust force. This device is calibrated by small mass loads.

The second conceptual design, Figure 6-7 (b), represents a thin, rigid cantilever beam fixed on one end. When the thruster which is connected to the other end of the beam experience a discharge, a measurable amount of strain will be induced in the beam. This induced strain can then be measured by a strain gauge. This device is calibrated by small mass loads.

The third conceptual design, Figure 6-7 (c), comprises of an equally balanced pendulum rotating about a centre point. This is done by placing the thruster on one end of a thin rigid rod

and placing a counterweight on the other. This allows for a balanced system about the centre of the rod. Thereafter, a torsion wire is placed in the centre of the rod, about which the pendulum can rotate. When a rotational force is generated with a thruster discharge, a certain degree of rotation will be achieved. This rotation angle is dictated by the amount of rotation resistance caused by the torsion constant of the wire. Once the degree of rotation is known, calculations can be made on the force required to achieve that amount of rotation. Calibration of this device can be done electrostatically (Lun, 2008) or by defining the oscillation period.

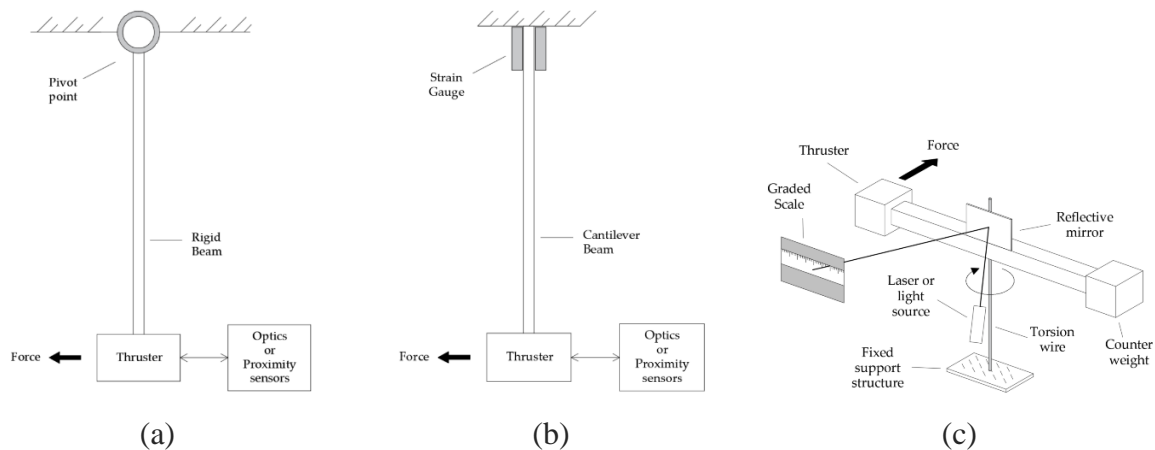


Figure 6-7 DTMS design concepts. Concept (a) represents a pivoting balance. Concept (b) represents a strain gauge cantilever balance. Concept (c) represents a torsional pendulum.

Although the pivot (Figure 6-7-(a)) and cantilever (Figure 6-7-(b)) balance systems seem fairly similar, the pivot balance has the disadvantage of slower response times towards short pulses and therefore is more suited for constant discharge systems. The cantilever balance consists of a rigid body. Therefore, it can easily be used to determine single discharge pulses, although mechanical wear is to be expected in the form of strain hardening (Lun, 2008). Due to the simplicity of a torsion pendulum, it can be designed using everyday household items. As no complex components are required, the cost and build time is dramatically decreased. Furthermore, the torsion pendulum can be approached via two methods, namely:

- Using a low friction bearing
- By using a torsion wire

The first method comprises of a pendulum resting on a low friction bearing, where the thrust is determined by considering rotation time. The problem with this design is finding a bearing with the low resistance requirements that can still accommodate the axial loads applied to it. The second method comprises of a pendulum hanging from a torsion wire. When the torsional resistance of the rotating wire matches the torque applied, the force can be determined. The

weakness of this design lies in the determination of the ‘torsional constant’ of the wire. As shown in equation (6-1), the torsional constant is related to the oscillation period of the system. Therefore, time measurements have to be made. If the time per oscillation is not precise, errors in the thrust calculation can be expected.

$$T_{\text{oscillation}} = 2\pi \sqrt{\frac{I_{\text{inertia}}}{K}} \quad (6-1)$$

where $T_{\text{oscillation}}$, I_{inertia} and K represents the oscillation time of the pendulum, the moment of inertia of the pendulum body and the torsional constant of the wire, respectively. To measure the angle of rotation, a protractor can be used. This method may alter the accuracy of the results. To gather more accurate results, a mirror is placed on top and parallel to the rigid body. From this, a laser is aimed at the mirror perpendicularly. When rotation of the pendulum is observed due to the applied force of the thruster, the change of angle can be measured by how much the laser point shifts on a graded scale. Due to the simplicity of designing a torsional pendulum, component availability, and the ease of theoretical modelling, the torsional pendulum design was chosen for this project.

6.3.2 Preliminary Design of DTMS

For the torsional thrust balance used in this project, an adapted version of the Cavendish gravity experiment was used. As the Cavendish experiment (Figure 6-8) was originally described as ‘Weighing the Earth’ by measuring the force between two objects, the experiment inherently determined the gravitational constant of Newton's law of gravitation. The experiment works by joining two equal masses with a thin, rigid beam. The rod and mass combination is suspended from above using a thin torsion wire attached at the centre of the rod as shown in Figure 6-8. By placing two larger free-standing masses a distance from each smaller mass, a gravitational force exists between them. Knowing that the thin wire has a torsional resistance, the force between the two objects can be calculated when the torsion force of the wire is equal to the gravitational force between the two masses.

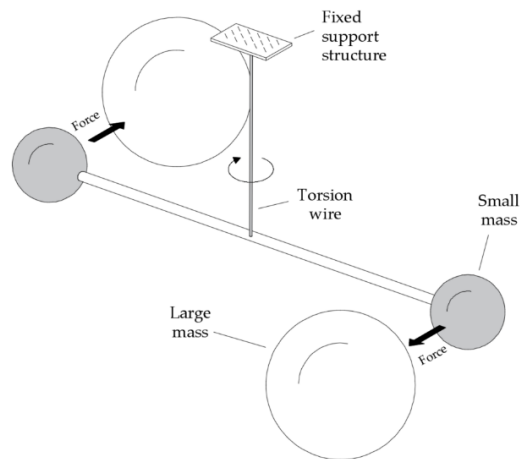


Figure 6-8 Cavendish experiment illustration

By using the cavendish experimental concept, the force generated by the thruster can be determined by modifying the setup to a system that only produces one force vector rotating about a central point. This modification is illustrated in Figure 6-9.

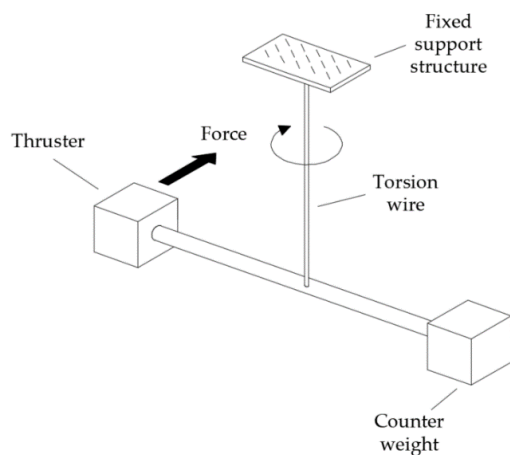


Figure 6-9 Torsion balance concept for a DTMS design (adapted from the cavendish experiment)

Comparing Figure 6-9 with Figure 6-8, similarity in structure can be observed. The major difference between the cavendish experiment and Figure 6-9 is that the rotational force generated in the system is represented by a single force element from the thruster, instead of the two larger masses attracting the two smaller masses in the original experiment.

Therefore, the following simplifications and assumptions are made:

- The system will operate in a low vacuum environment
- Air resistance can be neglected
- The PPT thrust will be the only external force applied to the system

- Mass ejected from thruster is to be neglected
- The force applied from PPT is perpendicular to the rigid rod ($\mathbf{F}_{\text{PPT}} \perp L_{\text{rod}}$)
- The mass of the PPT and counter-weight are equal ($m_{\text{PPT}} = m_{\text{counter}}$)

To determine the thrust generated by the thruster, the rotation angle of the pendulum needs to be measured (as in the cavendish experiment). By measuring the angle at which the pendulum resisting force is equal to the applied force and knowing the torsional constant, the thrust can be determined. To mathematically describe this torsion balancing system, the torques are set equal, shown as,

$$\tau_{\text{wire}} = \tau_{\text{PPT}} \quad (6-2)$$

where, τ_{wire} and τ_{PPT} represents the reaction of the torque generated by the wire due to its torsional constant and the torque generated by the thruster on the pendulum. Describing these torques by their fundamental characteristics, states,

$$\tau_{\text{PPT}} = F_{\text{PPT}} \cdot R_{\text{rod}} \cdot \sin \alpha \quad (6-3)$$

$$\tau_{\text{wire}} = K\theta \quad (6-4)$$

where, F_{PPT} , R_{rod} , α , K and θ represent the force generated by the thruster, the radius of the rigid rod, the angle between the force of the PPT and the rod, the torsional constant and the angle of rotation of the pendulum. From equation (6-2) and the force generated from the PPT being perpendicular to the length of the rod ($\mathbf{F}_{\text{PPT}} \perp L_{\text{rod}}$), equation (6-3) can be represented as,

$$K\theta = F_{\text{PPT}} \cdot R_{\text{rod}} \quad (6-5)$$

From equation (6-1), it is shown that the period of oscillations is directly related to the inertia of the pendulum and the torsional constant of the wire. Therefore, rearranging equation (6-1) to find the torsional constant, yields

$$K = \frac{4\pi^2 I_{\text{inertia}}}{T_{\text{oscillation}}} \quad (6-6)$$

Substituting equation (6-6) back into equation (6-5), leads to

$$\frac{4\pi^2 I_{\text{inertia}} \theta}{T_{\text{oscillation}}} = F_{\text{PPT}} \cdot R_{\text{rod}} \quad (6-7)$$

To determine the inertia of the pendulum, it was decided to evaluate the PPT and counter-weight as point masses while using the parallel-axis theorem to determine the inertia of the rod. Therefore,

$$I_{\text{PPT}} = m_{\text{PPT}} \cdot R_{\text{rod}}^2 \quad (6-8)$$

$$I_{\text{counter}} = m_{\text{counter}} \cdot R_{\text{rod}}^2 \quad (6-9)$$

$$I_{\text{rod}} = \frac{1}{12} m_{\text{rod}} \cdot L_{\text{rod}}^2 \quad (6-10)$$

where I_{PPT} , I_{counter} , I_{rod} , m_{PPT} , m_{counter} , m_{rod} and L_{rod} represents the inertia on the system due to the PPT mass, inertia on the system due to the counter-weight mass, inertia on the system due to the rod mass, the mass of the PPT, the mass of the counter-weight, the mass of the rod, and finally the length of the rod. Determining the total inertia of the pendulum leads to,

$$\sum I_{\text{inertia}} = I_{\text{PPT}} + I_{\text{counter}} + I_{\text{rod}} \quad (6-11)$$

Since $m_{\text{PPT}} = m_{\text{counter}}$, equation (6-8),(6-9) and (6-10) is substituted into equation (6-11), yielding,

$$\sum I_{\text{inertia}} = R_{\text{rod}}^2 \left(\frac{1}{3} m_{\text{rod}} + 2m_{\text{PPT}} \right) \quad (6-12)$$

Introducing equation (6-12) back into equation (6-7) and setting the force as the subject of the formula, the force of the PPT is represented by,

$$F_{\text{PPT}} = \frac{4\pi^2 \left(R_{\text{rod}} \left(\frac{1}{3} m_{\text{rod}} + 2m_{\text{PPT}} \right) \right) \theta}{T_{\text{oscillation}}^2} \quad (6-13)$$

As all variables on the right-hand side (RHS) of equation (6-13) are known, except for the angle of rotation; practical measurements of the pendulum rotation can be used to determine the thrust of the PPT. To simplify the mathematical calculations when conducting numerous tests, a MATLAB® program was written along with an application interface (Figure 6-10) to easily display the generated force of the PPT.

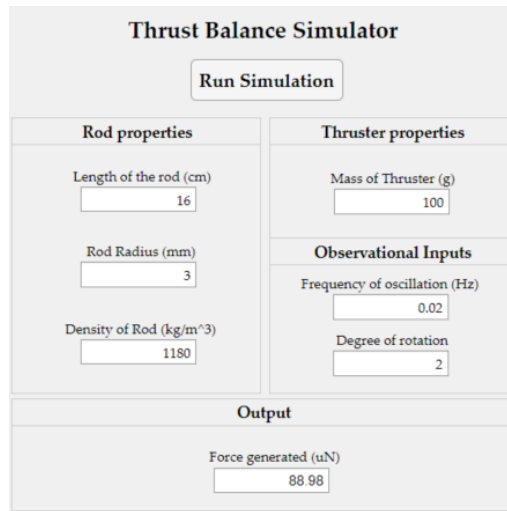


Figure 6-10 Thrust balance GUI interface

Testing the GUI software with the input parameters found in Figure 6-3, it was determined that a thrust of 88.98 μN is generated by the PPT for a pendulum rotation of 2° .

Table 6-3 Input parameters for thrust balance testing

Parameter	Value
Thruster mass	100 g
Rod length	16 cm
Rod diameter	6 mm
Rod density	1180 kg/m ³
Oscillation frequency	0.02 Hz

From the method described above, it is thereby theoretically possible to determine the thrust of the PPT using this torsion pendulum method.

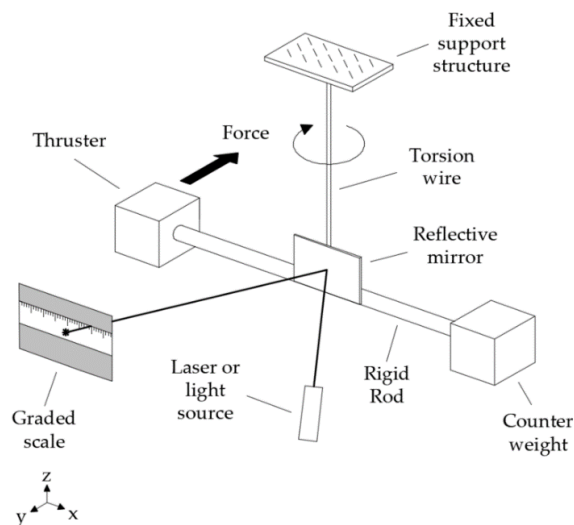


Figure 6-11 Preliminary DTMS design concept

From the design concept seen in Figure 6-11, the torsion pendulum preliminary design consists of a 160 mm rigid plexiglass rod with a diameter of 6 mm and density of 1180 kg/m^3 . The μPPT , weighing 97 g, is mounted on one side of the rod with the thruster's centre of mass at the end of the rod. Similarly, a counterweight (of also 97g) is placed on the other side of the rod with its centre of mass matching the end of the rod. To suspend the pendulum in the air, a 0.1 mm fishline with a length of 40 mm is used to connect the pendulum to the supporting structure. To determine the pendulum's angle of rotation, a mirror is placed in parallel with the rigid rod and on top of the connecting pin. A laser is thereafter directed to the mirror at an angle of 10° to the y-axis (Figure 6-11) and reflected to a graded scale. As the distance on the graded scale is proportional to the angle of rotation, and the angle of rotation represents the force generated by the μPPT , the thrust can be determined. To summarise the DTMS preliminary design, a visual schematic is presented in Figure 6-12.

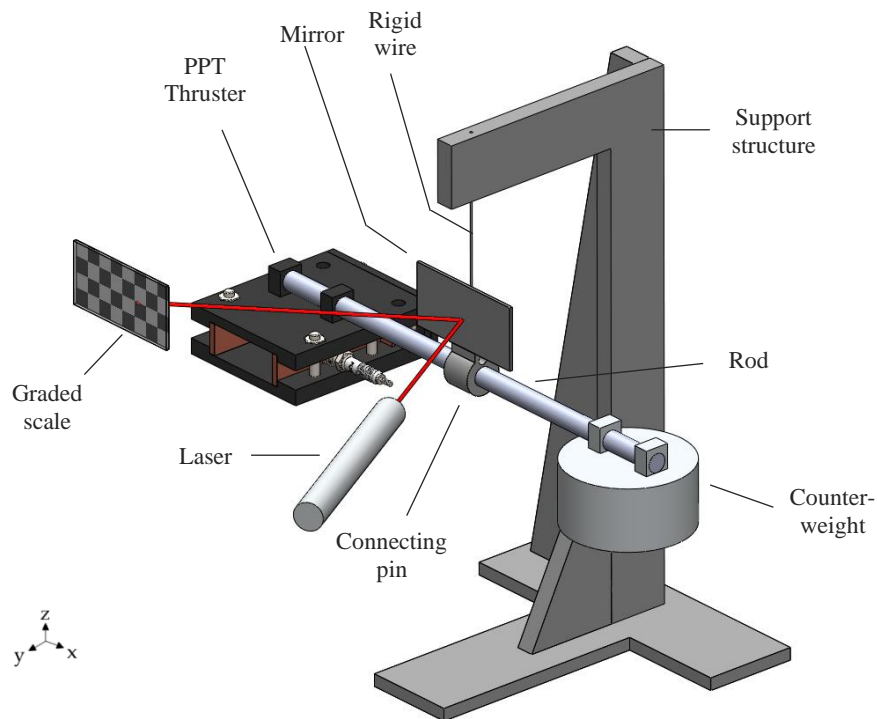


Figure 6-12 Schematic of preliminary DTMS design

6.3.3 Final DTMS Artifact

Due to the physical constraints of using a small vacuum chamber, the measurement setup was modified from the preliminary design as shown in Figure 6-14. The μ PPT was taken off the pendulum and mounted separately. On each end of the rod, a metal foil sheet was attached. The ejected plasma from the PPT strikes one of the foil sheets causing the pendulum to rotate. The rotation of the pendulum is measured using the deflection of the beam onto a graded scale. To elaborate on the modifications two design changes are discussed.

The first design change involved the removal of the thruster directly from the pendulum and placing it and a fixed mount as shown in Figure 6-14. This was due to the complexity of accommodating the wires connected to the μ PPT and interfering with the sensitive rotation of the thruster. Furthermore, with the μ PPT and counterweight both connected directly to the pendulum, the inertia of the system only allowed for small rotation angles. This inherently decreased the system accuracy as a small deflection represents a large spectrum of thrust values. Therefore, the μ PPT and counterweight were replaced with a foil sheet with a defined weight and size. Using the exhaust of the PPT (directed towards the foil sheet), rotation of the thrust balance is obtained.

The second design change involved the positioning of the laser and graded scale. With restricted space within the vacuum chamber, the laser offset toward the mirror resulted in measurement failures as shown in Figure 6-13.

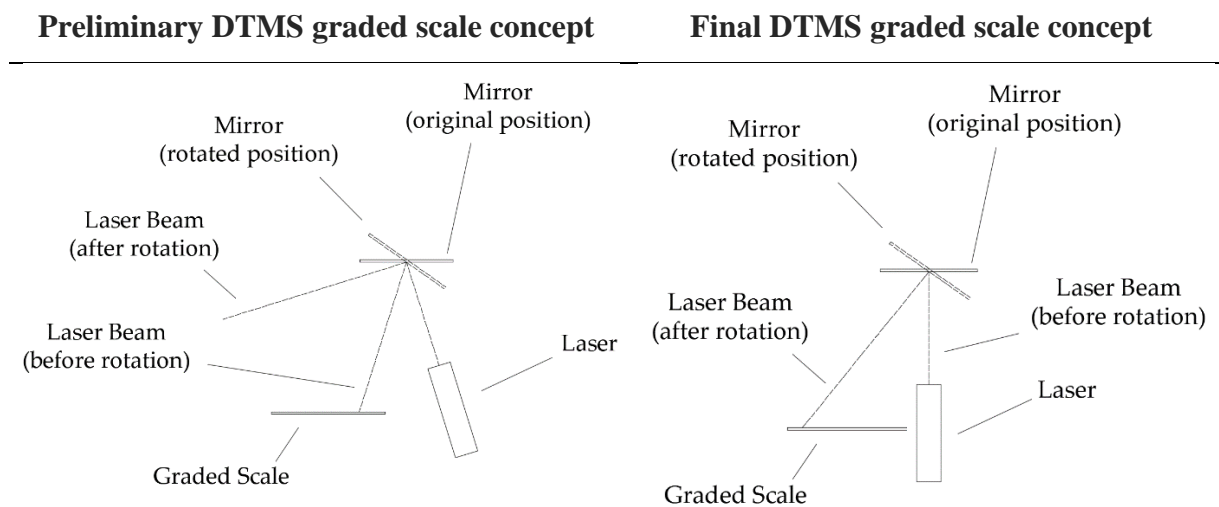


Figure 6-13 Schematic of preliminary DTMS design

This was due to the laser beam reflecting past the area of measurement once rotation of the pendulum occurs. To accommodate for the wide angle of deflection, the laser was moved perpendicular to the mirror while in the resting state as shown in Figure 6-13 and Figure 6-19.

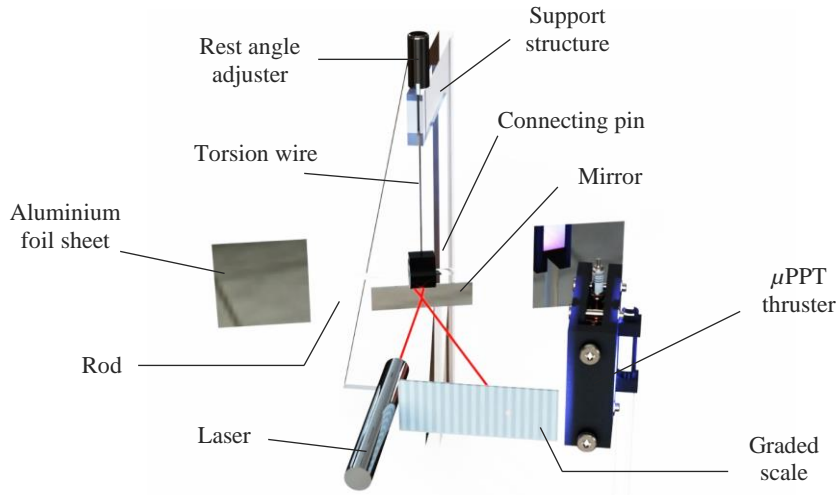


Figure 6-14 Final DTMS design layout

To support the pendulum, the fishline was replaced with a copper wire. This was primarily done to enforce a sense of control over the pendulum position. Therefore, a rest position adjuster was inserted to adjust the pendulum angle's rest position. Re-evaluating the force determination equation (equation (6-13)) from section 6.3.2, it can be stated that the equation is incomplete when comparing it to the practical experimental design. This is due to the lack of accounting for the connector pin and mirror within the system shown in Figure 6-14. As the inertia of the system is affected by these additional components, we redefine the total system inertia as

$$I_{\text{foil}} = m_{\text{foil}} \cdot R_{\text{rod}}^2 \quad (6-14)$$

$$I_{\text{mir}} = \frac{1}{12} m_{\text{mir}} (a_{\text{mir}}^2 + b_{\text{mir}}^2) \quad (6-15)$$

$$I_{\text{con}} = \frac{1}{12} m_{\text{con}} (a_{\text{con}}^2 + b_{\text{con}}^2) \quad (6-16)$$

$$I_{\text{rod}} = \frac{1}{12} m_{\text{rod}} \cdot L_{\text{rod}}^2 \quad (6-17)$$

Using the same methodology applied within the preliminary design section (chapter 6.3.2), and stating that the total inertial is the sum of all individual inertia's,

$$\sum I_{\text{inertia}} = I_{\text{foil}} + I_{\text{mir}} + I_{\text{con}} + I_{\text{rod}} \quad (6-18)$$

the force of the μ PPT can now be determined by

$$F_{\text{PPT}} = \frac{4\pi^2\theta}{T_{\text{oscillation}}^2} \left[R_{\text{rod}} \left(\frac{1}{3}m_{\text{rod}} + 2m_{\text{foil}} \right) + \frac{m_{\text{con}}(a_{\text{con}}^2 + b_{\text{con}}^2) + m_{\text{mir}}(a_{\text{mir}}^2 + b_{\text{mir}}^2)}{12} \right] \quad (6-19)$$

where m_{con} , a_{con} , b_{con} , m_{mir} , a_{mir} , b_{mir} and m_{foil} represents, the mass of the connecting pin, the width of the connecting pin, the length of the connecting pin, the mass of the mirror, the width of the mirror, the length of the mirror and the mass of the foil sheet. For a clear definition of the additional variables used in equation (6-19), we say

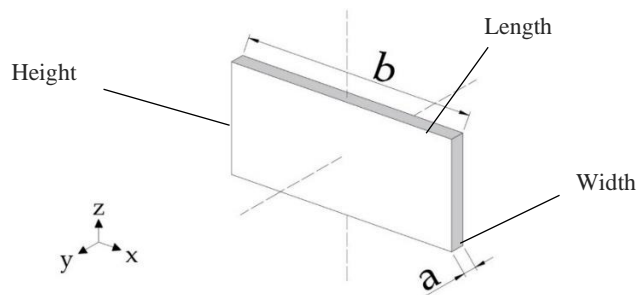


Figure 6-15 Description of inertia variables

From the final design seen in Figure 6-14, the torsion pendulum consists of a 160 mm rigid, brass rod with a diameter of 2 mm and density of 8400 kg/m^3 . A thin piece of foil (35x35 mm), weighing 0.3 g is mounted on both sides of the rod with its centre of mass at the end of the rod. To suspend the pendulum, a 0.1 mm copper wire of 40 mm is used to connect the pendulum to the supporting structure. After numerous tests (discussed in section 6.3.4), it was found that the natural frequency of the system averaged 0.4992 Hz, resulting in a period of approximately 2 seconds per oscillation. To determine the pendulum's angle of rotation, a mirror is placed parallel to the rigid bar. The mirror is supported by a 3D printed connecting pin. The laser is thereafter directed perpendicular to the mirror. Once the discharge is initiated, the rotation of the pendulum will cause the laser beam to be reflected by the mirror onto the graded scale. As the distance on the graded scale is proportional to the angle of rotation, it was found that the angle of rotation is represented by equation (6-20) which is further discussed in the subsequent section.

$$\phi = \tan^{-1} \left(\frac{x^* + 9}{73.5} \right) \quad (6-20)$$

6.3.4 Calibration of DTMS

To calibrate the thrust balance, the oscillatory behaviour of the pendulum was investigated. From equation (6-1), it is shown that the torsional constant can be determined with a known oscillation period and system inertia. Therefore, rearranging equation (6-1) leads to,

$$K = \frac{4\pi^2 I_{\text{inertia}}}{T_{\text{oscillation}}^2} \quad (6-6)$$

The dynamics of the rotational pendulum is essentially that of a damped second-order system. A typical step response of this system is shown in Figure 6-16. It is expected to find the rotation angle of the pendulum to decrease over time. Although the amplitude of the oscillation is expected to decrease, it is important to notice that the oscillation period is theoretically unchanged.

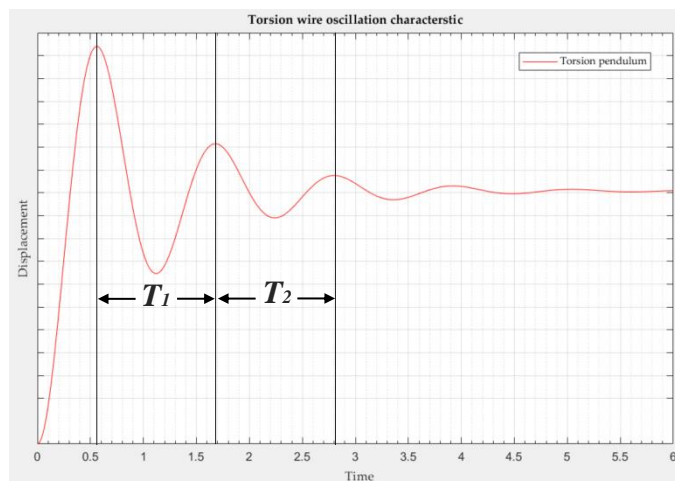


Figure 6-16 general torsional balance oscillation characteristic⁶

Therefore, the torsional pendulum was initially manually rotated and released to oscillate freely. The oscillation period was measured using time lapses through a digital stopwatch. This experiment was repeated three times, whereafter successive tests were done by evaluating the oscillation of the thruster after μ PPT discharge.

⁶ It should be noted that the displacement on the vertical axis observed in Figure 6-16 is proportional to the angular displacement of the torsional pendulum

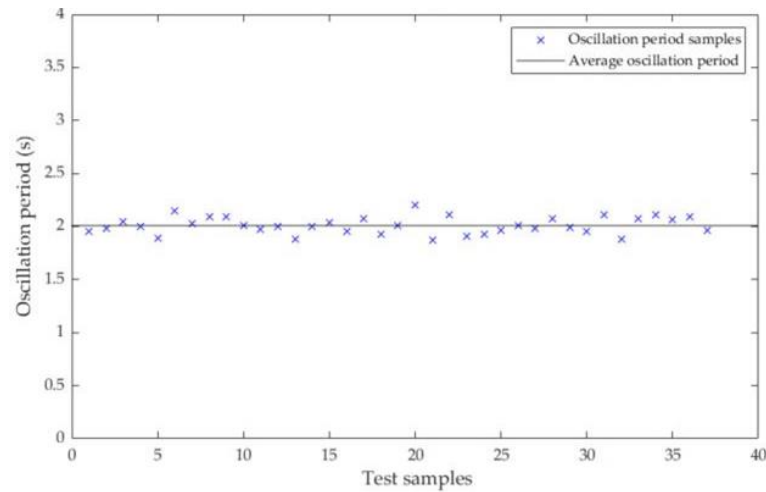


Figure 6-17 Thrust balance oscillation period measured data

When evaluating the sample measurements in Figure 6-17, it can be observed that there are irregularities within the data samples. These irregularities can be described by two factors, namely:

- Human error
- Externally applied forces

As previously mentioned in this chapter, a digital stopwatch and human reaction time was used to measure the oscillation period of the pendulum. When considering this measuring method, irregularities are to be expected. Furthermore, it should be noted that initial oscillation testing was conducted in open air. Thus, it should be considered that air currents could affect the oscillation time of the pendulum. From the data captured in Figure 6-17, it was calculated that the mean oscillation period equalled 2.0033 s or 0.4992 Hz.

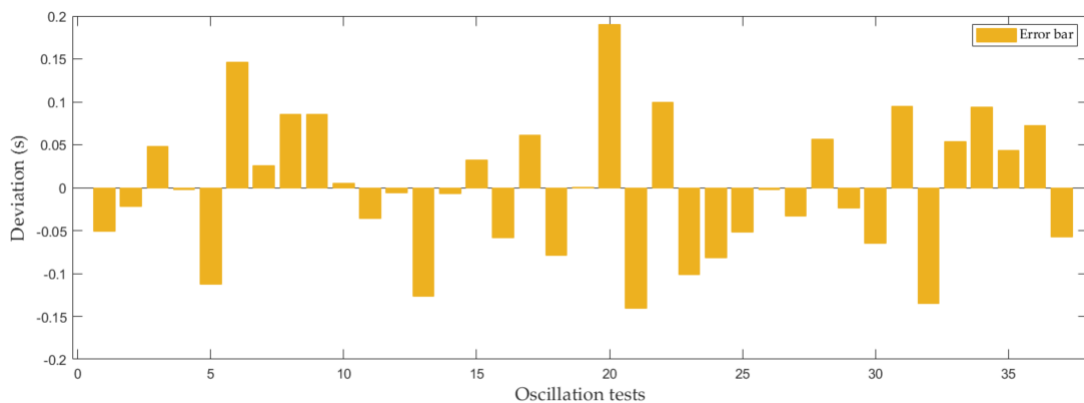


Figure 6-18 Thrust balance oscillation error bars

Analysing the error bar graph presented in Figure 6-18, a standard deviation of 0.4803 is calculated. When considering the standard deviation, thrust calculations led to a system error of approximately 20%.

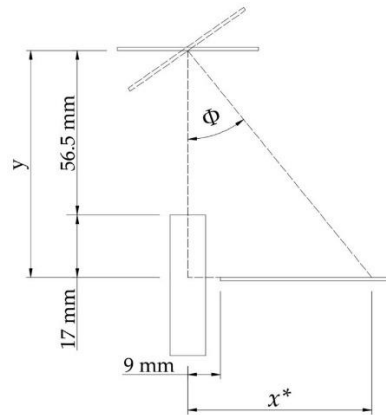


Figure 6-19 Torsion pendulum rotation using a graded scale

The rotation angle of the pendulum is measured using a graded scale. Therefore, a laser is pointed directly towards the pendulum mirror so that the mirror and laser beam are perpendicular to one another. From physical measurements, it was found that the laser was 56.5 mm from the mirror and the graded scale was 17 mm behind and on the right-hand side of the laser as shown in Figure 6-19. Furthermore, a 9 mm offset was measured between the laser and the graded scale. Using trigonometry functions, the angle of rotation (ϕ) can be determined by,

$$\phi = \tan^{-1} \left(\frac{x}{y} \right) \quad (6-21)$$

where $x = (x^* + 9)$, x^* and y represents the adjusted deflection distance, the measured distance on the graded scale, and the perpendicular distance between the mirror and graded scale, respectively.

6.3.5 Summary of DTMS

Within this section, a direct thrust measuring system was developed to measure the thrust generated by the μ PPT. Three thrust balance concepts were considered, namely, a pivot balance, strain gauge and torsion balance. From the three concepts discussed, it was decided to move forward with the torsion balance for this project due to the simplicity of design with no complex components required. This is also due to the slow response time of the pivot balance and the mechanical wear of the strain gauge. To summarise the DTMS design iterations, Table 6-4 is presented.

Table 6-4 DTMS design iterations

Design	Design description and changes
Conceptual designs	Three thrust measuring techniques are evaluated, namely: pivoting balance, strain gauge cantilever balance and torsional balance. Due to simplicity, further investigation steered towards the torsion balance. (Found in chapter 6.3.1)
Preliminary design	The thruster is mounted onto the pendulum; therefore, a counterweight is required. Fishline is used to support the 6 mm plexiglass rod, while the laser is positioned at a 10° angle from the front face of the mirror. (Found in chapter 6.3.2)
Final experimental Artifact	Thruster and counterweight are removed from the pendulum and replaced with thin 35x35 mm foil sleeves. Instead, the thruster is positioned perpendicular to the foil surface, where the exhaust particles produce rotation of the pendulum. Furthermore, the laser position is moved perpendicular to the mirror. This change in position allows for an increase in the rotational angle. (Found in chapter 6.3.3)

The final experimental thrust balance consists of a plexiglass support structure, copper torsion wire, a brass rod with a foil sheet mounted at each end, a mirror placed on the pendulum, a laser pointed perpendicular to the mirror when in resting state and a graded scale.

6.4 Summary and Conclusion

Within this section, all experimental work relating to the pulsed plasma thruster was discussed. This includes three main topics of discussion, namely: The experimental test setup, the experimental testing approach, and the DTMS system designed for this project.

Within the experimental test setup, a clear description of the components inside and outside of the vacuum chamber was presented. Thereafter, the experimental electrical circuit was presented, which was followed by a visual representation of how the measuring equipment was integrated into the electrical system.

Within the experimental testing approach, four types of tests were discussed as well as the importance of each. These tests are the voltage discharge measurements, current discharge measurements, thrust measurements and variable electrode length tests. Furthermore, these experimental tests were conducted to gather an understanding of pulsed plasma thrusters.

Within the DTMS section, a self-made thrust balance was designed, developed, and tested. Therefore, a detailed description was presented of the conceptual, preliminary, and final work on a DTMS prototype.

Chapter 7

Experimental Results and Discussion

In this chapter, all of the experimental test results are presented. This includes experimental test results for experiment 1 and experiment 2. Therefore, throughout this chapter, the performance of both experiments is displayed, analysed, and discussed. To present the thruster performance parameters, a similar sequential order is followed as in chapter 6.2. Thus, voltage and current discharges are firstly presented in a logical and meaningful fashion. From the voltage and current discharges, system characteristics are identified. From the voltage discharge measurements, the following system characteristics can be determined: the system resistance, system response and the damped harmonic motion. From the current discharge measurements, the peak current and plasma resistance are identified. Thereafter, plasma temperatures are theoretically calculated and compared to the literature of Nada(2013). A self-made thrust balance, described in section 6.3 of chapter 6, is used to measure the thrust of the μ PPT. Throughout this chapter, both experiment 1 and experiment 2 are subjected to variable operating conditions. These variable conditions include fluctuations in initial discharge voltage and operating background pressure. For the initial voltage fluctuations, voltages varied from 750 V to 1200 V, while pressure settings ranged between 0.75 Torr and 18 Torr. To end the chapter, a summary is presented. Due to measures beyond our control, physical experiments for this thesis were constrained in multiple areas. For this reason, this chapter presents an experimental limitations table (Table 7-1), essentially describing the experimental conditions under which the thruster was tested.

7.1 Experimental Limitations

Table 7-1 Experimental limitations

Limitations	Description
Current measurement	<p>Generally, a Rogowski coil, Hall sensor or fluxgate is used for current measurements in pulsed plasma thrusters. Examples of the Rogowski coil application can be found in the literature by (Choueiri, 2008), (Scharlemann, et al., 2011) and (Pottinger & Scharlemann, 2007). As none of these devices was available for this work, a 50 mV 80A shunt resistor was used.</p> <p>Queries: Limited literature exists on the shunt resistor properties. Therefore, there is uncertainty about how it operates over the maximum voltage range and how it responds to transient analysis.</p>
Voltage measurement	<p>Due to the operating voltage of the μPPT, high accuracy, high voltage probes are required. Due to the lack of equipment, initial compensation led to the design of a voltage divider. After inadequate testing results, a high voltage attenuator (Tektronix P5205) replaced the voltage divider. Without the possibility of manual calibration, Figure 7-6 displays the inaccuracy of the voltage attenuator when measuring a 5V square pulse waveform within the general discharge time of the thruster.</p>
Vacuum chamber	<p>To measure the performance of the thruster at LEO altitudes, a vacuum chamber of 10^{-4} to 10^{-10} Torr is required. Due to availability, a chamber of only 0.75 Torr vacuum pressure was used.</p>
Thrust measurement	<p>A high precision thrust balance is required to measure the thrust of the μPPT. As no thrust balance was available at the time, a self-made thrust balance was developed. Due to the high precision calibration equipment necessary and considering a self-made thrust balance was developed, errors were expected.</p>
Mass measurement	<p>An ultra-sensitive weight measuring device is required to measure the propellant block after a thruster discharge. As the mass ablated per shot was estimated to be around 2.85e-08 kg, the 0.01g sensitive scale proved impractical to accurately determine the mass per shot. For this reason, the estimated mass of 2.85e-08 kg was kept constant, while the measuring scale was used to characterise the thrust balance.</p>
Plasma density and temperature measurement	<p>When measuring plasma density, techniques such as Herriot cell interferometry can be applied. Detailed descriptions of this method can be found in research by (Berkery, et al., 2007). Similarly, spectroscopy techniques can be applied to evaluate plasma temperature. Due to the imaging lenses, filters, CCD detectors and lasers required, no plasma interferometry was conducted at this time.</p>
Flight circuit board creation	<p>Due to the mechanical nature of this work, complex electronics are not covered and, therefore, are proposed for future work and discussed in Appendix E.</p>

7.2 Experimental Results: Parameter Analysis

For all testing within this section, Table 7-2 represents the physical μ PPT parameters used. To test the thruster, three critical factors were examined, namely: the voltage discharge, current discharge, and thrust. These three variables determine the performance of the thruster and, therefore, associated comparisons were made by fluctuating the initial voltage, pressure, and changing the electrode length.

Table 7-2 Experimental design parameters

Operation Parameters	Values
Capacitance	6 μ F
Initial Voltage	750V - 1200 V
Main discharge energy	1.68 J - 4.32 J
Electrode separation distance	25 mm
Electrode width	10 mm
Electrode thickness	2 mm
Electrode Length	25 mm and 40 mm
Operating pressure	0.75 Torr - 18.75 Torr (1 mbar to 25 mbar)

Initially, tests were conducted using a self-made voltage divider. Results of the experimental tests quickly led to the decision to discard this unit since a large amount of additional resistance was added to the circuit.

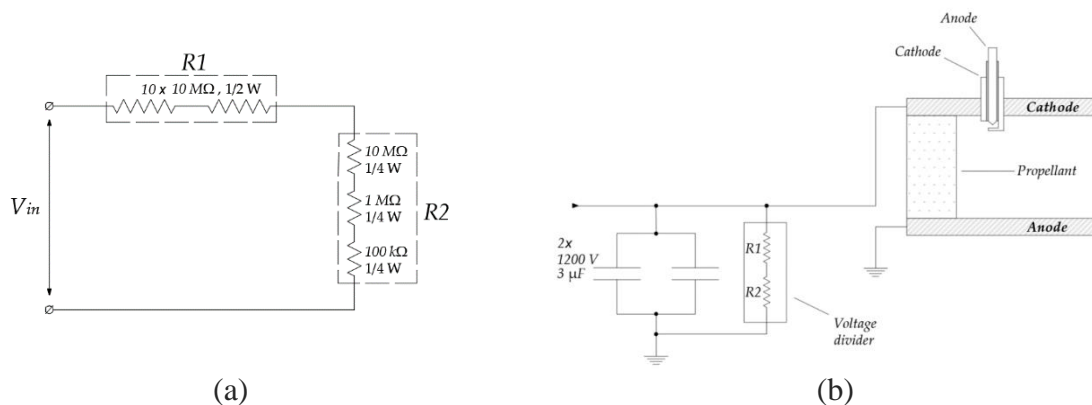


Figure 7-1 Voltage divider used for initial testing. Figure (a) presents constructed voltage divider values. Figure (b) presents the implementation of the voltage divider into the experimental prototype circuit.

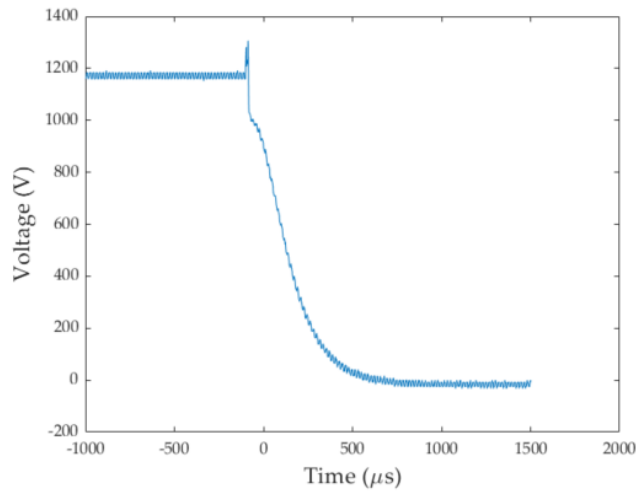


Figure 7-2 Voltage over time curve of the experimental prototype using the voltage divider from Figure 7-1. The curve describes the high resistance and highly over-damped system.

As mentioned in chapter 6, all voltage discharges further discussed within this chapter are measured with a Tektronix P5205 500x voltage attenuator.

7.2.1 Voltage Discharge Measurements

For the first voltage discharge measurements, the experimental design was tested within a 0.75 Torr pressure environment. Throughout the test phase, two separate electrode lengths were tested, namely: a 40mm length electrode (Experiment 1) and a 25 mm length electrode (Experiment 2).

Table 7-3 Initial voltage discharge for Experiment 1 and Experiment 2

40 mm Electrode		25 mm Electrode	
Experiment 1	Initial Voltage	Experiment 2	Initial Voltage
Test 1	1180 V ± 1.11%	Test 1	1180 V ± 0.55%
Test 2	1190 V ± 1.68%	Test 2	1185 V ± 1.27%
Test 3	1180 V ± 1.11%	Test 3	1200 V ± 0.83%
Test 4	1190V ± 1.68%	Test 4	1170 V ± 1.29%
Test 5	1200 ± 1.69%	Test 5	1180 V ± 0.55%
Test 6	1200 ± 1.69%	Test 6	1200 V ± 0.84%

As the experimental setup discussed in section 6.1 consisted of manual switches combined with low-quality capacitors, maintaining the desired voltage with a high level of accuracy proved troublesome. The use of manual switches led to a sequence of events (found in Figure 5-13) that had to be executed in a short amount of time, essentially resulting in discharge voltage

inconsistencies. Table 7-3 provides a list of tests conducted on both electrodes showing the variation of the initial discharge voltages. The initial voltage varied between 1170 V to 1200V. Figure 7-3 and Figure 7-4 show plots of the capacitor voltages as a function of time for the test listed in Table 7-3.

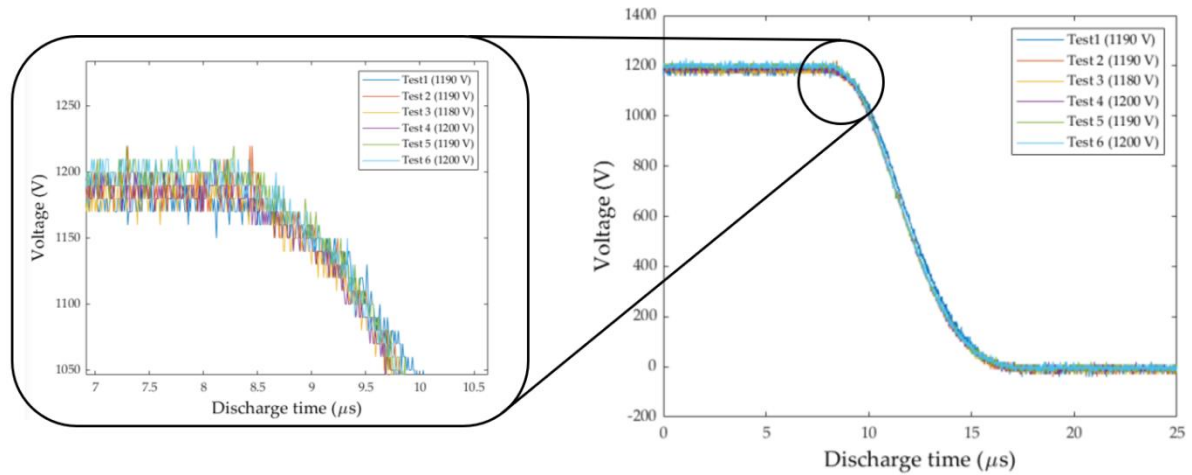


Figure 7-3 Raw voltage over time data from oscilloscope when six 40 mm electrode tests (Experiment 1) discharged between 1180 V and 1200 V at 0.75 Torr.

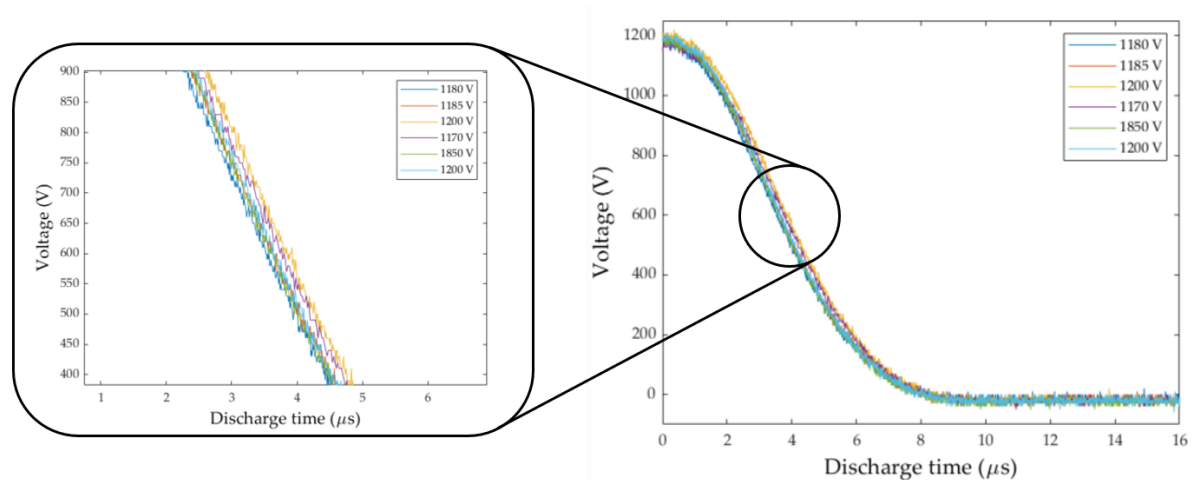


Figure 7-4 Raw voltage over time data from oscilloscope when six 25 mm electrode tests (Experiment 2) discharged between 1170 V and 1200 V at 0.75 Torr.

To compare the voltage discharge curves for both experiment 1 and experiment 2, a Savitzky-Golay⁷ filter was used for Figure 7-3 and Figure 7-4 to smooth out the discharge curves. The filtered data is presented in Figure 7-5. From the filtered data results, it is found that a 40 mm electrode thruster, operating at 1200 V, delivers a discharge pulse of approximately 9.24 μ s.

⁷ A Savitzky-Golay filter is a digital filter that can be used on a set of data point with the purpose to smooth out the data

Similarly, a 25 mm electrode thruster display a discharge time of approximately 10 μs . Additional to the voltage discharge curves, error bars display the standard deviation at four distinctive points within the discharge process, namely: the charged phase, initial discharge phase, mid-discharge phase, and end of discharge phase. These error bars represent the standard deviation of six discharge shots for both the 40 mm and 25 mm electrode thrusters observed in Figure 7-3 and Figure 7-4.

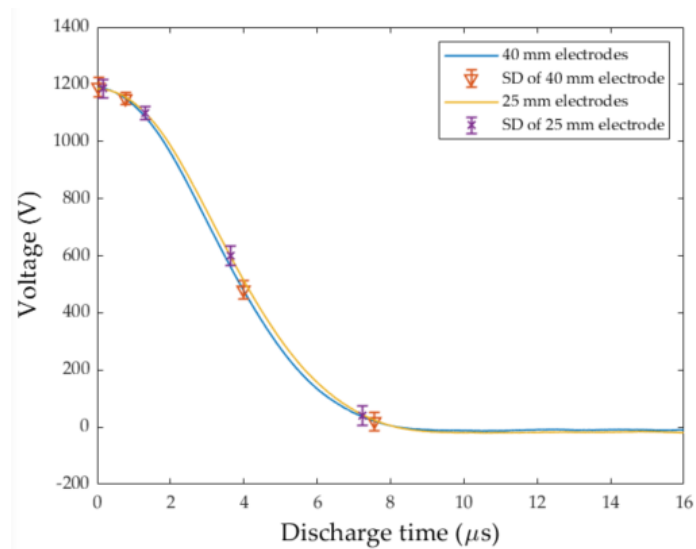


Figure 7-5 Filtered voltage discharge over time data of the experimental prototype for both experiment 1 and experiment 2 when discharging at approximately 1200 V under 0.75 Torr.

To assess the influence of the Tektronix P5205 500x attenuator, a square wave signal was applied to its input and the output was observed. Figure 7-6 shows the output of the attenuator together with the expected waveform obtained without the attenuator. From the results, the following was observed,

- the noisy character of the attenuator output
- the falling edge slope is distorted

This distortion of the falling edge will manifest itself as a resistance when estimating the plasma resistance. Therefore, it will contribute to a larger RC time constant, thus appearing as larger resistance. Furthermore, the high/low peak fluctuations observed in Figure 7-3 and Figure 7-4 are presumably caused by the Tektronix P5205 500x voltage attenuator. While attempting to calibrate the voltage attenuator, the falling edge of the square wave displayed a slope characteristic as shown in Figure 7-6. This slope generally indicates additional resistance and capacitance within the probe setup itself. As the slope stretches throughout the timeframe of discharge measurements (between 0 and 8 μs), the assumption is made that the voltage

attenuator is limited to the measurement accuracy of the discharge curve within the respected timeframe.

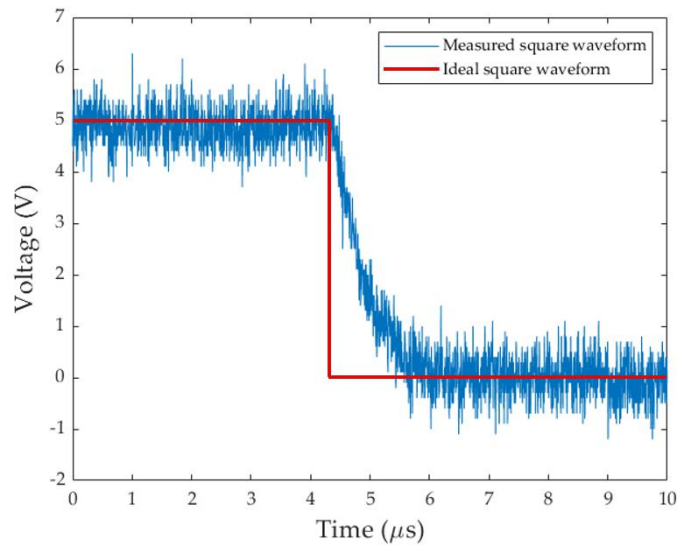


Figure 7-6 Tektronix P5205 slope characteristic when measuring a square pulse waveform.

Furthermore, as shown in Figure 7-3 and Figure 7-4, the discharge times are very similar to each other, although the voltages are different. This is due to the circuit capacitance equation, which controls the discharge time of the circuit, as shown in equation (6-1).

$$V_c = V_0 \left(e^{-t/RC} \right) \quad (6-1)$$

where, V_c , V_0 , t , R , C represent the capacitor voltage, the initial voltage, the discharge time, the total system resistance, and the capacitance of the capacitor respectively. Therefore, with the small number of voltage variations, the discharge time is rarely affected. As the discharge time is also associated with the total circuit resistance, it was determined that the system resistance for the 40 mm electrode thruster is 163.96 mΩ and 179.26 mΩ for the 25 mm electrode thruster.

7.2.2 Current Discharge Measurements

As described in section 6.2 of chapter 6, due to the inability of using a Rogowski coil to measure the discharge current, a 0.624 mΩ shunt resistor was utilized. Following the same methodology as the voltage discharge results from the prior section, the current discharge results of experiment 1 and experiment 2 are presented in Table 7-4 and Figure 7-7 and Figure 7-8.

Table 7-4 Current discharge measurements for both experiment 1 and experiment 2, each consisting of six discharges tested at 0.75 Torr with an initial voltage ranging between 1170 V and 1200 V.

40 mm Electrode			25 mm Electrode		
Experiment 1	Shunt Voltage	Discharge Current	Experiment 2	Shunt Voltage	Discharge Current
Test 1	19.26 V ± 1.79%	30.81 kA ± 1.79%	Test 1	12.7 V ± 2.36%	20.32 kA ± 2.36%
Test 2	20.55 V ± 2.7%	32.89 kA ± 2.7%	Test 2	12.9 V ± 3.88%	20.64 kA ± 3.88%
Test 3	19.3 V ± 1.55%	30.88 kA ± 1.55%	Test 3	13.1 V ± 5.44%	20.96 kA ± 5.44%
Test 4	19.6 V ± 0.86%	31.36 kA ± 0.86%	Test 4	12.4 V ± 5.44%	19.84 kA ± 5.44%
Test 5	20.2 V ± 2.97%	32.32 kA ± 2.97%	Test 5	13.8 V ± 4.54%	22.08 kA ± 4.54%
Test 6	20.3 V ± 3.45%	32.48 kA ± 3.45%	Test 6	14.1 V ± 6.38%	22.56 kA ± 6.38%

Evaluating the discharge times within Figure 7-7, it is found that the discharge time correlates with the voltage discharge times observed in Figure 7-5, essentially describing a high system resistance of 163.96 mΩ and 179.26 mΩ for the 40 mm electrode thruster and the 25 mm electrode thruster respectively.

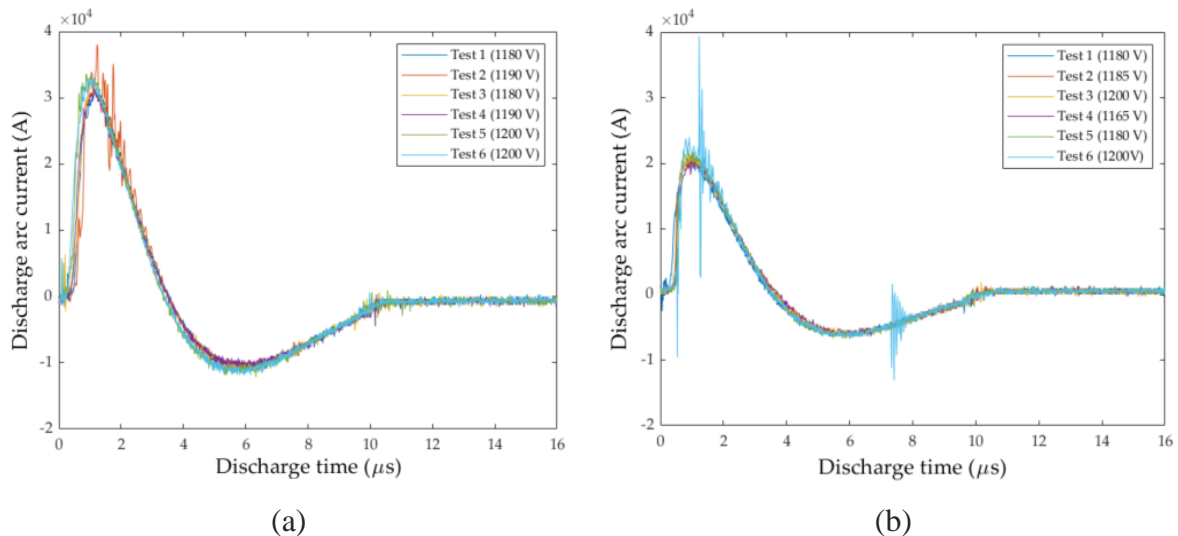


Figure 7-7 Raw current discharge over time data from oscilloscope. For figure (a), six 40 mm electrode tests (Experiment 1) discharged between 1180 V and 1200 V at 0.75 Torr. Similarly, figure (b), represents six 25 mm electrode tests (Experiment 2) discharging between 1170 V and 1200 V at 0.75 Torr.

To compare the current discharge curves for both experiment 1 and experiment 2, a Savitzky-Golay filter was used to smooth out the discharge curves. As each experiment consists of six distinctive shots, the average initial voltage for each test was used, as shown in Table 7-3. To

accommodate the change in discharge current from all six discharges within each experiment, standard deviation points were added to critical areas within the discharge cycle.

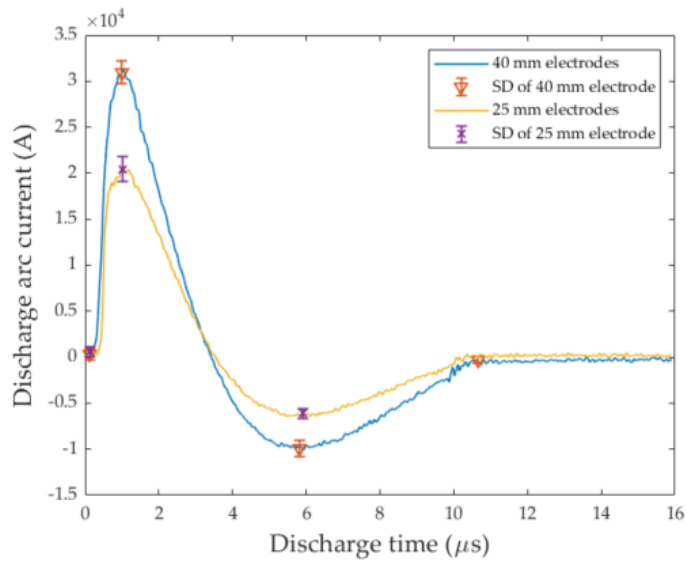


Figure 7-8 Filtered current discharge over time data for both experiment 1 and experiment 2 when discharging at approximately 1200 V under 0.75 Torr.

While evaluating the discharge current for both experiment 1 and experiment 2 in Figure 7-8, a dramatic dissimilarity in peak current values is observed. As the electrode length is the only physical variable changing between these two experiments, initial observations led to the assumption that the shorter electrodes provide a higher discharge resistance. Calculating the plasma arc resistance from the known discharge current when each experiment is discharged at 1200V, yields:

Table 7-5 Plasma resistance for experiments 1 and 2 when discharging at 1200 V

Experiment 1	Voltage	Current	Plasma resistance
Test 3	1200 V	32.32 kA	37.13 mΩ
Test 6	1200 V	32.48 kA	36.95 mΩ
Experiment 2	Voltage	Current	Plasma resistance
Test 5	1200 V	22.4 kA	53.57 mΩ
Test 6	1200 V	22.56 kA	52.748 mΩ

Using Ohms law to determine the plasma resistance from the input voltage and known current, we found that the average plasma resistance for experiment 1 is 37.04 mΩ and that for experiment 2 is 53.159 mΩ. When deducting the plasma resistance from the total resistance determined using equation (6-1), it is found that for both experiment 1 and experiment 2, the system resistance is approximately 126 mΩ.

7.2.3 Estimated plasma temperature

Reintroducing the plasma resistance model from chapter 3.2, it is shown that the plasma resistance relies on the plasma temperature. As the electrode separation distance and electrode width are known while assuming a plasma density of 1×10^{21} , the plasma temperature can be calculated by using the plasma resistance from the previous section.

$$R_p = 8.08 \frac{h_e}{T_e^{\frac{3}{4}} w_e} \sqrt{\frac{\mu_0 \ln \left[1.24 \times 10^7 \left(\frac{T_e^3}{n_e} \right)^{\frac{1}{2}} \right]}{\tau}} \quad (6-2)$$

where R_p , h_e , w_e , μ_0 , n_e and T_e represents the plasma resistance, electrode separation distance, electrode width, permeability of free space, plasma density, and plasma temperature, respectively. Therefore, using the experimental design parameters found in Table 7-2 with the plasma resistance found in Table 7-5, it was found that the plasma temperature is approximately 3.78 eV for experiment 1 and 2.188 eV for experiment 2. To summarize all the parameters associated with equation (6-2), Table 7-6 is presented.

Table 7-6 PPT input parameters and plasma temperature for experiments 1 and 2

Experiment 1: 40 mm Electrode		Experiment 2: 25 mm Electrode	
Parameter	Value	Parameter	Value
Electrode separation distance	25 mm	Electrode separation distance	25 mm
Electrode width	10 mm	Electrode width	10 mm
Plasma density	1×10^{21}	Plasma density	1×10^{21}
Permeability of free space	$4\pi \times 10^{-7}$	Permeability of free space	$4\pi \times 10^{-7}$
Plasma resistance	37.04 mΩ	Plasma resistance	53.159 mΩ
Plasma temperature	~ 3.78 eV	Plasma temperature	~ 2.188 eV

Thereafter, the plasma temperature was determined by using the data from Nada (2013) who provided a graph of various plasma resistances to plasma temperatures when having various aspect ratios. This data can be seen in Figure 7-9. Using this graph together with the experimentally determined plasma resistance, we can find the plasma temperature.

Nada(2013) only provided data for aspect ratios (AR) of 1, 3 and 5. Our AR is 2.5. Therefore, interpolation was required from the data in Figure 7-9 to create a curve for AR=2.5. The result of this interpolation is shown in Figure 7-9. Using the new AR = 2.5 curve line with the plasma resistance found in Table 7-6, it was found that the plasma temperature for experiment 1 is approximately 4.2 eV and 2.7 eV for experiment 2.

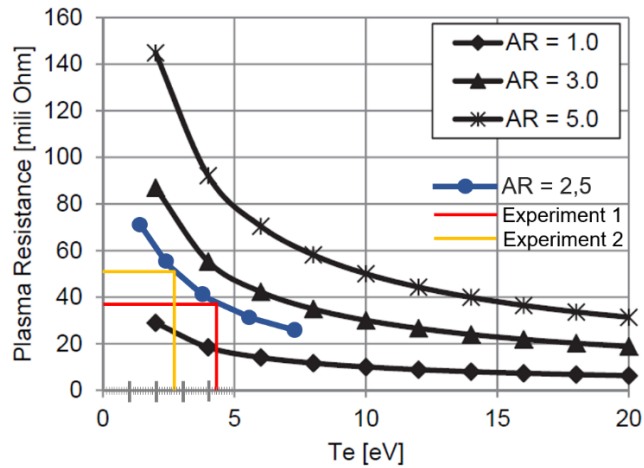


Figure 7-9 Plasma resistance over plasma temperature for dedicated aspect ratios (adapted from (Nada, Semtember, 2013)). The blue dotted line represents the added interpolated aspect ratio of 2.5 found within this thesis to the constructed graph by Nada.

Comparing the plasma temperature for both experiment 1 and experiment 2 with the literature constructed by (Nada, Semtember, 2013) in Figure 7-9, it is observed that the plasma temperatures determined for both experiments are in close proximity to the literature.

Table 7-7 Summary of plasma temperature results

Experiment 1	Value
Calculated plasma temperature	3.78 eV
Plasma temperature using the graph of (Nada, Semtember, 2013)	4.2eV
Similarity	90%
Experiment 2	Value
Calculated plasma temperature	2.188 eV
Plasma temperature using the graph of (Nada, Semtember, 2013)	2.7 eV
Similarity	81%

7.2.4 Thrust Measurements and Thrust Extrapolation to LEO pressures

As the capacitance, electrode separation distance, electrode length, electrode width and electrode thickness remained constant throughout the testing process for both experiments 1 and 2, the initial voltage was found to be the only changing input variable within the μ PPT itself. Therefore, a fair argument can be made that the initial voltage is the primary variable leading to variances in discharge performance. Figure 7-10 shows a plot of the thrust versus discharge energy for experiments 1 and 2. The results display a linear relationship between the increase in voltage and the increase in thrust. Furthermore, it appears that the specific thrust (T_F/W) increases as the operating pressure increases. From these tests, it is found that a maximum thrust of 3.374 mN is observed for a 1200 V discharge operating at 0.75 Torr (1 mbar). From these results, the standard deviation was calculated to be 0.7054. Furthermore, it was found that a dramatic increase in thrust occurs when the pressure is increased during μ PPT discharges. When testing the thruster at a pressure of 18 Torr (25 mbar), a thrust of 4.298 mN is shown in the subsequent figure, leading to a 27.4% increase in thrust when compared to the 0.75 Torr pressure environments.

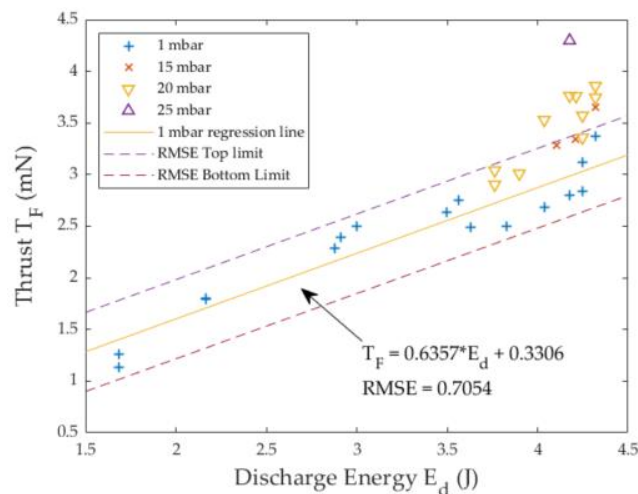


Figure 7-10 Thrust to discharge energy evaluation at various pressure levels ($C = 6 \mu\text{F}$)

Due to the limitation of operating pressure throughout these experimental tests, three identical discharge energy samples, operating at various pressures, were used to roughly estimate thrust at the desired pressure of Low Earth Orbit (LEO). From the extrapolation results toward LEO pressures (1×10^{-9} Torr to 7.5×10^{-10} Torr), a rough estimation led to a thrust generation of approximately $270 \mu\text{N}$.

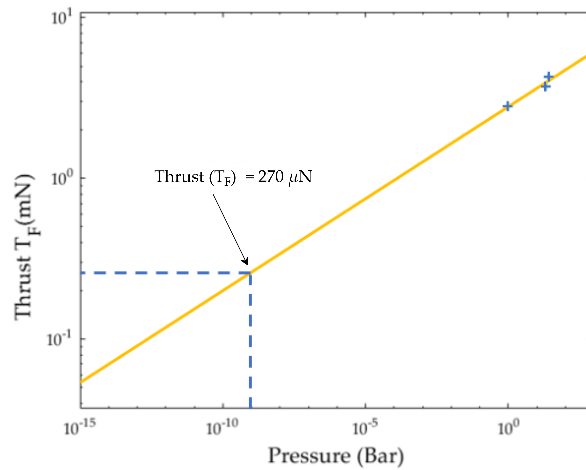


Figure 7-11 Thrust extrapolation towards LEO pressure discharging at 1200 V

Comparing the measured experimental thrust to the numerical results presented in chapter 5.3, it is clear that the thrust exceeds that of the simulation with a ratio of approximately 20:1. Comparing the extrapolated results to the numerical simulation, a 61% similarity is obtained.

Table 7-8 Experimental and numerical thrust values at 1200 V

Simulated	Experimental results	Extrapolated results
165.6 μN	3.374 mN	270 μN

As the numerical model neglects the effect of operating pressure for determining thrust, three possible factors are taken into consideration for the large thrust gap found between the experimental tests and simulation. These factors are:

- Thrust measurement error
- The addition of heavy particles caused by cathode erosion
- Additional ionisation of air molecules

As discussed in chapter 6.3.4, the thrust balance is calibrated using the oscillation period of the pendulum. Since the oscillation period was measured manually, the results display a maximum deviation of 0.2 s from the mean value determined. Therefore, using the root mean square error and adjusting the pendulum oscillation period accordingly, it is calculated that the thruster is subjected to a 20 % error tolerance.

Furthermore, as briefly discussed in chapter 2.1, heavy particles are created during the μPPT ablation process. From the cathode spots observed in Figure 7-14, it is stated that ablated

cathode material largely contributes to the heavy particles ejected from the thruster. As the cathode erosion rate is only measured through vapourisation and ion condensation, a large difference in mathematical and experimental results is observed (Lun, 2008). Thus, a fair argument is made in stating that the addition of micro-particle ejection caused by cathode erosion led to an increase in thrust.

With residual air molecules present during low vacuum pressures, various experimental discharges are investigated to evaluate the influence of additional air molecules contributing to the thrust generated. Therefore, photos of the plasma in experiment 1 are presented in Figure 7-12, discharging at 1200 V at two different pressures.

Experiment 1: 40 mm electrodes



(a)

1200 V at 0.75 Torr pressure



(b)

1200 V at 15 Torr pressure

Figure 7-12 Plasma arc colour for experiments 1 and 2

From Figure 7-12(a), it is shown that four colour variations were emitted during the plasma arc discharge, namely: pink, blue, violet and white. From this, it is found that the pink and blue spectrum represents the presence of ionised Hydrogen and Nitrogen molecules respectively, while the violet emittance indicates ionised Oxygen present. As air is represented by all three of these elements, speculation leans towards additional thrust being generated by these air molecules. Due to the high current discharge, image saturation is observed within the white spectrum. Furthermore, by increasing the chamber pressure to 15 Torr within Figure 7-12(b), results show an increase in the intensity of Nitrogen ionisation, leading to additional accelerated material. From the colour spectrum evaluation on plasma discharges at various pressures, it is

speculated that an increase in pressure leads to an increase in thrust, fully agreeing with the data represented in Figure 7-10.

Experiment 2: 25 mm electrodes



(a)
850 V at 0.75 Torr pressure



(b)
1200 V at 15 Torr pressure

Figure 7-13 Plasma arc colour for experiments 1 and 2. (a) Represents a PPT discharge of low initial voltage, low-pressure environment. (b) represents a PPT discharge of high initial voltage, high-pressure environment.

Conducting similar tests for experiment 2, Figure 7-13(a) displays a low initial voltage test to evaluate the behaviour of the plasma arc within a low-pressure environment. Results show that low ionisation elements such as Hydrogen and Oxygen are present within the acceleration process. When increasing the discharge energy, while testing at higher chamber pressures, it is speculated that Nitrogen ionisation largely contributes to the amount of thrust generated. From this evaluation, it is stated that the additional thrust generated is consistent with the results found in Figure 7-12.

7.2.5 Electrode Length Evaluation

From section 6.2 in chapter 6, it is found that the current path is dependent on the plasma discharge region. As the μ PPT behaves as an electromagnetic gun, accelerating the propellant as a single shot (slug model), excess electrode material extending outward from the plasma front face should have no contribution to the acceleration of the propellant. Therefore, two experiments were conducted to evaluate the influence of the electrode length on the thrust generated by the μ PPT. Evaluating experiment 1, consisting of 40 mm copper electrodes, it was

found that the cathode spots are located within 10 mm from the PFTE discharge surface. From the current distribution discussion within chapter 6.2 and the cathode spot region observation in Figure 7-14, results led to a second experiment (experiment 2) with 25 mm long electrodes.

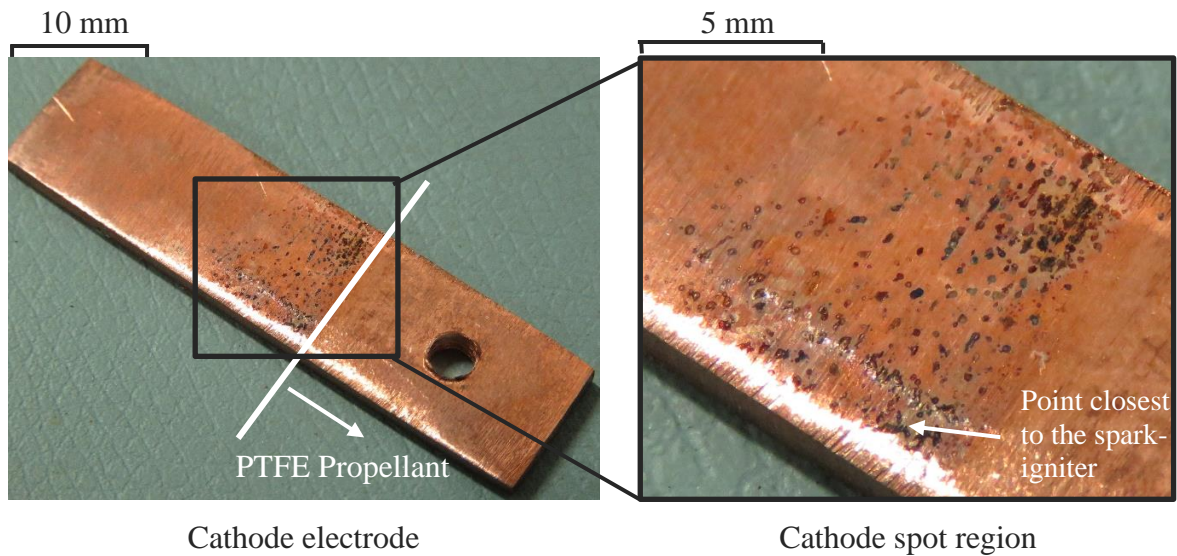


Figure 7-14 Experimental cathode electrode after all experiment 1 tests were conducted

Furthermore, viewing Figure 7-14, heavy cathode erosion is observed when considering the thruster has only been discharged under 500 times. This is because the erosion rate is highly dependent on the surface temperature, discharge current pulse duration, and partially due to the electrode size as it impedes heat dissipation. Research has found that erosion rates drastically increase with high arc currents and longer pulse duration due to gross melting (Lun, 2008).

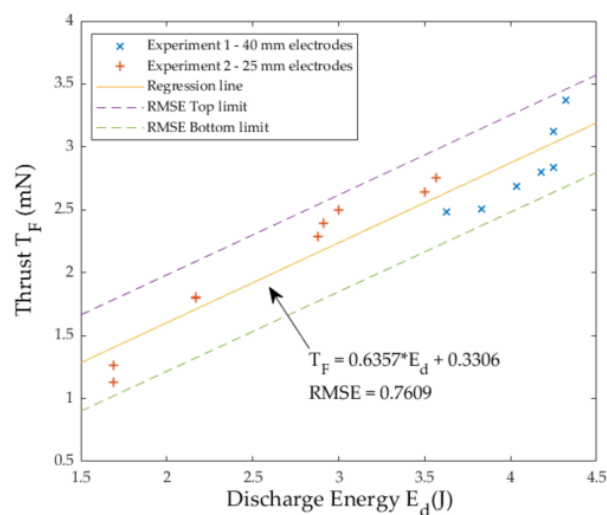


Figure 7-15 Thrust to discharge energy evaluation for both experiments 1 and 2 when varying the electrode length and the discharge energy ($C = 6 \mu\text{F}$)

From the test results found in Figure 7-15, it was found that the longer electrodes have minimal, if any, contributions to the thrust performance of the μ PPT. Comparing these results with the literature of (Arrington, et al., 1997), a clear correspondence is seen in the minimal effect of an increase in electrode length.

7.3 Summary

Throughout this chapter, the experimental limitations and experimental results were presented and discussed. Within the experimental limitations section, it was shown that a lack of instrumentation and equipment led to alternative methods to measure the voltage, current, and thrust of the μ PPT.

Although the voltage divider proved useful for measuring the capacitor voltage without an HV probe, it served as inefficient for measuring the transient response of the system. Therefore, initial testing led to the abandonment of the voltage divider. Furthermore, due to the manual switching operations during PPT testing, a large amount of time elapsed between the charge and discharge time. This led to the voltage divider acting like a bleeding resistor. This led to the conclusion that manual switches are not a good testing mechanism for PPT evaluations.

From the parameter analysis within chapter 7.2, two experiments were conducted to evaluate the effect of the electrode length on the μ PPT performance. In addition, within each experiment, variable discharge energies were tested coherently. Evaluating the voltage discharges for both experiments 1 and 2, while using the circuit capacitance equation from equation (6-1), it was found that the total system resistance equalled 163.69 m Ω and 179.26 m Ω respectively. Using the current discharge results, the average plasma resistance for a 1200 V discharge equalled 37.04 m Ω and 53.159 m Ω for experiment 1 and experiment 2 respectively. Using the total system resistance and plasma resistance from both experiments, it was calculated that the system resistance is 126 m Ω . For this reason, the conclusion was made that the voltage attenuator introduced additional resistance into the system. From the plasma resistance model in equation (6-2), it was calculated that for both experiments 1 and 2 (discharging at 1200 V), the plasma temperature was 3.78 eV and 2.188 eV respectively. Comparing these results to the literature of Nada(2013), a 90% similarity was found for experiment 1 and 81% for experiment 2.

Evaluating the thrust generated within experiments 1 and 2, a clear correlation exists between an increase in pressure and an increase in thrust. Finite limits exist when increasing the operating pressure. Therefore, from the experiment test results, the main discharge becomes unreliable above 15 Torr. From the higher pressure tests, results found that ionisation of air elements greatly contributed to the thrust generated by the μ PPT. Furthermore, the addition of heavy particles and thrust error measurements contributed to the large thrust measured. Extrapolating the thrust generated to LEO operating pressures led to a rough thrust estimate of $270 \mu\text{N}$.

After evaluating the thrust results of experiments 1 and 2, it is concluded that the longer electrodes do not contribute to any additional thrust compared to the shorter electrodes. This result fully agrees with the work described in chapter 6.2.

Chapter 8

Conclusions and Recommended Future work

8.1 Conclusion

The work in this thesis was devoted to the design of a pulsed plasma thruster to set the groundwork for future PPT development for F'SATI satellite missions. Therefore, a micro pulsed plasma thruster was developed for future integration with CubeSat structures and can conform to CDS standards. To do this, a numerical solution was firstly presented using a user-friendly interface. This strategy led to the implementation of a one-dimensional electromechanical model which was validated with the experimental results of two well-known thrusters. Furthermore, conceptual designs and a preliminary design were presented evolving into an experimental prototype. Within the conceptual design, multiple design approaches were presented for both the electrical and geometrical parameters. Within the preliminary design a power circuit solution, as well as a geometrical solution was presented based on the numerical simulation results. The experimental prototype was thereafter presented to show the artefact used for experimental testing. With the experimental prototype, an understanding of the PPT operation and testing methodology was achieved by analysing the results of the voltage discharge, current discharge and thrust generated.

8.1.1 Numerical Model

After the PPT was clearly defined within the conceptual design section, simulation software was developed to numerically solve the electromechanical model and determine estimated thruster performance. To simplify the numerical simulation, a user interface application was designed and can be installed onto a modern-day computer. After validating the model with two

well-known thrusters namely, the LES6 and LES8/9, a high similarity of 81.6% and 96.48% were shown respectively. Using the numerical model, electrical and mechanical geometry comparisons were made to evaluate which system parameters estimated the best thruster performance. Within the electrical tests, it was shown that the energy of the PPT system plays a significant role in the performance of the thruster. As the initial voltage and capacitance are directly related to the discharge energy of the μ PPT, nine simulations were conducted at a system energy of 5 J (or 5 W at 1 Hz). Each test varied the initial voltage and capacitance of the system. After evaluating the results, it was found that a system capacitance of 4.44 μ F operating at an initial voltage of 1500 V delivered the best results. Similarly, the aspect ratio was evaluated by keeping a constant discharge area of 250 mm^2 throughout five tests, while varying the aspect ratio from 0.4 to 2.5. Results of the test found that an aspect ratio of 2.5 delivered the best results.

8.1.2 Design

At the start of this thesis, a propulsion survey was conducted to determine which propulsion type was best suited for this project. Through an elimination process, it was determined that the pulsed plasma thruster was best suited for this project. Thereafter, conceptual designs were presented for both the electrical and geometry types to determine the PPT type for this thesis. From the conceptual designs, it was decided to use the rectangular parallel plate PPT after evaluating the parallel plate side-fed thruster, co-axial breech-fed thruster, and coaxial side-fed thruster in a comparison table within chapter 5.1.1. Within the electrical conceptual design section, the capacitive energy storage unit was chosen over the inductive storage unit and Marx circuit as it was found to be the simplest circuit to characterise, and it is highly popular among PPTs.

Therefore, using the best results from the electrical and mechanical tests, a preliminary design simulation was conducted. From this simulation, it was estimated that the thruster delivers a 195.2 μ N thrust, an exhaust velocity of 6848 m/s, a specific impulse of 698 s, and a 195.3 μ N-s impulse-bit. As the numerical simulation delivered satisfactory results, a preliminary design was presented based on the input parameters from that simulation. The preliminary design consists of both the power circuit design and a CAD model design of the μ PPT. As practical implications prevented the experimental prototype to adhere to the preliminary design, adaptations were made to the experimental prototype. Therefore, the ideally 4.44 μ F capacitor

operating at 1500 V was substituted with two parallel CBB15-1200-3 Film capacitors of 3 μF operating at 1200 V.

8.1.3 Experimental work

Within the experimental work section, work was dedicated towards the voltage discharge, current discharge and thrust measurement of the μPPT . As the required testing equipment was out of reach, an uncalibrated voltage attenuator replaced the high voltage probes required, a shunt resistor replaced the Rogowski coil required, and a self-made thrust balance was used instead of a highly accurate industrial thrust balance. Furthermore, within the experimental work, two test types were evaluated, namely, experiment 1 and experiment 2. These two tests were conducted to evaluate the effect of the electrode length on the performance of the μPPT . Therefore, experiment 1 consisted of a μPPT thruster with 40 mm long electrodes, while experiment 2 consisted of a μPPT thruster with 25 mm long electrodes.

Due to the limited testing equipment, a limitations table was presented at the beginning of chapter 7. As one of the experimental objectives was to gain an understanding of the μPPT operation and testing methodology, the experimental results were examined to understand system characteristics and evaluate parameters influencing the results measured. By doing this, the objective was achieved. Firstly, the voltage discharge of the μPPT was evaluated and presented. Within these tests, the system resistance, system response and the damped harmonic motion were analysed. From the results, it was shown that the system resistance equalled 163.69 m Ω and 179.26 m Ω for experiments 1 and 2 respectively. Furthermore, it was shown that the system has a slow system response with a highly overdamped characteristic for both experiments 1 and 2. Furthermore, comparing the voltage discharge of both experiments, a high level of similarity was observed.

After the voltage discharge evaluation, the current discharge of the μPPT was analysed. Within these tests, a shunt resistor was used due to the difficulty of sourcing a desirable Rogowski coil. Results of the current discharge were used to evaluate the plasma resistance and to determine the effect of the electrode length on the performance of the thruster. Using the results, it was determined that an average plasma resistance of 37.04 m Ω and 53.159 m Ω was present for experiment 1 and experiment 2, respectively. Deducting the plasma resistance for both

experiments from their dedicated total resistance, it was found that the system resistance is approximately 126 m Ω .

Due to the lack of a high precision thrust balance system and high-vacuum chamber, thrust measurement tests were conducted using a self-made thrust balance operating between 0.75 Torr and 18 Torr. As the self-made thrust balance was calibrated manually, an approximate error of 20% was calculated. From the tests conducted, it was found that for a 1200 V discharge, operating at 0.75 Torr, a maximum thrust of 3.374 mN was observed. Within the thrust measuring tests, attention steered towards the effect of the thrust generated when the chamber pressure was changed, variable discharge energies were used, thruster electrode lengths varied, and the colour irradiated during plasma discharge. Results of these tests presented a linear relationship between an increase in chamber pressure, delivering an increase in thrust. From the higher pressure tests, results found that ionisation of air elements greatly contributed to the thrust generated by the μ PPT. Furthermore, the results of experiments 1 and 2 concluded that the longer electrodes do not contribute to any additional thrust compared to the shorter electrodes. Applying extrapolation to the thrust results at a 1200 V discharge within various chamber pressures, a rough estimate was made that the thrust should generate 270 μ N of thrust at LEO pressures.

8.2 Proposed Future Work

As the aim of this thesis is to set the groundwork for future PPT development for F'SATI satellite missions, it opens the opportunity for further researchers to continue with this work. The main areas recommended for future research are directed toward both theoretical and experimental work. Therefore, theoretical models and simulation adjustments are discussed. Furthermore, recommended experimental work is discussed for further evaluation of the pulsed plasma thruster. To end the chapter, additional work towards a possible flight circuit is discussed.

8.2.1 Future Work on Theoretical and Numerical Models

Within this thesis, the general electromechanical model was used to numerically estimate thruster performance. As this model excludes the addition of gas-dynamic forces and externally

applied magnetic fields, it is recommended to investigate these parameters for increased modelling accuracy. Furthermore, to conduct various simulations for future pulsed plasma work, it is recommended to add the snowplow model and coaxial geometries to the written code and application interface. This will not only enable the user to simulate the thruster using different modelling tools, but it will also enable future researchers to expand their research field.

8.2.2 Experimental Future Work

The experimental future work section is divided into two main categories. The first category discusses recommended testing equipment for the experiments conducted within this thesis. This is followed by recommended future tests that can be conducted on the μ PPT model. As discussed throughout previous chapters, experimental tests were adapted due to the lack of required instrumentation. Therefore, the following adjustments can be made to improve experimental results:

- **Voltage discharge measurements:** Within the voltage discharge measurements, a Tektronix P5205 voltage attenuator was used. As this device has no manual calibration options, a slope characteristic was observed within a square wave pulse signal with a duration equal to the discharge period. Furthermore, this voltage attenuator is only limited to a maximum input voltage of 1300 V, thus restricting measuring capabilities at higher voltages. For these reasons, it is recommended to use an HV probe that is can handle double the required input voltage. Therefore a 3 kV HV probe or higher is required for this work.
- **Current discharge measurements:** During the current discharge measurements a shunt resistor was used. This was done by measuring the voltage drop over the resistor and using Ohm's law to determine the current. Although results were obtained for these tests, it is yet unclear how the characteristics of the shunt resistor are affected when exceeding the maximum current and voltage parameters set for the specific shunt resistor. Therefore, two types of current tests are recommended.

The first method consists of keeping the shunt resistor as it is a cheap and quick solution to measure the discharge current. Although an easy solution, additional tests will have to be conducted to ensure that the integrity of the shunt resistor's characteristics remains constant. To do this, the resistance of the shunt resistor will have

to be measured before any tests. Thereafter, multiple tests will have to be conducted to answer the following questions:

- Do the resistor characteristics change after multiple discharges?
- Is there a linear relationship between the voltage drop and the current when exceeding the maximum threshold of the shunt resistor?
- How well does the shunt resistor respond to transient responses?

The second method consists of using a Rogowski coil to measure the current discharge. This method is the most popular method used for PPT current discharge measurements. To implement the Rogowski coil, an integrator is required leading to a calibration process for accurate results.

- **Vacuum chamber adaptations:** Within this thesis, a vacuum chamber with a maximum vacuum pressure of 0.75 Torr was used. As LEO pressures range between 1×10^{-9} Torr to 7.5×10^{-10} Torr, additional vacuum pumps are required. Therefore, to test within these low pressures, three types of pumps are ideally required. These pumps are a rotary centrifugal pump (1 bar to 10^{-4} mbar), a turbopump (10^{-4} mbar to 10^{-7} mbar), and an ion pump (10^{-7} mbar - 10^{-11} mbar). Although the ultra-high vacuum pressures from an ion pump would be ideal, pressures generated by the high-vacuum turbopump will also be sufficient for general testing.

Furthermore, it is recommended that two of the vacuum chamber sides are transparent. This is required when conducting plasma interferometry and spectroscopy tests as described later in this chapter.

- **Discharge mass measurements:** From the limited number of discharges throughout the experimental procedure, the 0.1 mg scale available failed to deliver an accurate mass per discharge. For the experimental prototype testing, an assumed mass discharge of 2.85×10^{-8} kg was assumed. Due to the large difference between the numerical model simulations and experimental tests, this assumed value could not be used in further performance calculations. Therefore, the mass discharge should be measured. Although an optimal solution would utilise an ultra-fine scale being used for these tests, it is rather suggested that a large amount of PPT discharges should be averaged out to calculate the mass per discharge.

From the discussion on recommended testing equipment for the experiments conducted within this thesis, future tests on the μ PPT model are presented.

The first recommendation is the addition of plasma interferometry and spectroscopy tests for the μ PPT. Within the interferometry tests, plasma density can be determined. Although many methods have been developed over the years, due to the space constraints within the vacuum chamber, it is found that the Herriot Cell technique works well for these tests. This is due to the increased path length of the laser, inherently increasing the accuracy of the measurements. Within the spectroscopy tests, plasma temperature can be determined. As plasma interferometry and spectroscopy inherently characterise the plasma, the results can be used to determine the plasma resistance and evaluate if there is a relationship between the plasma characteristics and thruster performance.

The second recommendation is the evaluation of the spark-igniter position within the μ PPT system. Within the experimental prototype, the spark-igniter was placed perpendicular to the propellant surface (as shown by the red vertical arrow below in Figure 8-1) and electrode face (shown by the short arrow pointing towards the electrode in Figure 8-1).

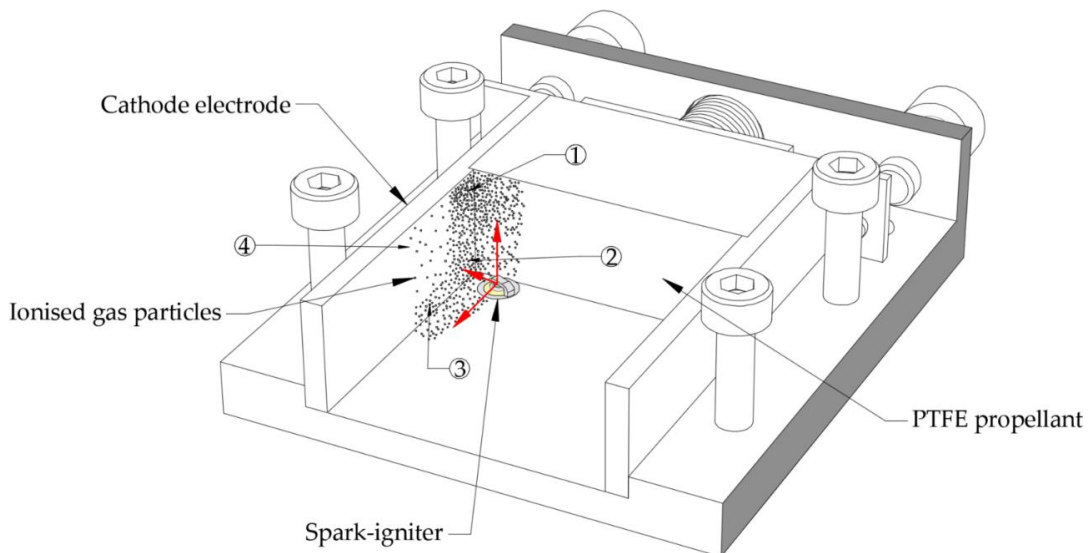


Figure 8-1 μ PPT experimental prototype with the estimated initial gas environment for main PPT discharge. The dots represent ionised molecules created after the initial spark-igniter discharge. The spark-igniter's front face is placed perpendicular to the propellant discharge surface and electrode face, while placed in the outer cover of the μ PPT.

Within the experimental tests, a grouping of cathode spots was found. This grouping was mostly found in sections 1 and 2 as visually presented in Figure 8-1. As a high erosion rate was found within sections 1 and 2, it is speculated that the highest density of ionised gas field is found within the corners closest to the spark-igniter. Therefore, it is recommended to conduct various experiments while moving the spark-igniter. Understanding the effect of the spark-igniter position on electrode erosion rate can be extremely advantageous, especially when considering long-term missions.

The third recommendation focus on work dedicated to the thrust balance for this thesis and a potential replacement. Evaluating the torsional balance used within this thesis, a 20 % error was found for the thrust measurement. This error was due to the hand measurements taken while calibrating the system. For higher accuracy results, a proximity sensor can be used to determine the oscillation period. Furthermore, From the camera footage taken during testing, it was found that pendulum drifting occurred. This is due to the torsion wire's inability to resist deflection when a rapid radial force is applied to it. As a rigid wire would solve the drifting problem, it will allow for small deflection angles, leading to a less accurate system. Therefore, it is also proposed to investigate a rigid cantilever thrust measuring system as proposed by (Lun, 2008). This induced strain can then be measured by the use of strain gauges and eliminates the drifting and rotational problems.

A fourth recommendation is presented to address the electrical circuit used for PPT operation. As the electrical circuit within this thesis was merely used for experimental testing, a practical flight operation was not possible. Therefore, future work can be dedicated to a complete flight solution for autonomous operation. Within Appendix E, a partial solution to a future electrical flight model is presented. This model briefly describes how the circuitry can be adapted to suit autonomous operations and achieve desired discharge frequency.

Appendices

Appendix A

Review on Available Propulsion Technology for Nanosatellites

A.1 Descriptive Characteristics of Variable Thrusters

Within this section, key characteristics are discussed of various thruster types for micro-propulsion applications. It should be noted that only relevant information about each thruster is listed and that only a selection of thrusters is presented. This section includes both electrical and chemical thrusters.

A.1.1 Electric Propulsion

(μ PPT) Micro Pulsed Plasma Thruster

- Scalable
- Low power requirements
- Solid or liquid propellant
- Quasi-neutral plasma (no neutraliser required)
- Simplistic
- Low system mass

- Spark-igniter required
- Well-proven technology (Space Heritage)
- Risk of electromagnetic interference

(μ VAT) Micro Vacuum Arc Thruster

- Scalable
- Low mass
- Any conductive material can be used for propellant
- Risk of spacecraft contamination
- Simplistic
- Minimal spacecraft experience

(μ IT) Micro Ion Thruster

- High efficiency
- Involves positively charged ions (neutralizer required)
- Grid erosion
- Scaling difficulty
- Complex

(μ HT) Micro Hall Thruster

- High efficiency
- Large specific impulse
- Scaling difficulty
- Neutraliser required
- Possible overheating problems

(FEEP) Field Emission Electric Propulsion

- Generates low thrust
- Ultra-precision

- Large specific impulse
- High voltages required
- Neutraliser required
- Risk of spacecraft contamination

(μ RJT) Micro Resistojet Thruster

- Limited Specific impulse (< 500 s)
- No contamination onto the spacecraft
- Low system mass

A.1.2 Chemical Propulsion

Cold Gas Thruster

- Low/Limited Specific impulse (\ll 300 s)
- High thrust generation
- Well-proven technology
- Risk of propellant leakage

Monopropellant Thruster

- Low/Limited Specific impulse (\ll 300 s)
- High thrust generation
- High power consumption
- Heavy and large
- Scaling difficulty

A.2 Performance Evaluation of the Variable Thrusters Mentioned

Table A-1 Thruster Evaluation (Adapted from Lun (2008), Scharlemann et al. (2011), Mueller et al. (2010) and Zandbergen (2013))

Performance Parameters	Electrical Thrusters							Chemical Thrusters		
	μ PPT	μ VAT	μ IT	μ HT	FEEP	MPD	μ RJT	Cold gas	Mono prop.	Bi-prop.
Specific Impulse (s)	500-1000	500-3000	1800-3184	-	4000-12000	-	56-150	65	130-220	-
Efficiency range (%)	5%-16%	13%	6%	-	30%-45%	-	55%-68%	-	-	-
Propellant	PTFE	*Al.	Xenon	Xenon	Liquid metal	-	N_2H_4	Various	H_2O_2 N_2H_4	Various
Feed mechanism	Yes	Yes	Yes	Yes	Yes	Yes	Yes	Yes	No	Yes
System Mass (g)	180-600	250-500	1250	-	500	-	50	-	100	-
Operating frequency (Hz)	1-2	100-1000	DC	-	DC	-	-	-	-	-
Impulse-bit (μ Ns)	1-80	0.01-30	DC	-	DC	-	-	550	1	-
Total impulse (μ N/s)	30-252		976	-	-	-	-	-	800-1000	-
Input Power (W)	1-20	1-30	10-43	-	0.5-10	-	0.55-3	-	1	-
Thrust (μ N)	1-500	0.01-3000	67-1500	-	100	-	100-500	55	1000	-
Thrust/Power (μ N/W)	25	18	6.7-35	-	12.5-20	-	182	-	1000	-

* - *Generally*

Analysing Table A-1, it is shown that most EP systems have a thrust-to-power ratio between 10-200 μ N/W. Therefore, considering a thruster operating at 5 W and assuming that there is a linear thrust increase approach, a thrust of over 1 mN can be expected from some of these thrusters, theoretically.

Due to the high thrust values generated by chemical propulsion systems, they are useful in orbital manoeuvres for nanosatellites. Although the thrust values are exciting, chemical propulsion systems have a small specific impulse. This factor gives electric propulsion devices a great advantage over these chemical thrusters. Considering nanosatellites generally have a mission timeframe of three years or more, chemical propulsion display a low specific impulse and additional complexity; it was decided to eliminate chemical propulsion systems for further development in this thesis.

From the electric propulsion systems discussed, the μ IT and the μ HT seem promising in their high specific impulse and thrust capabilities. As this might seem ideal for the outcome of this project, due to the complex designs, charged particles, high mass, high power requirements and scaling difficulties; a decision was made to eliminate these thrusters from the list. Similar to the μ IT, the Magnetoplasmadynamic thruster also show the difficulty in its ability to scale its power requirements to that of the CubeSat standard. Therefore, the most promising propulsion types on this list are the μ PPT, μ VAT, FEEP and μ RJT. Each of these propulsion types shows promising characteristics in certain areas but lacks in others. For the μ RJT, a substantial thrust to power ratio is observed but is directly followed by a very small specific impulse. This leaves the three thruster possibilities which can be used for this project, namely the μ PPT, μ VAT and FEEP thrusters. Furthermore, within the work of (Scharlemann, et al., 2011), the authors concluded that the PPT and VAT are the best suited for nanosatellite applications. With the additional FEEP thruster, a comparison table is presented in Table A-2.

Table A-2 Final Comparisons of PPT, VAT and FEEP Thruster Systems

PPT		VAT		FEEP	
Pros.	Cons.	Pros.	Cons.	Pros.	Cons.
Low power requirements	Sparkplug required	Low power requirements	Small impulse-Bit	Low power requirements	Propellant Heating
Scalable	Ionisation energy loss	Scalable	Ionisation energy loss	Ultra-precision thrust	Neutralizer required
Simplistic	Lower thrust accuracy	Simplistic	Lower thrust accuracy	Uniform thrust	Small impulse-Bit
Low system mass		Low system mass		Low system mass	Complex machining
Well-proven technology		High I_{SP}		Very High I_{SP}	Risk of contamination
Throttle capabilities		Throttle capabilities		Small impulse-Bit	Low thrust
Zero warmup time		Zero warmup time		High efficiency	
Small to High Impulse-Bit		Small impulse-Bit		Throttle capabilities	
Quasi-neutral		Quasi-neutral			
Fail-safe		Fail-safe			
Long shelf life		Long shelf life			
Proven Reliability					

Analysing Table A-2, it is evident that all three thrusters are suitable for the use of small/nano spacecrafts. Thus, to determine which thruster is most appropriate for this project, the question of ‘What does this project require’ must constantly be weighed when analysing these thruster characteristics. The FEEP thruster displays remarkable specific impulse figures, outclassing the μ VAT and μ PPT. It also delivers ultra-precision thrust and throttling capabilities which can be very beneficial to the orientation of the spacecraft. The complex machining, neutraliser, overheating and possible spacecraft contamination can be problematic. The μ VAT shows great potential for the use on nanosatellites with its high specific impulse and simplicity, but its lack of flight time and small impulse-bit is an area of concern. Although the μ PPT has some characteristics which do not live up to those of the μ VAT and FEEP thruster, it does show a great track record on reliability during space missions as seen on the LES-6, Nova 1-3, LES 8/9 and many more (McGuire & Myers, 1996). Furthermore, due to its simplicity, throttling capabilities and numerous advantages mentioned in chapter 2.1, it is an attractive option for this project. After considering all the pros and cons of these thrusters, the μ PPT is chosen for this project. This is due to the simplicity, reliability and space heritage of the thruster while having respectable performance characteristics.

Appendix B

Computer-Aided Design of Preliminary Design Components

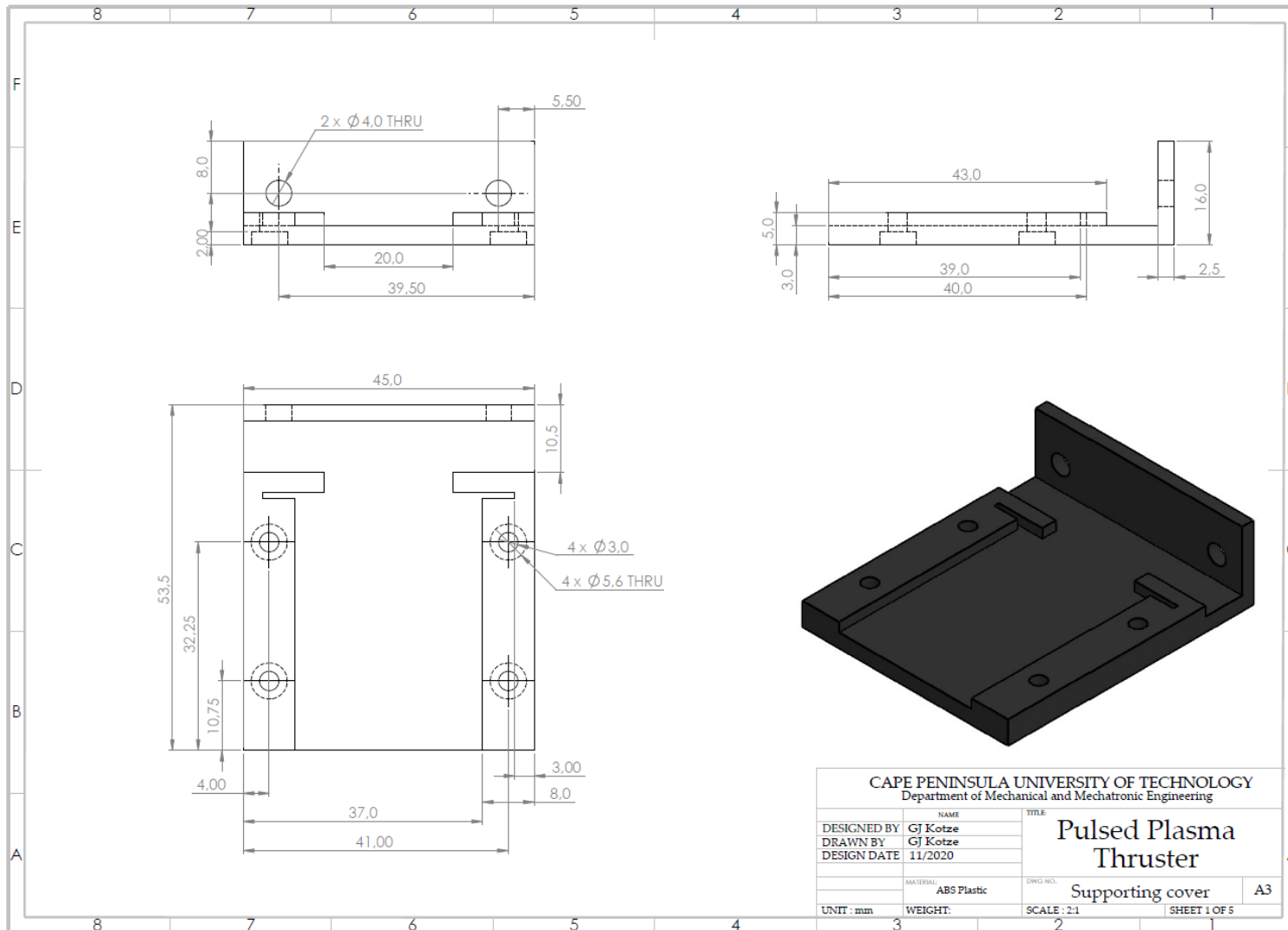


Figure B-1 PPT supporting cover

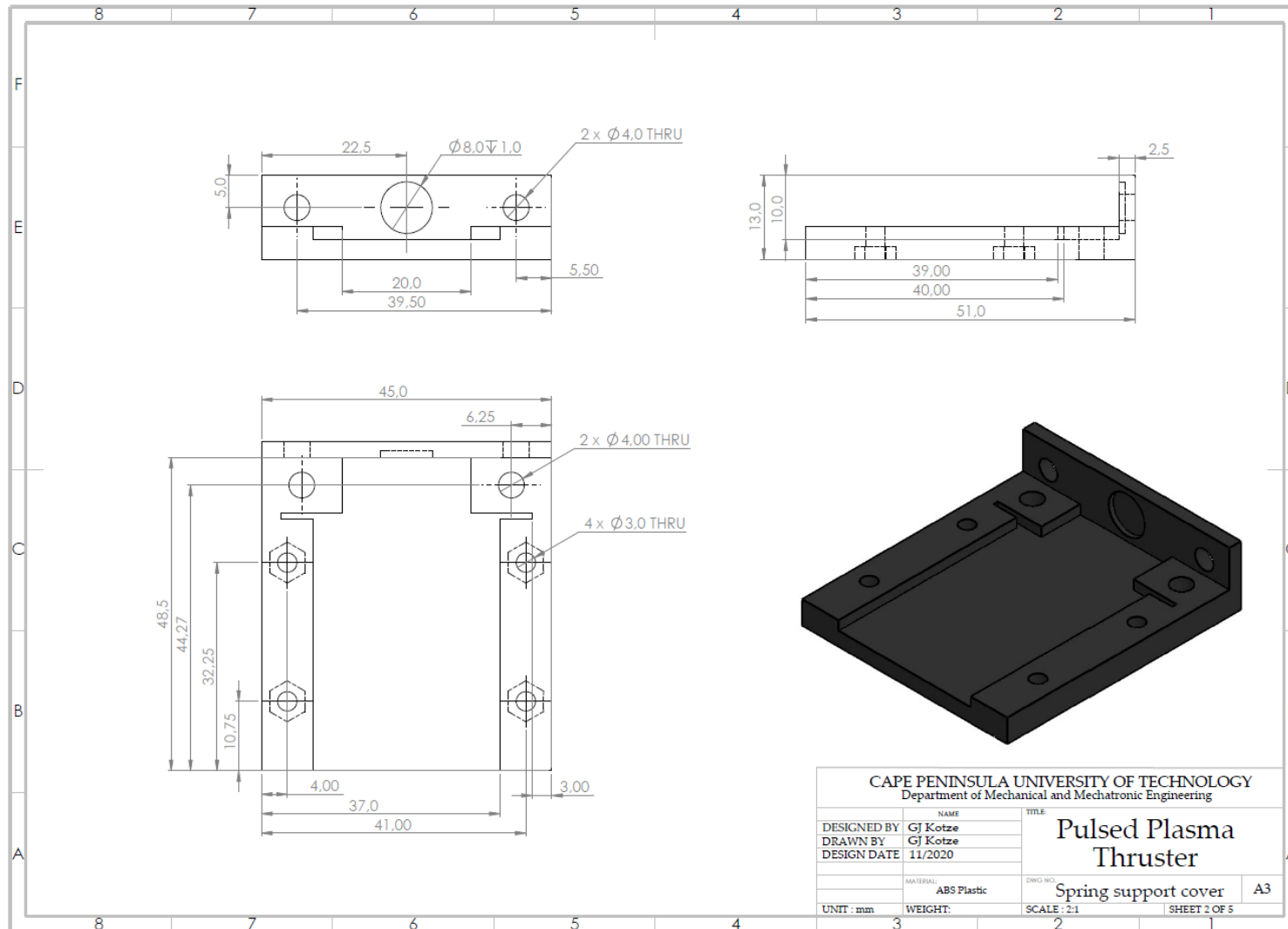


Figure B-2 PPT and spring support cover

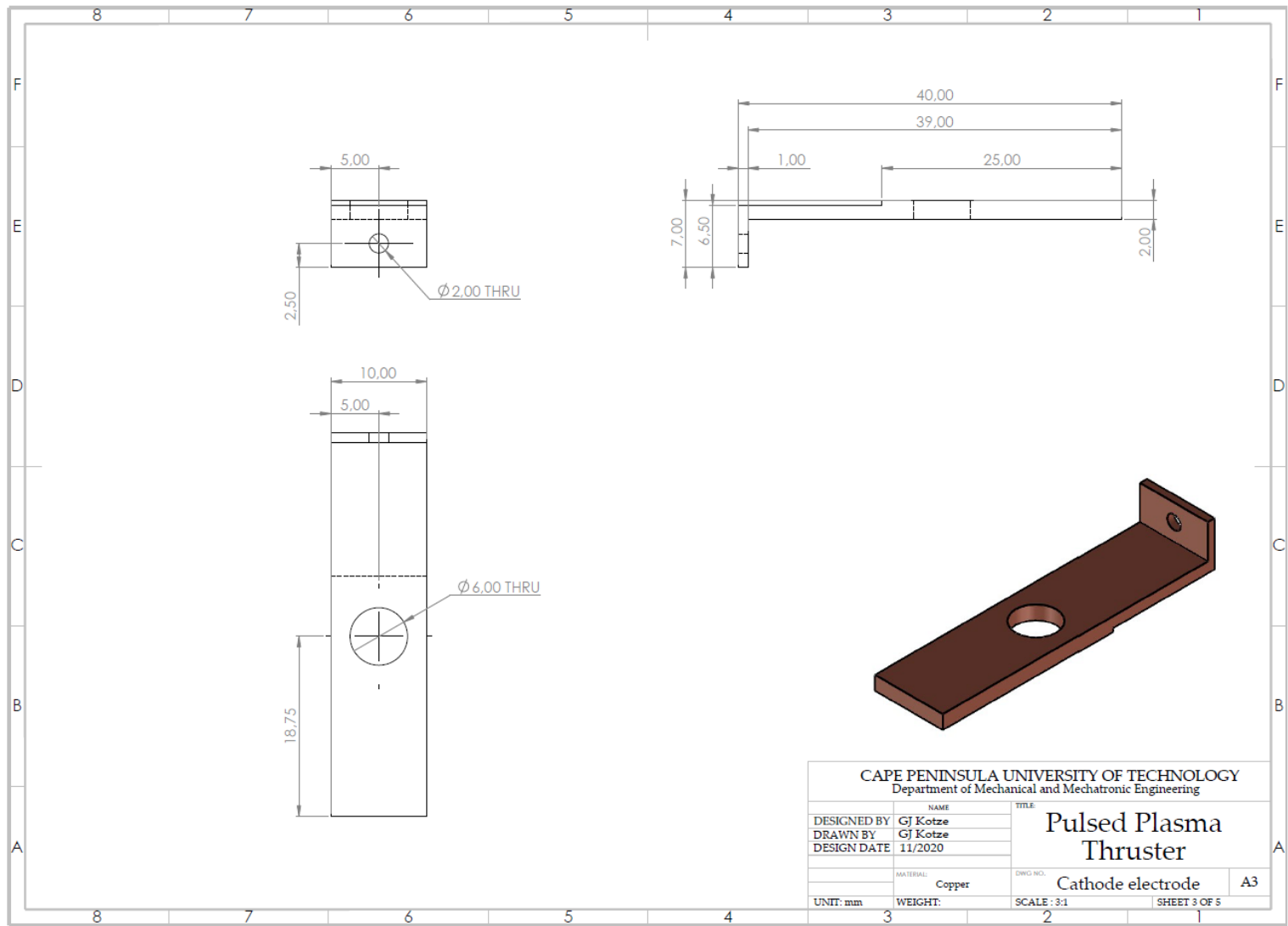


Figure B-3 PPT cathode electrode

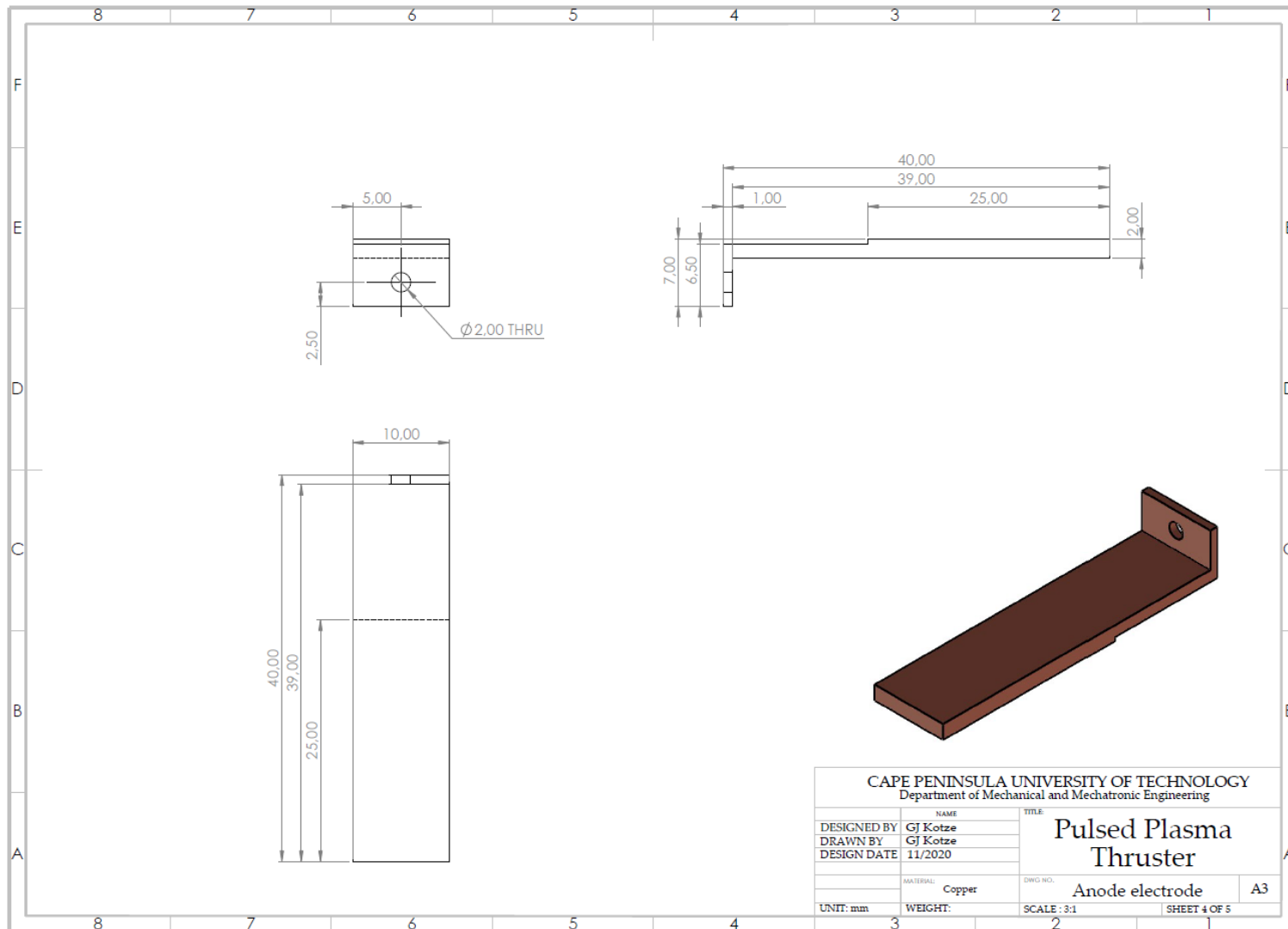


Figure B-4 PPT anode electrode

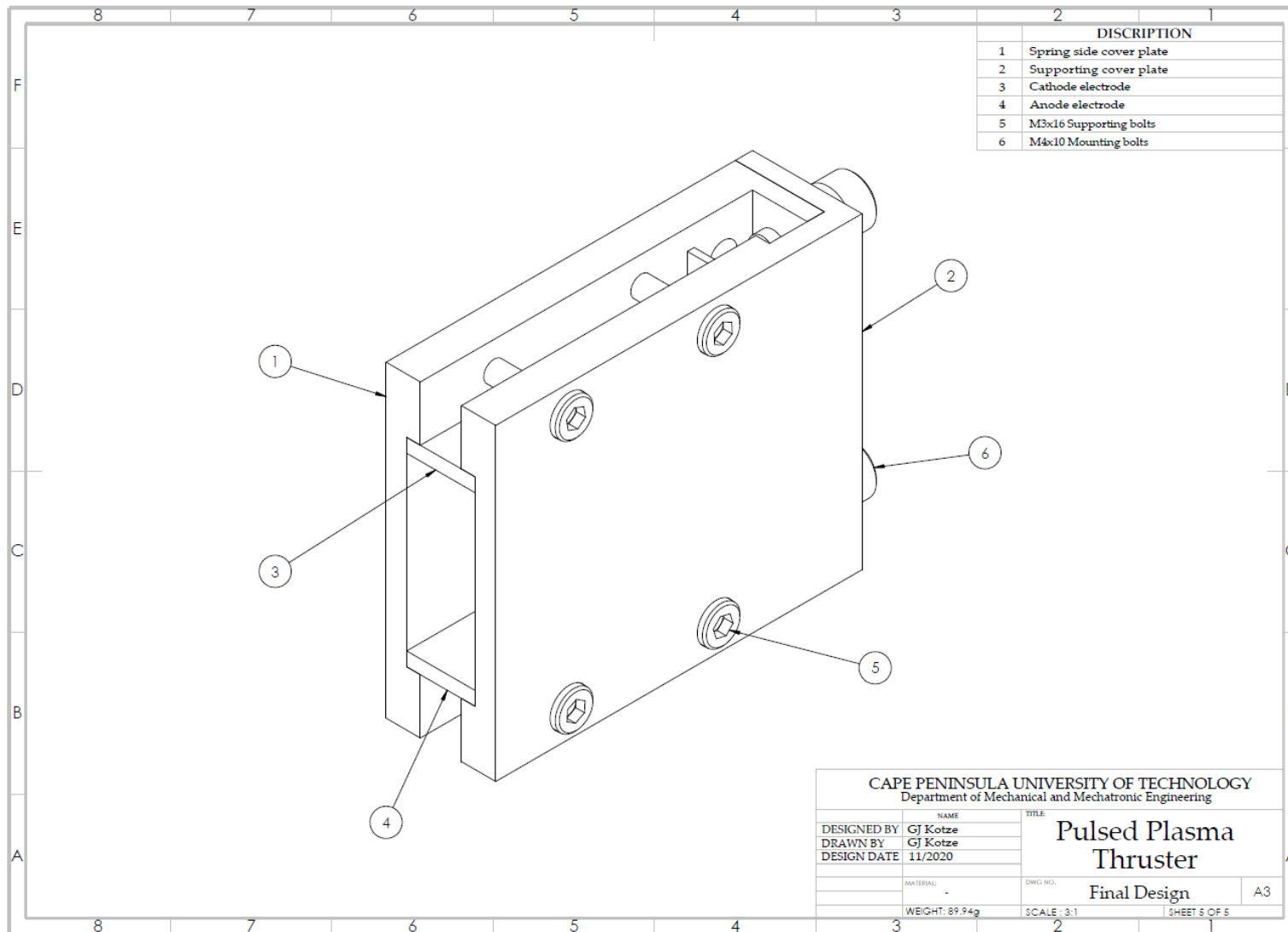
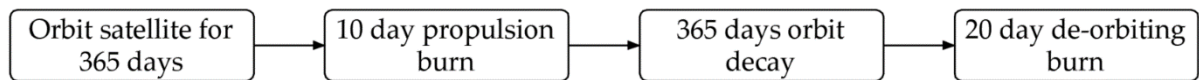


Figure B-5 PPT final design

Appendix C

STK Simulation for Preliminary Design

Within this section, the flight operation model is used to evaluate the orbital capabilities of a 3U CubeSat. Using an STK model developed by (Jourbert, 2021), orbital maintenance and de-orbiting capabilities are tested and thereafter discussed. All variables inserted into STK are obtained from the numerical simulation results presented in chapter 4.7.3. For orbital testing, four tests are integrated into a single mission. These tests are executed sequentially and are ordered as,



Test 1: Orbital decay at 500 km

Within the first test, an evaluation is done on the natural behaviour of the orbit of the satellite throughout a single year.

Table C-1 Orbital parameters simulation results during the first year in orbit

Initial conditions		After 365 days in orbit	
Orbital Parameters	Value	Orbital Parameters	Value
Duration	-	Duration	365 days
Altitude Of apoapsis	500 km	Altitude Of apoapsis	499.46 km
Altitude Of periapsis	500 km	Altitude Of periapsis	473.84 km
Atmospheric pressure	2.33×10^{-9} Torr	Atmospheric pressure	6.77×10^{-9} Torr
Eccentricity	0	Eccentricity	0.0018647
Grams fuel used	0 g	Grams fuel used	0 g
Specific Impulse	0 s	Specific Impulse	0 s
Delta-V	0 m/s	Delta-V	0 m/s

From the initial conditions and orbital parameters after 365 days, observed in Table C-1, it is shown that a natural change in eccentricity occurs. Evaluating the periapsis and apoapsis after 365 days, it is found that the altitude of the satellite decreased by 5.232% and 0.108% respectively. From this data, it is estimated that the CubeSat will have an orbital lifetime of approximately 19 years. Orbital decay within the first 365 days can be observed in Figure C-1.

Test 2: 10-day thrust burn

Within test 2, the μ PPT thruster was activated for 10 days after the initial 365 days in orbit. This is to illustrate the orbital maintenance and altitude control capabilities of the thruster.

Table C-2 Orbital parameters during 10-day burn

Before thruster is turned on		After thruster was turned on for 10 days	
Orbital Parameters	Value	Orbital Parameters	Value
Duration	365 days	Duration	10 days
Altitude Of apoapsis	499.46 km	Altitude Of apoapsis	572.64 km
Altitude Of periapsis	473.84 km	Altitude Of periapsis	508.72 km
Atmospheric pressure	6.77×10^{-9} Torr	Atmospheric pressure	1.85×10^{-9} Torr
Eccentricity	0.001865	Eccentricity	0.004619
Grams fuel used	0 g	Grams fuel used	15.747031 g
Specific Impulse	0 s	Specific Impulse	713.80 s
Delta-V	0 km/s	Delta-V	27.611638 m/s

From Table C-2, it is shown that for the periapsis and apoapsis, an orbital altitude increase of 7.36% and 14.65% can be expected, respectively. Comparing the orbital decay found throughout test 1 with the orbit altitude increase for test 2, it is found that for both the periapsis and apoapsis a rate of change of 5134% and $4952 \times 10^3\%$ is determined, respectively. From the periapsis, apoapsis and eccentricity results are shown in Table C-2, an increased eccentricity of approximately 250% is found. If space mission requirements do not allow for large eccentricity changes, alternative thrust methods can be used. One of these methods includes an increase in altitude adjustment time, while another method comprises of lowering the pulse rate of the thruster. For a visual representation, Figure C-1 presents the altitude control capabilities of the CubeSat for a 10-day burst.

Test 3: Orbital decay at higher altitudes

After the 10-day thruster burn from test 2, the orbital parameters of the satellite are once again observed over a period of 365 days to evaluate the orbital decay at higher altitudes.

Table C-3 Orbital parameters at higher altitudes

The moment before thruster is turned off		After 365 days in orbit	
Orbital Parameters	Value	Orbital Parameters	Value
Duration	-	Duration	365 days
Altitude Of apoapsis	572.64 km	Altitude Of apoapsis	560.48 km
Altitude Of periapsis	508.72 km	Altitude Of periapsis	495.38 km
Atmospheric pressure	1.85×10^{-9} Torr	Atmospheric pressure	2.12×10^{-9} Torr
Eccentricity	0.004619	Eccentricity	0.004713
Grams fuel used	15.747031 g	Grams fuel used	0 g
Specific Impulse	713.80 s	Specific Impulse	0 s
Delta-V	27.611638 m/s	Delta-V	0 m/s

From Table C-3, a decay in altitude is shown for both the periapsis and apoapsis. From the simulation results, it is found that the periapsis and apoapsis experienced a 2.62% and 2.12% orbital decay, respectively. From this data, it is estimated that the CubeSat will have an orbital lifetime of approximately 38 years. Comparing the orbital decay of test 1 with test 3, it is clear that the altitude of the thruster has a drastic effect on the orbital lifetime of a satellite. To view the orbital decay rate between test 1 and test 3, Figure C-1 is presented.

Test 4: 20-day de-orbiting burn.

Within this test, the de-orbiting capabilities of the CubeSat are presented. To do this, the satellite rotates by 180° facing the opposite direction. When the thruster is activated, it inherently acts as a brake, reducing the CubeSat’s orbital velocity.

Table C-4 Orbital parameters during de-orbiting

Test 3: Moment before thruster is turned on		Test 4: Post 20-day burn	
Orbital Parameters	Value	Orbital Parameters	Value
Duration	-	Duration	20 days
Altitude Of apoapsis	572.64 km	Altitude Of apoapsis	471.16 km
Altitude Of periapsis	508.72 km	Altitude Of periapsis	380.93 km
Atmospheric pressure	1.85×10^{-9} Torr	Atmospheric pressure	2.12×10^{-9} Torr
Eccentricity	0.004713	Eccentricity	0.006631
Grams fuel used	0 g	Grams fuel used	32.725182 g
Specific Impulse	0 s	Specific Impulse	713.80 s
Delta-V	0 m/s	Delta-V	57.732728 m/s

From viewing Table C-4, it is clear that the altitude of both the periapsis and apoapsis in test 4 is significantly lower than in test 3. Through this test, it is shown that for the periapsis and apoapsis, a 25.12% and 17.72% decay in altitude can be achieved within 20 days of operation respectively. As the rate of decay is inversely proportional to the orbit height, it was determined that the CubeSat will de-orbit within a 25-day timeframe.

Analysing the fuel consumption data presented in Table C-4, it should be noted that the total volume of propellant required is 14.875 cm^3 . Comparing this volume with the propellant volume of 3.75 cm^3 found in the preliminary design, an additional/extended PTFE propellant bar is required for de-orbiting the CubeSat. When assuming the mass discharge with each pulse is $28 \mu\text{g}$, it is determined that the propellant block depth required, is 59.5 mm deep.

From these results, it is shown that a 3U CubeSat does theoretically possess orbital manoeuvring and de-orbiting capabilities when equipped with the preliminary design model presented within this thesis. Although true, it should be stated that to successfully de-orbit within 25 days, the propellant bar will need to be extended.

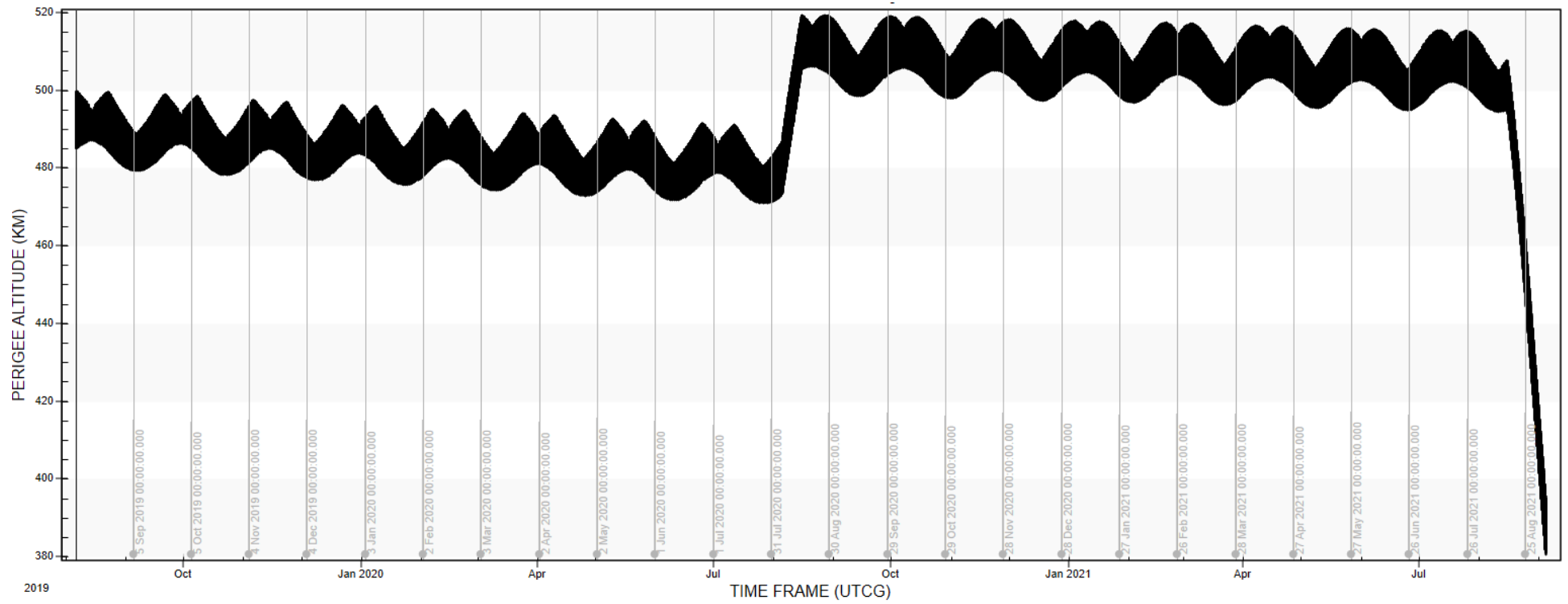


Figure C-1 Orbital mission example of a 3U CubeSat using the performance parameters of the preliminary design μ PPT thruster within this thesis.

Appendix D

Measuring the Discharge Voltage using a Self-Made Voltage Divider

Initially, a voltage divider was designed to ensure that each capacitor bank of the main discharge circuit and the spark-igniter circuit were charged to the required voltage. This was primarily done to accommodate the limited voltage capacity of the multimeter and oscilloscope probes used. At first, the voltage divider was designed to reduce the system voltage by a ratio of 1:10. Therefore, when the capacitor is charged to 1200 V, a 120 V was observed on the multimeter. This was done by applying the voltage divider rule,

$$V_{R2} = V_{in} \cdot \left(\frac{R2}{R1 + R2} \right) \quad (D-1)$$

where R_1 , R_2 , V_{in} and V_{R2} represents resistor 1, resistor 2, the initial voltage and voltage across $R2$. Considering that the voltage divider is placed parallel to the capacitors, as seen in Figure D-2, a high initial resistance ($R1$) of 100 M Ω was chosen to limit the voltage drop over the capacitors. Therefore, to achieve the desired $V_{R2} = 120 V$ and considering that the capacitors are charged to 1200 V, $\therefore V_{in} = 1200 V$, it was calculated that a 11.11 M Ω secondary resistor ($R2$) was required.

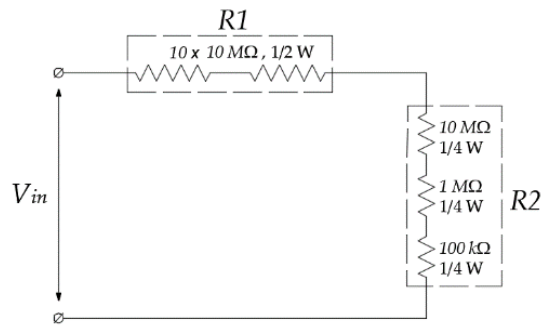


Figure D-1 Experiment voltage divider

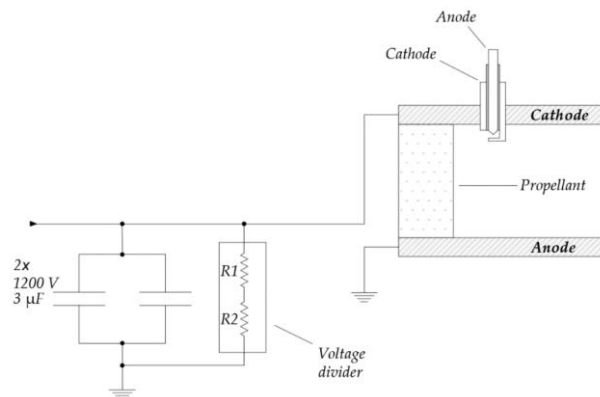


Figure D-2 Voltage divider implementation

From preliminary system testing, it was found that $R1$ had a total resistance of $111 \text{ M}\Omega$ due to resistor tolerances. Furthermore, it was found that the voltage reduction yielded a 1:20.41 ratio. This was due to the negligence of the internal resistance within the multi-meter. Attending to the internal resistance (R_{int}) within the system and integrating it into equation (D-1) yields,

$$V_{R2} = V_{in} \cdot \left(\frac{\left(\frac{1}{R2} + \frac{1}{R_{int}} \right)}{R1 + \left(\frac{1}{R2} + \frac{1}{R_{int}} \right)} \right) \quad (D-2)$$

From the voltage divider reduction ratio results, it was concluded that the voltage divider provided a satisfactory result in measuring the voltage of the capacitors but added excessive amounts of additional resistance to the system. Due to this reason, the voltage divider was abandoned for further testing.

Appendix D

Proposed Circuitry for Future Research

Within this section, a proposed circuit is presented for the use of further research and development. Due to the diverse range of these satellites, the proposed circuit design follows the regulations set by the CubeSat Design Standards (CDS) discussed in chapter 1.1.4. Electrical and circuit operation designs are presented with their dedicated descriptions. To ensure that the entire thruster assembly fits into the required 1U volume within a CubeSat, the assembly is designed to fit onto a PCB board dimensioned according to the PC-104 standards.

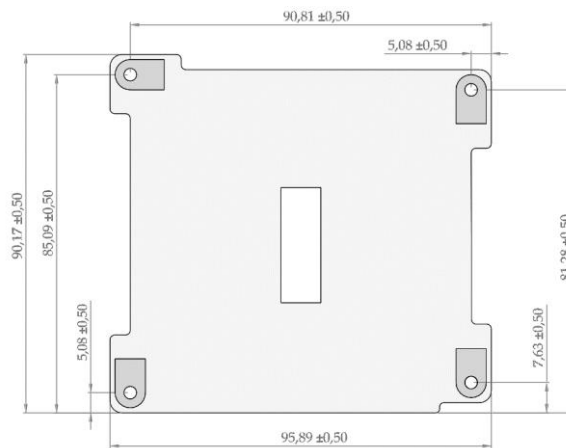


Figure E-1 PCB base conforming to PC-104 standards

Electrical design

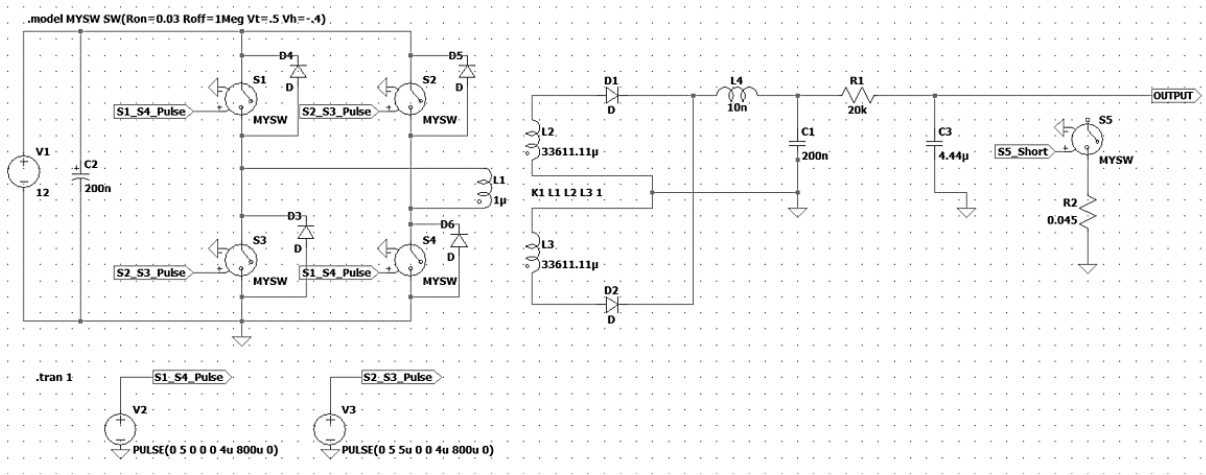


Figure E-2 LT Spice full-bridge DC-DC converter

Circuit Operation

As the μ PPT is designed to operate at a 1 Hz discharge frequency, the power transistors will have to operate at a given pulse signal. To do this, the EPS will supply the power transistors with a 5 V pulsed input signal, essentially controlling the charge/discharge cycles. Within LTSpice, the following circuit was simulated to evaluate the charge and discharge operation using power transistors.

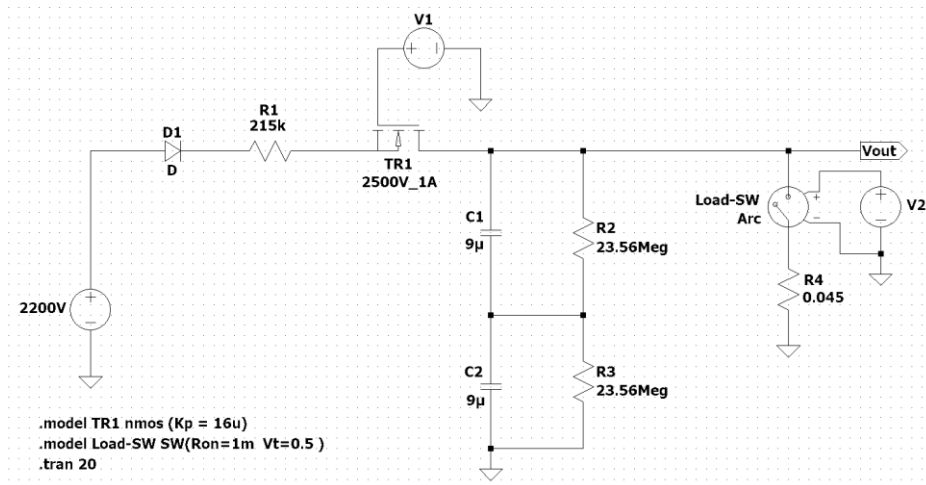


Figure E-3 LTSpice charge/discharge configuration

For the circuit in Figure E-2, an input pulse signal, displayed in Figure E-3, is used to charge the power transistor to the required voltage. As the arc switch in Figure E-2 represents the main discharge of the system, it can be said that the switch represents the power transistor of the

spark-igniter circuit. Therefore, Figure E-4 represents the required pulsed signal supplied from the EPS to discharge the spark-igniter.

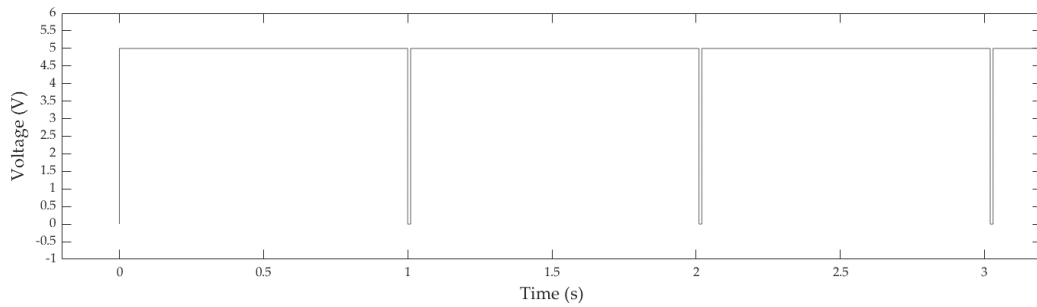


Figure E-4 Input pulse signal from EPS for charging

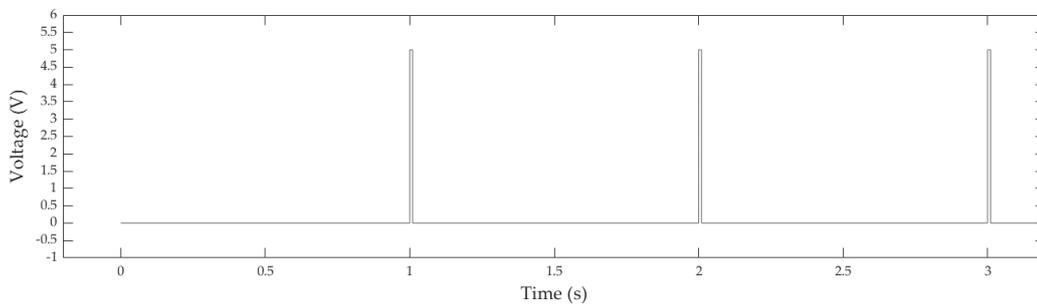


Figure E-5 Input pulse signal from EPS for discharging

As the spark-igniter initially discharges, it allows for a low dielectric environment for the main discharge of the system to initiate. For this reason, we state that a vacuum triggerless mechanism is used as mentioned in chapter 2.6. Combining the charge and discharge cycles of the system, Figure E-5 represents the operating sequence of the μ PPT.

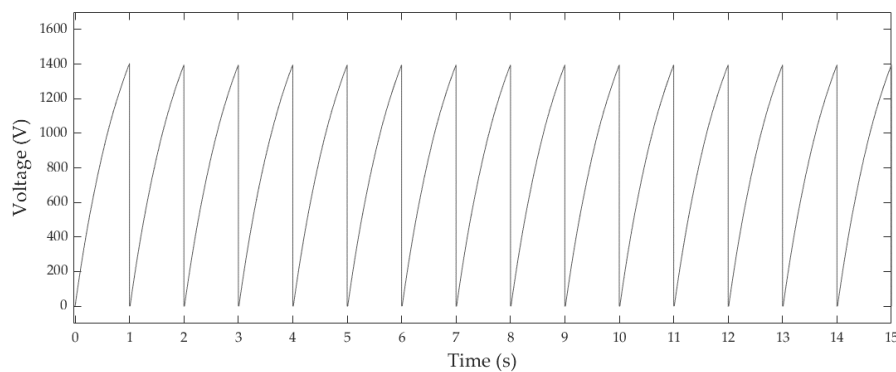


Figure E-6 μ PPT charge/discharge cycles simulation

Bibliography

Berkery, J. W., Markusic, T. E. & Choueiri, E. Y., 2007. Laser interferometry measurements of a high density propagating current sheet. *Plasma Sources Sci. Technology*, 16(1), pp. 233-239.

Aerospace, C., 2020. *CU Aerospace*. [Online]

Available at: <http://www.cuaerospace.com/technology-products/compact-small-satellite-propulsion-unit-cubesats>

[Accessed 12 08 2020].

Akimov, V. et al., 1997. ANALYSIS OF PPT POTENTIALITIES IN SOLVING THE SATELLITE ORBIT CONTROL TASKS. *25th International Electric Propulsion Conference*, pp. 97-146.

Anon., 2020. *Amaya Space*. [Online]

Available at: <https://amayaspacespace.com/>

[Accessed 30 06 2020].

Anon., n.d. *Institute of Space and Astronautical Science*. [Online]

Available at: <http://www.isas.jaxa.jp/en/>

[Accessed 25 05 2020].

Anon., n.d. *S. P. Korolev Rocket and Space Corporation Energia*. [Online]

Available at: <https://www.energia.ru/english/>

[Accessed 24 05 2020].

Arhipov, B. A. et al., 1997. *Development and Application of Electric Thrusters at EDB "Fakel"*. Cleveland, USA, s.n.

Arrington, L. A., Haag, T. W. & Meckel, N. J., 1997. *A performance comparison of pulsed plasma thruster electrode configurations*. Ohio, Electric Rocket Propulsion Society, p. 8.

Aston, G. & Pless, L. C., 1981. Igniter plug erosion and arc initiation processes in one-millipound pulsed plasma thruster. *15th International Electric Propulsion Conference*, 21-23 April.

Black, H. D., Jenkins, R. E. & Pryor, L. L., 1975. *The transit system 1975*, Laurel Maryland: The Johns University - Applied Physics Laboratory.

Boeke, C., 2016. *Via Satellite at 30: The 1990s and Early 2000s*. [Online]

Available at: <http://interactive.satellitetoday.com/via-satellite-at-30-the-1990s-and-early->

2000s/

[Accessed 26 05 2020].

Burton, R. L. & Turchi, P. J., 1998. Pulsed Plasma Thruster. *Journal of Propulsion and Power*, 14(5), pp. 716-734.

Busek, n.d. *BmP-220 Micro-Pulsed Plasma Thruster*. [Online]

Available at: http://www.busek.com/technologies_ppt.htm

[Accessed 12 05 2020].

Cassady, R. J., Hoskins, W. A., Campbell, M. & Rayburn, C., 2000. *A Micro Pulsed Plasma Thruster (PPT) for the "Dawgstar" Spacecraft*, Washington: Primex Aerospace Company.

Cassady, R., Willey, M., Meckel, N. & Blandino, J., 1998. Pulsed plasma thruster for the New Millennium Space Interferometer Experiment DS-3. *34th AIAA/ASME/SAE/ASEE Joint Propulsion Conference and Exhibit*, Issue 98-3326.

Cerdan, X. A., 2016. *Study and design of a micro pulsed plasma thruster for a 3U Cubesat*, Sao Paulo: University of Sao Paulo.

Child, C. D., 1911. Discharge from Hot CaO. *Physical Review*, Volume 32, p. 492.

Choueiri, E. Y., 2004. A Critical history of Electric Propulsion: The First 50 Years (1906-1956). *Journal of Propulsion Power*, Volume 20, pp. 193-203.

Choueiri, E., 2008. Fundamentals of discharge initiation in pulsed plasma thrusters: Threshold criteria for undervoltage breakdown. *Journal of applied physics*, 093305(1), pp. 1-9.

Choueiri, E. Y., 2009. New Dawn for Electric Rockets. *Scientific American*, Feb, pp. 58-65.

Clary, D. A., 2003. *Rocket man: Robert H. Goddard and the birth of the Space age*. New York: Hyperion.

Coil, S. M., 1992. *Robert Hutchings Goddard*. New York: Orient BlackSwan.

De Carvalho, R. A., Estela, J. & Langer, M., 2020. *Nanosatellites Space and Ground Technologies, Operations and Economics*. NJ: Wiley & Sons.

Dunbar, B., 2014. *NASA*. [Online]

Available at: <https://www.nasa.gov/audience/foreducators/rocketry/home/hermann-oberth.html>

[Accessed 20 May 2020].

ESA, 2007. *ESA*. [Online]

Available at:

https://www.esa.int/About_Us/ESA_history/Lyman_Spitzer_Space_telescope_pioneer

[Accessed 20 May 2020].

- ESA, 2020. *Sharing Earth Observation Resources*. [Online]
Available at: <https://directory.eoportal.org/web/eoportal/satellite-missions/content/-/article/zacube-2>
[Accessed 13 08 2020].
- ESA, 2020. *Sharing Earth Observation Resources*. [Online]
Available at: <https://earth.esa.int/web/eoportal/satellite-missions/t/transit>
[Accessed 25 05 2020].
- Eslava, S., 2014. *Design of a Micro-Pulsed Plasma Thruster for 3U Cubesat*, Massachusetts: Worcester Polytechnic Institute.
- Fakel, 2018. *Experimental Design Bureau 'Fakel'*. [Online]
Available at: <https://fakel-russia.com/index.php/en/about>
[Accessed 25 05 2020].
- Fortescue, P., Swinerd, G. & Stark, J., 2011. *Spacecraft Systems Engineering, Fourth edition*. UK: John Wiley & Sons, Ltd.
- F'SATI, 2020. *F'SATI (French South African Institute of Technology)*. [Online]
Available at: http://www.fsati.org/images/F_SATI-Fiche.pdf
[Accessed 10 09 2020].
- Galactic, V., n.d. *Virgo in Galactic*. [Online]
Available at: <https://www.virgingalactic.com/vision/>
[Accessed 08 07 2020].
- Gamero-Castano, M. & Hruby, V., n.d. *A torsional balance that resolves sub-micro-Newton forces*, Massachusetts: International Electric Propulsion Conference.
- Gatsonis, N. A. et al., 2001. Experimental Investigations and Numerical Modeling of Pulsed Plasma Thruster Plumes. *Journal of Spacecraft and Rockets*, 38(3), pp. 454-464.
- Gatsonis, N. & Demetriou, M., 2004. Prospects of Plasma Flow Modeling and Control for Micro Pulsed Plasma Thruster. *AIAA-2004-3464, 40th Joint Propulsion Conference*, 11-14 July.
- Gibbon, P., 2014. *Introduction to Plasma Physics*, Geneva, Switzerland: CERN.
- Goddard, R. H., 1920. *Method and Means for Producing Electrified Jets of Gas*. United States, Patent No. 1363037.
- Goebel, D. M. & Katz, I., 2008. *Fundamentals of Electric propulsion: Ion and Hall thrusters*. California: Jet Propulsion Laboratory, California Institute of Technology.
- Guman, W. J., 1975. Designing Solid Propellant Pulsed Plasma Thrusters. *AIAA Paper 75-410*, March.

- Guman, W. J. & Peko, P. E., 1968. *Solid propellant pulsed plasma micro-thruster studies*. New York, AIAA 6th Aerospace Sciences Meeting.
- Guman, W. J. & Williams, T. E., 1973. Pulsed Plasma Microthruster for Synchronous Meteorological Satellite (SMS). *AIAA*, pp. 73-1066.
- Hart, P. J., 1962. Plasma Acceleration with Coaxial Electrodes. *The Physics of Fluids*, January.5(1).
- Haus, H. A. & Melcher, J. R., 1989. *Electromagnetic Field and Energy*. Massachusetts, USA: Prentice Hall.
- Hoskins, W. & Cassady, R., 2000. Applications for Pulsed Plasma Thrusters and the development of Small PPT's for Microspacecraft. *AAIA Paper 2000-3434, 36th AAIA/ASME/SAE/ASEE Joint Propulsion Conference*, 16-19 July.
- Howell, E., 2016. *Sergei Korolev: Architect of the Soviet Space Program*. [Online] Available at: <https://www.space.com/34396-korolev-biography.html> [Accessed 23 05 2020].
- Hutchinson, P. I., 2001-2021. *MITopencourseware*. [Online] Available at: <https://ocw.mit.edu/courses/nuclear-engineering/22-611j-introduction-to-plasma-physics-i-fall-2006/readings/chap3.pdf> [Accessed 23 05 2021].
- Inc, P. L., 2020. *Planet*. [Online] Available at: <https://storage.googleapis.com/planet-ditl/day-in-the-life/index.html> [Accessed 14 07 2020].
- Jahn, R. G., 1968. *Physics of Electric Propulsion*. New York: McGraw-Hill.
- Janson, S. W., 2011. *25 years of small Satellites*, Los Angeles: The Aerospace Corporation.
- Jourbert, M. L., 2021. *Orbital configuration and maintenance of nanosatellites through electric propulsion*, Cape Town: Cape Peninsula unuversity of Technology.
- Kawnine, T. & Kawnine, M., 2014. *Short Review on Electric Propulsion Systems: Ion Thruster*, s.l.: Lulea University of Technology.
- Kazeev, M. N., Kozubskiy, K. N. & Popov, G. A., 2009. *Victor Khrabrov - Pioneer of the First Space Electric Propulsion System Development and Space Tests*. Michigan; USA, s.n.
- Keidar, M. et al., 2006. Optimization Issues for a Micropulsed Plasma Thruster. *Journal of Propulsion and Power*, 22(1).
- Khrabrov, V. A., 2007. *Development and Flight Tests of the First Electric Propulsion System in Space*. Florence, Italy, s.n.

- Krommes, J. A., 2018. *An introduction to the physics of the Coulomb logarithm with emphasis on quantum-mechanical effects*, Princeton: Princeton Plasma Physics Laboratory.
- Kumagai, N. et al., 2003. *Research and development status of low power pulsed plasma thruster system for u-lab Sat II*. Toulouse, France, s.n.
- Laperriere, D. D., 2005. *Electromechanical Modeling and open-loop control of parallel-plate pulsed plasma microthrusters with applied magnetic fields*, Massachusetts: Worcester Polytechnic Institute.
- Larangot, B. et al., 2002. *Solid Propellant MicroThruster: an alternative propulsion device for nanosatellite*, 7 avenue du colonel Roche, 31077 Toulouse cedex 4, France: LAAS-CNRS.
- Lemmer, K., 2017. Propulsion for CubeSats. *Acta Astronautica 134*, 09 February, pp. 231-243.
- Lev, D. et al., 2017. The Technological and Commercial Expansion of Electric Propulsion in the Past 24 Years. *The 35th International Electric Conference*, 8-12 October.
- Lev, D. et al., 2019. The technological and commercial expansion of electric propulsion. *Acta Astronautica*, 18 March, pp. 213-227.
- Ley, W., Wittmann, K. & Hallmann, W., 2008. *Handbook of Space Technology*, Sussex, United Kingdom: John Wiley & Sons.
- Lovberg, R. H., 1968. *Nonsteady M.H.D Accelerators*, in J. Grey (ed.), "Plasma Technology,". Englewood Cliff, N. J.: Prentice-Hall Inc..
- Lun, J., 2008. *Development of a vacuum arc thruster for nanosatellite propulsion*, Cape Town: Stellenbosch University.
- McDowell, J., 2010. *Kappa and Lambda: Japan's first steps into space*, Cambridge, USA: Harvard_Smithsonian Center for Astrophysics.
- McGuire, M. L. & Myers, R. M., 1996. *Pulsed Plasma Thrusters for Small Spacecraft Attitude control*, Cleveland, Ohio 44135: NASA Lewis research Center.
- McKay, C. P., 2013. The Case for a NASA Research Base on the Moon. *Space Science Division, NASA Ames Research Center*, pp. 162-166.
- Michels, C. J., Heighway, J. E. & Johansen, A. E., 1966. Analytical and experimental performance of capacitor powered coaxial plasma guns.. *AIAA Journal*, 4(5), pp. 823-830.
- Mikellides, P.G.; Turchi, P. J., 1995. *Modeling of Ablation-Fed Pulsed Plasma Thrusters*. San Diego, s.n.
- Mueller, J., Hofer, R., Parker, M. & Ziemer, J., 2010. Survey For Propulsion Options For Cubesats. *57th JANNAF Propulsion Meeting* , 3-7 May, pp. 1-57.

- Nada, T. R., September, 2013. One-dimensional model of a pulsed plasma thruster. *Aeronautical Journal*, 117(1195), pp. 929-942.
- NASA, 2019. *Ernst Stuhlinger*. [Online]
Available at: https://www.nasa.gov/centers/marshall/history/power_to_explore.html
[Accessed 20 May 2020].
- NASA, n.d. *Konstantin E. Tsiolkovsky*. [Online]
Available at: <https://www.nasa.gov/audience/foreducators/rocketry/home/konstantin-tsiolkovsky.html>
[Accessed 19 05 2020].
- Nawaz, A., Albertoni, R. & Auweter-Kurtz, M., 2010. Thrust efficiency optimization of a pulsed plasma thruster SIMP-LEX. *Acta Astronautica*, Volume 67, pp. 440-448.
- Ou, Y. et al., 2018. Theoretical modeling and parameter analysis of micro-pulsed plasma thruster. *Energies*, 4 May.
- Palumbo, D. & Guman, W., 1976. Effects of propellant and electrode geometry on pulsed ablative plasma thruster performance. *Journal of Spacecrafts and Rockets*, 13(3), pp. 163-7.
- Palumbo, D. J. & Guman, W. J., 1972. Continuing Development of the Short Pulsed Ablative Space Propulsion System. *AIAA Paper 72-1154*, November.
- Paulino, V. D. S., 2020. *Innovation and trends in the space industry*. London: John Wiley & Sons Inc.
- Poly, C., n.d. *CubeSat Design Specification*. [Online]
Available at:
https://static1.squarespace.com/static/5418c831e4b0fa4ecac1bacd/t/56e9b62337013b6c063a655a/1458157095454/cds_rev13_final2.pdf
[Accessed 11 08 2020].
- Pottinger, S. J. & Scharlemann, C. A., 2007. Micro pulsed plasma thruster development. *30th International Electric Propulsion Conference*, 17-20 September.
- Power, X., 2020. *Mouser*. [Online]
Available at: https://www.mouser.co.za/datasheet/2/942/xppo_s_a0010519473_1-2295522.pdf
[Accessed 12 December 2021].
- Rezaeiha, A., 2014. Effect of power on PPT discharge current. pp. 207-214.
- Rezaeiha, A. & Schonherr, T., 2012. Analysis of effective parameters on ablative PPT performance. *Aircraft Engineering and Aerospace Technology*, 84(4), pp. 231-243.

- Rezaeiha, A. & Schonherr, T., 2013. *Overview of Alternative Propellants for use in PPT*. Nagoya, Japan, s.n.
- Scharlemann, C. et al., 2011. IEPC-2011-171. *Propulsion for Nanosatellites*, 32nd International Electric Propulsion Conference(171), pp. 1-6;10.
- Schein, J. G. et al., 2007. *Vacuum arc plasma thrusters with inductive energy storage driver*. United States, Patent No. US20070045248A1.
- Seifert, B. et al., 2013. *Development and verification of a uN thrust balance for high voltage electric propulsion systems*. USA, International Electric Propulsion Conference.
- Setlow, R. B., 1949. A High Current Ion Source. *Review of Scientific Instruments*, 20(8), pp. 558-560.
- Shepherd, L. R. & Cleaver, A. V., 1948. The Atomic Rocket I. *J. Brit. Interplanetary Soc.*, Volume 7, pp. 185-194.
- Shepherd, L. R. & Cleaver, A. V., 1948. The Atomic Rockets II. *J. Brit. Interplanetary Soc.*, Volume 7, pp. 250-262.
- Shepherd, L. R. & Cleaver, A. V., 1949. The Atomic Rocket III. *J. Brit. Interplanetary Soc.*, Volume 8, pp. 23-36.
- Shepherd, L. R. & Cleaver, A. V., 1949. The atomic rocket. IV. *J. Brit. Interplanetary Soc.*, Volume 8, pp. 59-70.
- Souder, M. D. & West, M., 2008. *Solar Sail technology for Nanosatellites*. Honolulu, Hawaii, s.n.
- Space, A. C., 2019. *Clyde Space*. [Online]
[Accessed 29 06 2020].
- SpaceX, 2020. *SpaceX*. [Online]
Available at: <https://www.spacex.com/human-spaceflight/mars/>
[Accessed 08 07 2020].
- Spanjers, G. & et al., 2002. AFRL MicroPPT development for Small Spacecraft Propulsion. *AAIA Paper 2002-3974, 38th AIAA/ASME/SAE/ASEE Joint Propulsion Conference*, 7-10 July.
- Spitzer, L., 1952. Interplanetary Travel Between Satellite Orbits. *Journal of the American Rocket Society*, Volume 22, pp. 92-96.
- Stuhlinger, E., 1954. Possibilities of Electrical Space Ship Propulsion. *5th International Astronautical Congress*, pp. 100-119.
- Stuhlinger, E., 1955. Electric Propulsion Systems for Space Ships with Nuclear Source Part I. *Journal of Astronautics*, Volume 2, p. 149.

- Stuhlinger, E., 1956. Electric Propulsion Systems for Space Ships with Nuclear Source Part II. *Journal of Astronautics*, Volume 3, p. 11.
- Stuhlinger, E., 1964. *Ion propulsion for space flight*. New York: McGraw-Hill.
- Tikhonravov, M. K., 1947. *Works on Rocket Technology*. Moscow: Publishing house of the defence ministry.
- Vondra, R. J. & thomassen, K. I., 1972. Performance Improvements in Solid Fuel Microthrusters. *Journal of Spacecrafts and Rockets*, 9(10), pp. 737-742.
- Vondra, R., Thomassen, K. & Solbes, A., 1971. A pulsed electric thruster for satellite control. 59(2), pp. 271-277.
- Wallangen, V., 2014. *Analytical Modeling of a Microthruster System for Nanosatellite Applications*, Stockholm, Sweden: Royal Institute of Technology .
- Wertz, J., 1999. *Space Mission Analysis and Design*. third edition ed. New York: Publishing Co..
- Zandbergen, B., 2013. *Micropropulsion systems for CubeSats*, Delft: Delft University of Technology.
- Ziemer, J. K., 2001. *Performance Scaling of Gas-Fed Pulsed Plasma Thrusters*, New Jersey: Princeton University.
- Ziemer, J. K. & Choueiri, E. Y., 2001. Scaling laws for electromagnetic pulsed plasma thruster. *Plasma Sources Science and Technology*, 5 June, pp. 395-405.
- Ziemer, J. K., Cubbin, E. & Choueiri, E. Y., 1997. *Performance Characterization of a High Efficiency Gas-Fed Pulsed Plasma Thruster*, New Jersey: Princeton University .